Ultrasonic wave propagation in compounds containing ordered vacancies

Seddon, T.

ULTRASONIC WAVE PROPAGATION IN COMPOUNDS CONTAINING ORDERED VACANCIES

A thesis submitted to the University of Durham

for the Degree of Master of Science

by

T. Seddon B.Sc. (Dunelm)

Department of Applied Physics and Electronics,
Science Laboratories,
South Road,
Durham.

September, 1972

A C K N O W L E D G E M E N T S

First I would like to express my sincere thanks to Dr. G. A. Saunders for his guidance, interest and constant encouragement during the period of this work and for showing that research can be a both rewarding and enjoyable experience, especially as a member of his ultrasonics and semimetals group.

I am greatly indebted to Professor D. A. Wright for giving me the opportunity to use the many facilities of his department and to the Principal, Mr. K. A. Holes and Board of Governors of Hebburn Technical College for generously allowing the time in which to pursue my research activities.

My thanks also go to Mrs. M. McCoulough for her careful typing of this manuscript, to the technical staff of the Applied Physics and Electronics Department headed by Mr. F. Spence; in particular Mr. R. Waite and Mr. C. Savage for their help on numerous occasions.

Finally, I wish to thank my wife Barbara for her patience, understanding and encouragement over the many months of this project.

C O N T E N T S

A B S T R A C T

The compounds $HgTe$, $Hg_5In_2\square Te_8$, $Hg_3In_2\square Te_6$ and $Hg_5Ga_2\square Te_8$, $Hg_3Ga_2\square Te_6$ constitute a series in which the concentration of vacancies, sited regularly on the lattice, increases progressively from zero. To assess the effect of such vacancies on the mechanical properties, the propagation of $10MHz$ ultrasonic waves in single crystal samples of each compound has been studied over the temperature range $77^{o}K$ to room temperature.

The large single crystals required for the ultrasonic experiments have been grown, using a modified Bridgman technique, from stoichiometric melts. Single crystal grains within each boule produced, have been identified by the use of polishing, etching and back reflection x-ray techniques. Back reflection x-ray photographs have been used primarily to establish the Laue group of $Hg_3In_2\square Te_6$, $Hg_3Ga_2\square Te_6$ and $Hg_5Ga_2\square Te_8$, which are shown to be cubic, and to align the samples in the specific direction required by the theory of ultrasonic wave propagation in solids; the $|110|$ axis in a cubic material. The lattice parameter of each of these compounds has been found using Debye-Scherrer powder photographs each of which exhibits a superlattice imposed on the zincblende pattern of lines, because of this $Hg_5In_2\square Te_8(Hg_5Ga_2\square Te_8)$ was indexed using a $2 \times 2 \times 2$ unit cell and $Hg_3In_2\square Te_6(Hg_3Ga_2\square Te_6)$ using a $3 \times 3 \times 3$ unit cell.

An order-disorder transformation has been observed in quenched samples of the semiconducting compound $Hg_3In_2\square Te_6$; extinction of the superlattice lines indicates that a change from an ordered to a disordered state is complete above $595 \pm 5^{o}K$. This effect has been further investigated by making resistivity, Hall voltage, thermoelectric power and differential thermal analysis measurements through the temperature region of the transistion. In each case the order-disorder

transformation had a marked effect on the results, especially in the transistion region.

The elastic constants of each compound have been determined from measurements of the ultrasonic velocity made by the pulse echo technique. These constants show a regular trend through each series, namely that the stiffness decreases as the vacancy concentration increases. In particular, there is a linear relationship between the reduced compressibility and the vacancy concentration. The elastic constants are also used to determine the anisotropy ratio, the Cauchy relationship and those parameters which can be related to interatomic binding such as the force constants of Born's model, ionicity (Potters relationship) and Debye temperature. Finally, the elastic constant data in conjunction with the mathematical theory for wave propagation in cubic crystals enabled the phase velocity surfaces, and the particle displacement and energy flux vectors to be determined.

Attenuation measurements - made over the same temperature range as the elastic constant data - exhibit Bordoni-type relaxation peaks on a background which is probably dominated by a resonance type loss mechanism associated with pinned dislocations. The peaks which occur in the compounds $HgTe$, $Hg_5In_2\square Te_8$ and $Hg_3In_2\square Te_6$ are consistent with dislocation motion on the *(111)* and *(110)* slip planes. In this series of compounds the activation energies for kink formation and the Peierls stresses, calculated on the basis of the kink nucleation theory, show that dislocation motion becomes easier with increased vacancy concentration and takes place more readily on the *(111)* slip planes.

CHAPTER I

INTRODUCTION

Interest has been aroused in the band structure and electron transport properties of mercury telluride *HgTe* and its pseudobinary alloys formed with other *II-VI* compounds or III_2VI_3 compounds. *HgTe* is a semimetal as a result of a small band overlap. Progressive addition of another telluride, such as *CdTe*, *MnTe* or In_2Te_3, causes the energy overlap to decrease until it goes through zero; the closer the band edges are, the smaller is the carrier effective mass and the greater is the carrier mobility. Narrow band gap alloys find a use in the fabrication of tunable long wavelength infrared lasers or detectors. Wright (1965) has found that addition of In_2Te_3 to *HgTe* reduces the band gap linearly with lattice parameter a_o until the composition *37.5 mol %* In_2Te_3 is attained; the zero gap alloy has a composition corresponding to *4 mol %* In_2Te_3. Compounds $Hg_5In_2Te_8$, $Hg_3In_2Te_6$ and $HgIn_2Te_4$ occur at compositions *37.5 mol %*, *50 mol %* and *75 mol %* In_2Te_3 in Hg_3Te_3 respectively (Spencer and Ray 1968). These compounds are semiconductors; the direct energy gaps for the first two being *0.61* and *0.78eV* respectively (Dahake 1967). Also of interest is a similar set of compounds, existing at the same percentage compositions, formed when Ga_2Te_3 is added to *HgTe*; the phase diagram for Ga_2Te_3 - *HgTe* has been investigated by Ray, Spencer and Younger (1969) but no information is available on the electrical and mechanical properties of these particular materials. While the electrical properties of the compound set *HgTe*-In_2Te_3 are well documented, few details of the lattice and mechanical properties are available. The primary purpose of this investigation is then to determine the elastic and anelastic properties of $Hg_3In_2Te_6$, $Hg_5Ga_2Te_8$ and $Hg_3Ga_2Te_6$ by

ultrasonic pulse echo techniques.

Before discussing the probable structure of these compounds, it is of value to sketch in the background. The elements which make up these compounds tend to form structures with tetrahedral bonds; every atom has four nearest neighbours, which are located at the vertices of a surrounding tetrahedron which may or may not be distorted. Simply, these structures form bonds which complete the octet shell of each atom, the electrons being shared with the four nearest neighbours. The average number of valence electrons per atom is then four; this is the Grimm-Sommerfeld rule. Binary compounds of composition *AB* will then be composed of equal amounts of elements from groups spaced symmetrically apart to the right and left of the group *IV* column in the periodic table. The most frequently observed structures in these compounds are the zincblende and wurtzite types but others are known.

Mercury telluride, which can be considered as the parent of the compounds studied here, is a *II-VI* compound with the cubic zincblende structure (Lawson et al 1959). This is composed of two equivalent, interpenetrating, face-centred cubic lattices, each containing one atomic species only, and relatively displaced one quarter of the distance along a cube diagonal (Figure 1.1). The unit cell contains two atoms, one on each sub-lattice, spaced by $a_o\sqrt{3}/4$, where a_o is the lattice constant of value $6.462A^o$ for *HgTe*.

An important aspect of the zincblende structure is the absence of a centre of symmetry or inversion. As a result, mercury telluride like the other zincblende crystals should be polar and piezoelectric. Figure (1.2) illustrates the feature that mercury-tellurium layers have a unique orientation along the $|111|$ direction. The opposed $(\bar{h}\bar{k}\bar{l})$ faces and the opposed $|hkl|$ and $|\bar{h}\bar{k}\bar{l}|$ direction can exhibit

different physical and chemical properties. For example, Warekois et al (1962) have shown that the intensity of x-rays diffracted from the *(111)* and *($\bar{1}\bar{1}\bar{1}$)* faces of mercury telluride are not the same, the high intensities being consistent with the reflection from a plane of mercury atoms. Further, preferential etching of the mercury surface was found and correlated with the x-ray data.

The sequence of binary compounds containing two atoms per molecule can be extended by replacing one atomic species by two different atoms from columns in the periodic table on either side of the column occupied by the replaced atom. Thus compound series $I\text{-}III\text{-}VI_2$, $I_2\text{-}IV\text{-}VI_3$ and $I_3\text{-}V\text{-}VI_4$ can be derived from *II-VI* compounds. There are known tellurium compounds in the $I_2\text{-}IV\text{-}VI_3$ group, for example Cu_2GeTe_3 and Cu_2SnTe_3, which also take the zincblende structure with *2Cu* and *1Ge* or *Sn* atoms randomly distributed on the three sites (Palatnik et al 1961). These and related compounds have all the available lattice sites occupied. Other compound series based on the zincblende lattice exist. Occupation of all the lattice sites is not a prerequisite for retention of the zincblende structure. The compounds studied here were chosen because they have vacant lattice sites. They are pseudo-binary in nature, and can be considered as being derived from *HgTe* by adding the appropriate amount of In_2Te_3 or Ga_2Te_3. The Grimm-Sommerfeld rule is not violated and can be applied with the modification due to Pamplin (1960). When a vacancy is designated as $\square$, $Hg_5In_2\square Te_8$ has five 2-valent, two 3-valent, one vacant site and eight 6-valent atoms and the composition can be written $II_5III_2\square VI_8$ so that

$$\frac{5.2 + 2.3 + 1.0 + 8.6}{5 + 2 + 1 + 8} = 4 \qquad (1.1)$$

The average number of valence electrons per site is then four. $Hg_5In_2\square Te_8$ *(or* $Hg_5Ga_2\square Te_8$*)* has one vacancy in every eight cation sites and $Hg_3In_2\square Te_6$ *(or* $Hg_3Ga_2\square Te_6$*)* one in every six cation sites;

the tellurium atoms occupy the anion sites. In both compound types the charges are balanced; $Hg_3In_2\square Te_6$ (or $Hg_3Ga_2\square Te_6$) can be thought of as being formed by replacing $3Hg^{2+}$ by $2In^{3+}$ (or $2Ga^{3+}$) plus one vacancy. A similar situation exists for $Hg_5In_2\square Te_8$ (or $Hg_5Ga_2\square Te_8$).

The fact that these compounds conform to the Grimm-Sommerfeld rule is not sufficient to ensure that they exist as tetrahedral structures. Mooser and Pearson (1959) have found that, as the average principle quantum number n of a compound increases, the bonds tend to lose their directional properties. Also as the electronegativity difference ΔX of the component atoms increases, the bonds tend to become more ionic. A graph (Figure 1.3) of ΔX versus n for several binary compounds reflects these tendencies. There is a sharp separation between the 4-co-ordination of the tetrahedral structure, the 6-co-ordination in cesium chloride type structures. *HgTe* itself, whose values of ΔX and n are listed (Table 1.1) fits neatly into the area occupied by the diamond and zincblende structures. Here the classification has been extended to include the ternary compounds of both the mercury-indium-tellurium and the mercury-gallium-tellurium sets by using

$$\Delta X = X_C - \left| \frac{kX_A + mX_B}{k + m} \right| \qquad (1.2)$$

the average electronegative difference. X_C, X_A and X_B are the electronegative values of the ions and k,m are the number of individual cations. The values of n and ΔX for each compound, listed in Table (1.1), compare closely with those of the parent compound *HgTe*. The position of these compounds on the graph (Figure 1.3) is firmly within the area occupied by *A4* and *B3* structures and suggest that they may be less ionic than the parent compound. Since *HgTe* has the zincblende structure, there is a strong possibility, provided the structure remains cubic in each case,

that the ternary compounds will take the closely related structure in which the tellurium anions lie on one face centred sub-lattice and the mercury, indium or gallium cations and vacancies on the other. When the present work was started, the actual structure of these compounds was in question. Ultrasonic studies in single crystals require knowledge of the Laue group. To assess this, a limited x-ray crystallographic study has been undertaken and it has been shown that all four compounds take a cubic structure of the $\bar{4}3m$ point group. The aim has not been to do a complete structural analysis, a formidable problem in itself.

The elastic and anelastic properties of the compounds $Hg_3In_2\square Te_6$, $Hg_5Ga_2\square Te_8$ and $Hg_3Ga_2\square Te_6$, obtained via the ultrasonic pulse echo measurements, have been compared and correlated with the results obtained for *HgTe* (Alper and Saunders 1967) and $Hg_5In_2\square Te_8$ (Alper, Pace and Saunders 1968). Large single crystals are required for this measuring technique, consequently much effort has been applied in this direction. Since the compounds can be produced with ordered lattices, an objective, has been to assess for the first time the way in which the presence of vacant lattice sites can affect the elastic properties of materials in general.

The presence of vacancies on a large scale should also affect the ultrasonic wave damping, in particular that associated with dislocation movement. Previously, ultrasonic wave propagation has been studied extensively in *HgTe*, with the object of assessing both the intrinsic properties and the effects of material imperfections (Alper and Saunders 1969). Dislocation damping was shown to play an important role; Bordoni type relaxation peaks resulting from intrinsic dislocation effects were observed. Similar peaks have now been observed in each of these vacancy compounds and are reported here. The results have been

interpreted on the basis of the kink nucleation theory (Seeger, Donth and Pfaff 1957); the activation energy for kink formation and the Peierls energy barrier to dislocation motion of the slip planes has been estimated. It has been shown that the presence of vacancies profoundly modifies not only the elastic properties but also the basic dislocation motion parameters.

Finally, as a consequence of the compounds being produced with ordered lattices an order-disorder transformation may occur. This has been found in $Hg_3In_2Te_6$; the temperature at which the change occurs and its effects on electrical properties have been investigated.

Table (1.1). Table of the average principle quantum number and the electronegativity difference for each compound. These values are based on electronegativity values given by Pauling and Huggins (1934).

	Average Principle Quantum Number $\bar{n}$	Electronegativity Difference ΔX
$HgTe$	5.50	0.30
$Hg_5In_2\square Te_8$	5.34	0.385
$Hg_3In_2\square Te_6$	5.27	0.42
$HgIn_2\square Te_4$	5.15	0.50
$Hg_5Ga_2\square Te_8$	5.20	0.385
$Hg_3Ga_2\square Te_6$	5.10	0.42
$HgGa_2\square Te_4$	4.86	0.50

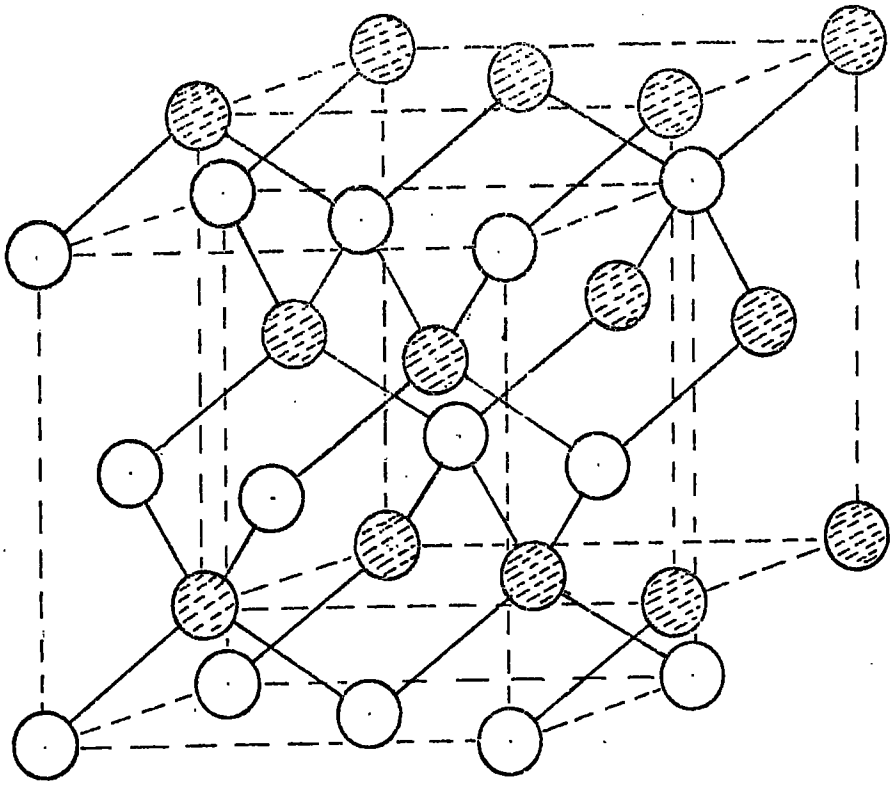

Fig. (1.1) The zincblende lattice shown as two interpenetrating face-centred cubic lattices.

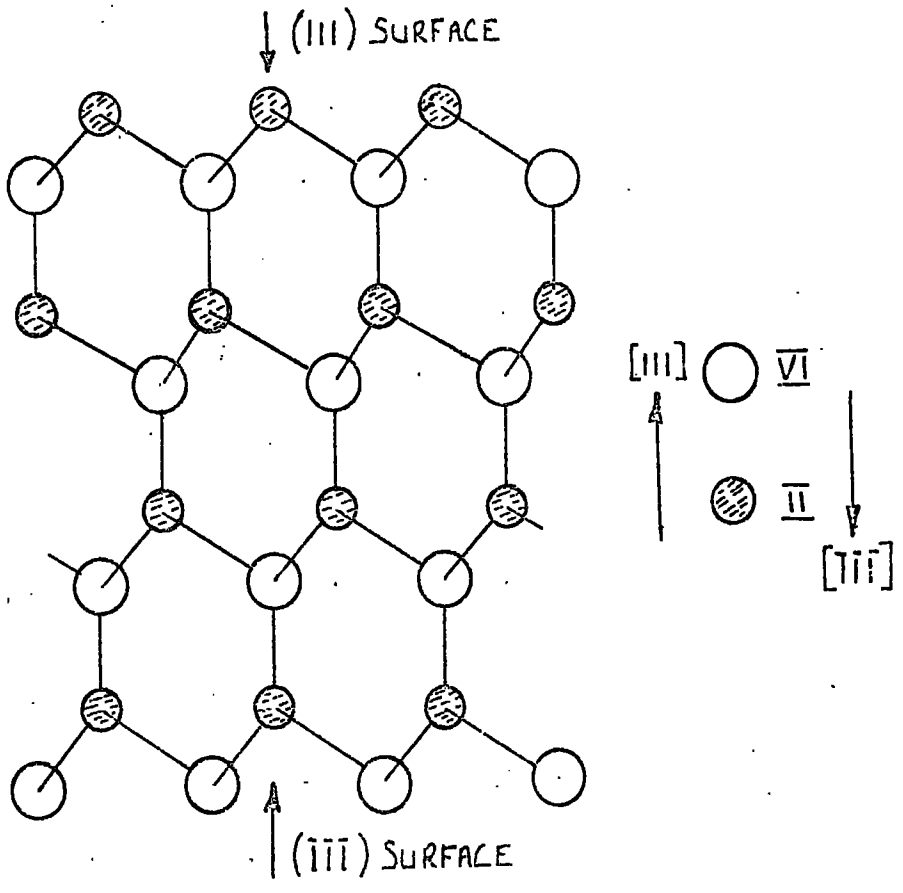

Fig. (1.2) The zincblende lattice in the |111| direction showing layers of atoms.

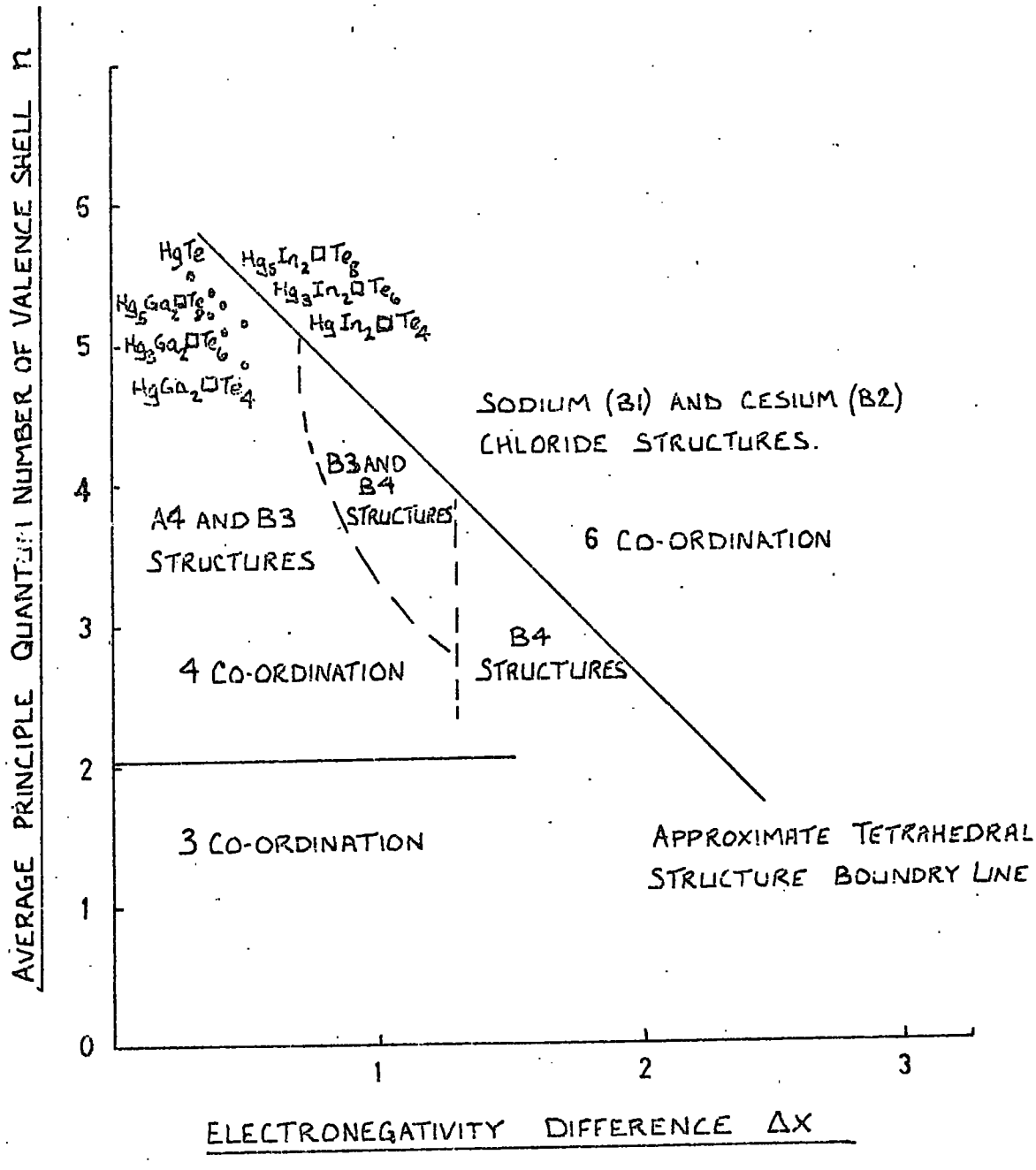

Fig. (1.3) A Mooser and Pearson (1959) chart of ΔX against n. The probable structure of a compound is indicated by the area in which it falls.

CHAPTER 2

CRYSTAL GROWTH AND X-RAY STUDIES

2.1 INTRODUCTION

Emphasis in the present work has been placed entirely on studies of compounds rather than intermediate solid solutions. The available compounds in any system can be found from an inspection of the phase diagram. The phase diagrams or more correctly the temperature-composition cross-sections for both pseudo-binary alloy systems Hg_3Te_3-In_2Te_3 (Figure 2.1) and Hg_3Te_3-Ga_2Te_3 (Figure 2.2) have been established by Spencer and Ray (1967) and Ray, Spencer and Younger (1969) respectively. The liquidus and solidus boundaries were determined by differential thermal analysis and the solvus boundaries from x-ray powder diffraction studies and microscopic observation of polished sections of the alloys. There are three regions on each of the diagrams, marked β, α_2 and γ, where the composition of the compounds is centred on the stoichiometric values *37.5 mol %, 50 mol % and 75 mol % of* In_2Te_3 *(or* Ga_2Te_3*)* in $HgTe_3$. The formulas of the corresponding compounds are $Hg_5In_2Te_8$ *(or* $Hg_5Ga_2Te_8$*)*, $Hg_3In_2Te_6$ *(or* $Hg_3Ga_2Te_6$*)* and $HgIn_2Te_4$ *(or* $HgGa_2Te_4$*)* respectively.

Attention has been restricted to the compounds $Hg_5In_2Te_8$, $Hg_5Ga_2Te_8$, $Hg_3In_2Te_6$ and $Hg_3Ga_2Te_6$ because evidence both from the present work and from other investigations shows that they are cubic and thus are ideal vehicles for a study of the elastic and anelastic properties of compounds with a high vacancy concentration. The compounds $HgIn_2Te_4$ and $HgGa_2Te_4$ have been excluded because Spencer et al (1967) and Ray et al (1969) report that they have a defect, chalcopyrite (tetragonal) structure. Vacancies of this type are an integral part of the structureas opposed to the Schottky and Frenkel point defect type of vacancy which occur

in all crystals. Schottky defects arise effectively by ions leaving their normal lattice positions and building on the surface of the crystal; to preserve electrical neutrality, the total charge on the migrant ions must balance. Frenkel defects are formed by ions leaving their normal lattice sites to take up interstitial positions, because ionic size is important, the occurrence of a vacancy is usually limited to the sub-lattice of the smaller ion, normally the cation. These defects arise from the spontaneous tendency of all systems to increase their entropy or degree of disorder, complete randomization is opposed by the fact that formation of defects requires energy. Then the density of these vacancies depends exponentially on the temperature and on their energy of formation. Depending on the crystal structure and the type of ion, the value of W_s and W_f the energy of formation of a Schottky defect and a Frenkel defect are quite different and usually the defect which has the lowest energy of formation dominates. Frenkel defects by their nature are likely to be important in crystals of the type considered here; the relatively open structure of the zincblende type lattice allows interstitial ions to be accommodated without much distortion. Nevertheless, the density of vacancies caused by this effect is very small compared with the enormous density of vacant lattice sites which normally exist in these compounds to satisfy the valency rule.

For pulse ultrasonic echo experiments, the transducer size, together with other considerations which are discussed in detail in chapter (4), demands that the samples must be large single crystals. As a consequence, much effort has been applied to growing crystals by a modified Bridgman-Stockbarger technique. Therefore, this chapter will be devoted to a discussion of the crystal growth technique and the subsequent x-ray work to determine first the symmetry and lattice parameters of the crystals

and then on alignment of the ultrasonic samples. Also, a superlattice pattern was recognised on some Debye-Scherrer powder photographs of $Hg_3In_2Te_6$ but not on others. This finding which suggested the existence of an order-disorder transformation in this compound, is of great interest in itself and has been investigated in more detail; a discussion of this aspect of the work can be found in sections (2.5) and (2.6)

2.2 DESCRIPTION OF THE GROWTH FURNACE

The furnace, shown in Figure (2.3), used to grow single crystals, consists of a vertically mounted, *78 cm* long, *4 cm* bore, mullite tube inside a rectangular *(78 x 40 x 40 cm^3)* sindanyo box. To increase the temperature gradient, the furnace was constructed in two sections, only the top half being well-insulated by vermiculate. The heater winding, made of kanthol wire was divided into three sections, the ratio of the current in each section being adjusted by means of ballast resistors, wound non-inductively to avoid disturbing the controller. This coupled with the insulation arrangement enabled the temperature profile of the furnace (Figure 2.4) to be adjusted to give two major features: a sharp gradient and a plateau. The temperature gradient was adjusted to be *35^oC per cm* at the growing interface.

A potentiometric, proportional, Eurotherm controller was employed to control the furnace temperature. An error voltage is developed between a measuring thermocouple sited in the furnace and a reference setting on the controller. The rate at which this is changing, and the length of time for which it exists controls the output power to the load. This results in a sophisticated system with a fast response time which is also able to override any spurious temperature fluctuations. The true temperature of the charge was measured by a thermocouple sited at

its base and a chart recorder was used to obtain a complete temperature record during the growth process. All the thermocouples used were made from platinum and 13% rhodium-platinum wires, the junction being made by fusing the ends with an oxygen gas flame. The thermocouple emf was then converted to temperature using a calibration chart conforming to *B.S.1826:1952* of an accuracy guaranteed to within $\pm$ 1^{o}C up to a temperature of 1100^{o}C.

Initially, the furnace was designed to allow crystal growth from the melt either by pulling the charge through the temperature gradient or by keeping the charge stationary, while lowering the temperature profile of the furnace. The latter function was achieved by driving the power control on the Eurotherm by means of a geared down motor, the temperature profile being lowered at approximately 2^{o}C per hour. Although eliminating mechanical vibration, this method suffers from the disadvantage that the rate at which the profile is lowered is not constant. Further, under these conditions the controller was merely being used as a sophisticated potentiometer. In the alternative method smooth lowering of the charge at a rate of 3 *mm* per hour was obtained through a stainless steel rod driven by a motor-gear system.

The system was later modified by using a ramp generator, which enabled the temperature profile to be lowered in a linear manner at a predetermined rate, adjustable between 0.5μV/hour (approximately 0.5^{o}C/hour and 9μV/hour (approximately 9^{o}C/hour). The generator connected in series with the controlling thermocouple, allowed the controller to be presented with the sum of the thermocouple and generator voltages. Then, as the generator voltage increased on a predetermined ramp, the thermocouple voltage and thus the furnace temperature fell to allow the voltage presented to the controller to remain constant. Hence the controller at all times operated correctly

on the feedback principle. This method proved to be the most successful and was employed to grow the majority of the crystals used in these experiments.

2.3 PREPARATION OF THE CHARGE AND CRYSTAL GROWTH

Crystals were grown in quartz crucibles whose size depended on the growth technique. Crucibles used in the pulling technique were made from *15 mm* bore quartz tubing and the charge occupied approximately *6 cm* of the tube; those used in the temperature profile lowering method were made from *24 mm* tubing. The difference between the crucible dimensions was necessary because in the latter method both the freezing interface and the charge should lie completely in the temperature gradient; the large diameter tubes allowed a charge length of approximately *3 cm*. Both types of crucible were similar in shape, the bottom end being conical with an angle of about 70^{o} to facilitate seed crystal formation (Figure 2.5). In each case the tube wall thickness was *1.5 mm*, allowing the crucible to withstand a pressure of *25* atmospheres.

The tubes were cleaned with hydrofluoric acid followed by washing with distilled water and dried under a vacuum. To prevent the sample from sticking to the inside of the tube, the surface can be coated by burning a few drops of acetone in the crucible with an oxygen gas flame, but this was not found to be necessary.

Single crystals of each compound, $Hg_3In_2\square Te_6$, $Hg_3Ga_2\square Te_6$ and $Hg_5Ga_2\square Te_8$ were grown from stoichiometric melts, usually by lowering the temperature profile with the ramp generator. Ingots produced by pulling the charge through the freezing point, were without exception polycrystalline, but the grains in some cases were quite large and it was just possible by careful cutting to obtain a monocrystalline ultrasonic sample.

The crucible was charged with the correct gram molecular weight of *99.999%* purity, mercury, indium or gallium and tellurium, to a weighing tolerance of *1 milligram*. The materials were obtained from the Koch-Light Co. Limited. With the exception of mercury, the elements were solids and needed to be melted through the neck of the tube with an oxygen-gas flame; this was done under a vacuum *(10^{-6} torr)*. Gallium or indium were melted first because of their low vapour pressure relative to tellurium. During melting, tellurium vapour did coat the neck of the tube but diffraction patterns observed in this film indicated that it was less than *10 micron* thick. Hence any loss in weight of the material was within the weighing tolerance. Finally, the tube was sealed at the neck after being evacuated to about *10^{-6} torr;* care was taken to ensure that the charge was not heated during this process.

The charged crucible was placed inside a stainless steel bomb, for safety reasons, and this was then located on the top of the pulling bar in the furnace (Figure 2.3). The position of the charge was such that the temperature profile showed that the conical tip of the crucible was about *15°C* above the melting point of the appropriate compound.

To prevent an excessive build up of the vapour pressure of mercury (vapour pressure of mercury at *700°C* is *70* atmospheres), the furnace temperature was increased over a period of three days until the correct temperature profile was obtained. This was found by experience.

Preliminary runs showed that samples obtained using high growth rates *(10°C/hour)* or with a small temperature gradient *(5°C/cm)* exhibited the effects of constitutional supercooling. Also with very slow growth rates *(0.5°C/hour)* the boule had a layer-like structure, indicating that the materials had separated out. The optimum growth rate was *2°C/hour* and gave large, well formed single crystals of each compound.

2.4 EXAMINATION AND ORIENTATION OF THE CRYSTALS

After the crucible had been opened with a water cooled grinding wheel, the sample was easily removed. To reveal any grain boundaries, the specimens were etched for about 20 seconds with a freshly prepared mixture of 1-part by volume concentrated nitric acid, 1-part concentrated hydrochloric acid and 2-parts distilled water, followed by re-etching with concentrated hydrochloric acid and washing with distilled water. When used at room temperatures this etchant, employed by Delves for mercury telluride oxidized the surface but this problem was overcome by heating to about $45^{o}C$. The polishing etchant used by Warekois et al (1962) of 6-parts HNO_3, 1-part HCl and 1-part H_2O for mercury telluride did not have the desired effect: the surface oxidized.

Normally, the boule was a large single crystal or it contained a very large grain, in which case the samples were obtained by cutting off any minor grains with a diamond wheel. The specimen was further inspected by x-ray back reflection techniques. Laue photographs were taken at intervals along a sample face and the procedure was repeated after rotation through $180^{o}C$. The sample to film distance (3 cm) and the angular orientation were held constant during this process; if the sample was a single crystal, all the photographs were identical. To check further, an additional series of photographs was taken after the crystals had been aligned and cut from the main body of the boule. Lack of spot splitting on these photographs, examples of which are given in Figures (2.6), (2.7) and (2.8), indicates an absence of any cellular or mosaic structure. Any surface damage produced by cutting was removed by the polishing etch: spot size reduced and their general appearance improved.

The Laue back reflection x-ray technique was also put to its principle uses: to determine the symmetry of a crystal and its

orientation relative to the x-ray beam. The ideal crystal is referred to identical unit cells, any one of which can be made to coincide with its neighbours by simple translations. The ensemble of all the unit cells forms the crystal lattice and the cell is usually, but not always, chosen as the smallest parallelopiped out of which the crystal can be constructed. The edges of the unit cell are parallel to the crystallographic axes *a*, *b* and *c*, and their relative dimensions are the unit distances along these axes.

Bravais showed that the number of types of polyhedra that will completely fill the space is seven. When body-centred and face-centred polyhedra were added, the total number increased to fourteen. Each polyhedron can be considered a unit cell. From these simple lattices are evolved the seven crystal systems. The edges of the polyhedra are the crystallographic axes, and the faces are the pinacoids of the crystal. The crystal systems evolved from the Bravais lattices are in order of increasing symmetry, the triclinic, monoclinic, or the rhombic, tetragonal, trigonal, hexagonal and cubic. Each of these systems can be broken down into point groups or crystal classes; the total number being *32*. The point group within a Bravais system to which a crystal belongs is determined by the number of symmetry elements of each kind possessed by that crystal. In general there are 2-fold, 3-fold, 4-fold and 6-fold symmetry axes, mirror planes and inversion symmetry axes which are designated $\bar{1}$, $\bar{2}$, $\bar{3}$, $\bar{4}$, and $\bar{6}$. The 2-fold inversion axis is equivalent to a mirror plane. In this case, the symmetry properties of the cubic point group are of particular interest here and these are listed in Table (2.1). The procedure then, has been to examine by x-ray back reflection photographs the symmetry of crystals of each compound and to compare the symmetry properties obtained with those listed in Table (2.1).

Point Group Symbol	Number of Symmetry Elements of Each Kind								
	m	*2*	*3*	*4*	*6*	$\bar{1}$	$\bar{2}$	$\bar{3}$	$\bar{4}$
23	-	*3*	*4*	-	-	-	-	-	-
m3	*3*	*3*	*4*	-	-	*1*	*3*	*4*	-
432	-	*6+(3)*	*4*	*3*	-	-	-	*4*	-
$\bar{4}$*3m*	*6*	*(3)*	*4*	-	-	-	*6*	-	*3*
m3m	*9*	*6+(3)*	*4*	*3*	-	*1*	*9*	-	*3*

Table 2.1

Crystallographic point groups of the cubic crystal class

X-ray reflection occurs when the Bragg law is obeyed

$$n\lambda = 2d\sin\theta \qquad (2.1)$$

where n is an integer, λ is the wavelength of the x-rays in Ångström units, d is the spacing between atomic planes and θ is the angle of reflection. The d value is fixed by the crystal and, if the sample is stationary, θ is also fixed. Therefore, each plane will choose the right wavelength from the white radiation used for reflection. A plane that happens to reflect radiation of a wavelength that is strong in the incident beam, for example K_α radiation, will give a strong spot even though it may not be an important plane. If a group of symmetrically equivalent planes all reflect the characteristic radiation, then the symmetry axis relating them is parallel to the incident beam. In general however, each spot on a Laue photograph comes from a different wavelength. The symmetry of the reflection pattern obtained is consistent with the crystal symmetry. If the beam looks down a 4-fold axis of the crystal, the Laue photograph produced will show a 4-fold axis of symmetry. Since x-ray reflection is the same from either side of a set of atomic planes, the x-rays add a centre of symmetry to the symmetry of the crystal; this is called Laue symmetry.

The crystals, mounted on a Phillips goniometer were lined up onto a symmetry axis by measuring the Laue films with a Greninger net. In each crystal $Hg_3In_2\square Te_6$, $Hg_5Ga_2\square Te_8$ and $Hg_3Ga_2\square Te_6$ a 2-fold, 3-fold and 4-fold axis was located (Figures (2.6), (2.7) and (2.8)). Possession of a 3-fold and a 4-fold axis is sufficient evidence in itself to establish that each crystal is cubic; none of the other crystal systems has a point group with both a 3-fold and 4-fold symmetry axis. In the cubic system these symmetry properties are

located to the *432*, $\bar{4}3m$ and *m3m* point groups which are situated within the highest Laue symmetry group. Nevertheless, to confirm this result a crystal of each compound was mounted on a 2-fold axis $|110|$ and a 4-fold axis $|001|$ was located. Then rotation through $35{\cdot}3^{o} \pm 1^{o}$ located a 3-fold axis $|1\bar{1}1|$ and a further rotation through $54{\cdot}7^{o} \pm 1^{o}$ located a 2-fold axis $|\bar{1}10|$. The crystal was then mounted on this axis and the procedure was repeated; a 4-fold $|001|$, 3-fold $|111|$ and 2-fold $|110|$ axis were located at the same angles. This finding, within the limits of the experimental error, showed that $Hg_3In_2\square Te_6$, $Hg_5Ga_2\square Te_8$ and $Hg_3Ga_2\square Te_6$ are cubic, this has not been previously established. Alper, Pace and Saunders (1968) have also shown that $Hg_5In_2\square Te_8$ is cubic with a point group within the same Laue group as the above compounds. This has been confirmed by H. MaCartney (private communication) it is not possible on a basis of the symmetry exhibited by Laue photographs to determine if the structure has either the *432*, $\bar{4}3m$ or *m3m* point group. The parent compounds *HgTe* (Lawson et al 1959) and In_2Te_3 (Hahn and Klinger 1949) have a zincblende structure with a point group $\bar{4}3m$, hence it would appear reasonable to suggest that these compounds $Hg_5In_2\square Te_8$, $Hg_5Ga_2\square Te_8$, $Hg_3In_2\square Te_6$ and $Hg_3Ga_2\square Te_6$ which are modifications of *HgTe* also belong to the $\bar{4}3m$ group and have a zincblende type structure. The elements of symmetry, crystallographic axes and stereogram of this point group are given in Figure (2.9).

Samples required for the ultrasonic experiments were cut with faces perpendicular to the $|110|$ axis. The crystals were aligned to within $\pm\frac{1}{2}^{o}$ of the pre-requisite axis by the Laue technique. By using *3 micron* followed by *1 micron* diamond dust, the faces were polished flat and parallel to within 10^{-4} *cm*. Parallism was checked by using a dial micrometer.

2.5 MEASUREMENT OF LATTICE SPACING, IDENTIFICATION OF THE POINT GROUP AND EFFECT OF ORDERING

Examination of the Laue back reflection photographs has established that each of the compounds investigated is cubic and belongs to one of the point groups *432*, $\bar{4}3m$ or *m3m*. However, this method cannot differentiate between these groups and fails to determine conclusively that these compounds have a similar structure to their parent compounds *HgTe* and In_2Te_3 or Ga_2Te_3. The objective then in taking Debye-Scherrer *X*-ray powder photographs of each compound was to assess the structure type and lattice parameter a_o of each compound and compare the results with the structure and lattice parameter of the parent compounds.

The method involved grinding a small specimen to a fine powder and then gluing this with a collodian solution to a glass fibre to form an aggregate of tiny crystals. The fibre was located along the axis of a Phillips-Scherrer camera of circumference *360 mm*, around which was located the film; a small electric motor was then used to rotate the fibre in a nickel filtered monochromatic copper K_α *x*-ray beam. *X*-rays are diffracted from the atomic planes when the angle made by the crystallites relative to the incident beam satisfies the Bragg Law. In this case, there are large numbers of crystallites all with a completely random orientation which cause the incident beam to be diffracted in the form of cones, the diameter of which relative to the incident beam can be readily measured using a Hilger and Watt illuminated scale to an accuracy of *0.05 mm*. Since the camera circumference is a convenient *360 mm*, the diffraction angle θ was a direct measurement and the d spacing could be obtained from

$$\lambda = 2d_{hkl}\sin\theta \qquad (2.2)$$

Normally, a twenty hour exposure was adequate to resolve the singlets at the low θ end of the film but accurate measurement of

lattice spacing requires that the doublets at the high θ end of the film be resolved, to achieve this the exposure was increased to about fifty hours, but the singlets were then virtually lost in the background. Dahake (1967) reported that the sharpness of the lines was influenced mainly by the homogenity of the sample, all high angle lines being diffuse and all low angle lines being very broad. This was not the case here, the lines on these photographs are well defined. Further, if the samples were finely powdered, the low angle lines were sharp and the high angle lines were not too well resolved. This could be due to excessive grinding distorting the crystal structure. As far as possible, in these photographs (Figures 2.10, 2.11, 2.12, 2.13, 2.14 and 2.15) a compromise between uniform low angle lines and well resolved high angle lines was achieved.

For a precision measurement of lattice parameter a_o, it is essential that reflections at angles as close to θ equal to 90^o as possible be used. The reason for this is apparent when the relationship between θ and the d spacing (Equation 2.2) is examined; $1/d$ has a sinusoidal dependence on θ and an error Δθ in measuring this angle produces a greater error in d at low values of θ than at high values of θ. This can be seen more easily by differentiating the Bragg equation (2.2) to give

$$\Delta d = - d \cot\theta \, \Delta\theta; \qquad (2.3)$$

the error Δd goes to zero at θ equal to 90^o. All systematic errors such as non-coincidence of the camera axis and the rotation axis of the specimen would be zero in this limit. Although it is not possible to achieve this condition since θ equal to 90^o corresponds to a reflection back into the x-ray beam, a close approximation can be obtained by calculating the lattice parameter a for several reflections

having different values of θ using

$$\sin^2\theta = \frac{\lambda^2 N}{4a^2} \quad , \tag{2.4}$$

where $d = a/\sqrt{N}$ and N is defined from the Miller indices of the reflecting plane by the relationship.

$$N = h^2 + k^2 + l^2 \tag{2.5}$$

The values obtained for a were plotted against the function

$$\frac{1}{2}\left(\frac{\cos^2\theta}{\sin\theta} + \frac{\cos^2\theta}{\theta}\right) \tag{2.6}$$

introduced by Nelson and Riley (1945) as an appropriate linear relationship between a and θ. Extrapolating this curve to where the function is zero (corresponding to θ equal to 90^o) gave the corrected lattice parameter a_o. This value, calculated for each of the compounds, together with the values calculated for *HgTe* (Alper and Saunders 1967) and $Hg_5In_2\square Te_6$ (Alper et al 1968) for comparison, are presented in Table (2.2). The measurements, for crystals $Hg_3In_2\square Te_6$ and $Hg_5Ga_2\square Te_8$ have a close correspondence with the measurements made by other workers, but the value a_o equal to $6.216A^o$ obtained for $Hg_3Ga_2\square Te_6$ appears to be somewhat larger than the value $6.162A^o$, obtained by Ray et al (1969).

It is apparent on simply comparing the powder photograph of each vacancy compound (Figures 2.11, 2.12, 2.13 and 2.15) against the powder photograph of mercury telluride (Figure 2.10), that the basic pattern of the lines is very similar. Superimposed on this strong pattern is a weak set of superlattice lines, indicating that the atoms in each material are arranged in an ordered structure.

Table (2.2) Lattice spacing a_o, x-ray density calculated by using a_o and density measured using Archimedes principle.

	$Hg_3In_2\square Te_6$	$Hg_5In_2\square Te_8$	$HgTe$	$Hg_3Ga_2\square Te_6$	$Hg_5Ga_2\square Te_8$
Lattice spacing a_o A^o	6.289 ± 0.002	6.33 ± 0.01	6.462 ± 0.001	6.216 ± 0.002	6.236 ± 0.002
X-ray density g/cm^3	7.05 ± 0.01	7.3 ± 0.01	8.079 ± 0.01	6.96 ± 0.01	7.39 ± 0.01
Density (Archimedes Principle) g/cm^3	7.10 ± 0.01	7.23 ± 0.01	8.08 ± 0.01	7.12 ± 0.01	7.88 ± 0.01

Initially, the photographs were indexed using a Bunn chart on the basis that since *HgTe* is zincblende and the lattice of each vacancy compound remains cubic, there would be a strong possibility that these compounds would also be zincblende; the tellurium anions forming a face centred lattice and the mercury, indium or gallium cations and vacancies being distributed in an ordered manner on the other interpenetrating face centred cubic lattice. This method allowed the main pattern to be indexed, but for a complete analysis the indices of the reflecting planes were obtained using Equations (2.4) and (2.5) under the condition that the selection rules be obeyed; values of N are restricted for the zincblende lattice to values of h, k, l which are either all even or all odd. There are also the forbidden numbers $N = 7, 15, 23, 28$ - - - as these cannot be expressed as the sum of three squares. The powder photographs of the compounds have a characteristic pattern due to the superposition of two sets of lines, one being the diamond type lattice indexed

$$N = 3, 8, 11, 16, 19, 24, 27 - - - -$$

the additional lines

$$N = 4, 12, 20, 36, 44, - - - - - -$$

required for a face centred cubic lattice are only faintly visible for zincblende materials. These lines are missing in each case from the basic pattern of each vacancy compound, but not completely from *HgTe*. The zincblende structure is often depicted as a cube containing eight atoms. For example, mercury telluride has four tellurium atoms on a face centred cubic lattice and the four mercury atoms are situated diagonally in the tetrahedral voids. In each vacancy compound these four lattice sites will contain either mercury or indium (or gallium) atoms or a vacancy. A repeatable cell for the compounds $Hg_5In_2\square Te_8$ and $Hg_5Ga_2\square Te_8$ can be contained in a block of $2 \times 2 \times 2$ unit cells

which will accommodate four molecules; the compounds $Hg_3In_2\square Te_6$ and $Hg_3Ga_2\square Te_6$ will require a block of *3 x 3 x 3* unit cells containing eighteen molecules. This concept allowed the powder photographs of the compounds $Hg_5In_2\square Te_8$ and $Hg_5Ga_2\square Te_8$ to be fully indexed, even the superlattice lines. The intensity of the lines has been estimated visually and grouped into six categories, viz.: *VS, S, FS, W, VW* and *VVW*. These are listed in Table (2.3) for both compounds together with the cubic indices based on a *2 x 2 x 2* unit cell and the measured *d* spacing for each line. The photographs of the compounds $Hg_3In_2\square Te_6$ and $Hg_3Ga_2\square Te_6$ were indexed using a *3 x 3 x 3* unit cell, this again suggested index values for the lines but in this case identification, although good, was not quite so definite; results are listed in Table (2.4). The compound *HgTe* was also indexed Table (2.5) to allow each vacancy compound to be compared with the parent compound and common reflections are marked with an asterisk. The question of the actual position of the atoms and vacancies in the lattice of $Hg_5In_2\square Te_8$ has been investigated extensively by H. Macartney and a full account will be produced in his Ph.D Thesis. An important result is that the vacancies dominate the ordering of the superlattice.

A repeatable cell, whose dimensions are known from the lattice parameter, containing a complete number of molecules allowed the *x*-ray density to be calculated. This value and the value of density measured using Archimedes principle are listed for each compound in Table (2.2).

Compounds $Hg_5In_2\square Te_8$ and $Hg_5Ga_2\square Te_8$ crystallize with an ordered lattice, but it has been found (Spencer et al 1967 and Ray et al 1969) that both $Hg_3In_2\square Te_6$ and $Hg_3Ga_2\square Te_6$ can be produced with a disordered lattice, this is not necessarily the case as photographs (2.13), (2.14) and (2.15) clearly demonstrate. Crystals of $Hg_3In_2\square Te_6$

Table (2.3) Interplanar spacing in $Hg_5In_2\square Te_8$ and $Hg_5Ga_2\square Te_8$, indexed using a 2 x 2 x 2 unit cell. Reflections equivalent to the HgTe pattern are marked with an asterisk.

$Hg_5In_2\square Te_8$

Line No.		d spacing A^o	h,k,l.
1	VS *	3.6570	222
2	W	2.9079	331
3	W	2.8268	420
4	W	2.5816	422
5	S	2.4393	333;511
6	VS*	2.2388	440
7	VW	2.1435	531
8	VW	2.1101	600;442
9	VS*	1.9097	622
10	W	1.7723	551;711
11	FS	1.6487	731;553
12	S*	1.5820	800
13	VW	1.5361	644/820
14	VW	1.4928	660;822
15	FS*	1.4496	662
16	VW	1.390	753;911
17	VW	1.3291	931
18	FS*	1.2936	844
19	VVW	1.2727	755;771
20	VVW	1.2415	862;10,2,0
21	FS*	1.2228	666;10,2,2
22	W	1.1780	864
23	W*	1.1194	880
24	W	1.1070	971;955
25	W*	1.0737	10,6,2
26	VVW	1.0280	10,6,4;12,2,2
27	W*	1.0028	12,4,0
28	W*	0.9474	10,6,6
29	VW	0.9454	10,8,4
30	VW	0.9273	13,3,3
31	VW*	0.9152	888
32	W*	0.8828 0.8725	10,10,2; 12,8,0
33	W	0.8567 0.8496	11,7,7; 13,5,5
34	W*	0.8458 0.8437	12,8,4
35	W	0.8257 0.8205	10,6,6; 14,6,2
36	W	0.8011 0.8011	11,9,7;11,11,3 13,9,1;15,5,1

$Hg_5Ga_2\square Te_8$

Line No.		d spacing A^o	h,k,l.
1	VS*	3.604	222
2	W	2.841	331
3	W	2.779	420
4	VW	2.535	422
5	W	2.397	333;511
6	VS*	2.197	440
7	W	2.1055	531
8	W	2.066	600;442
9	VS*	1.875	622
10	VW	1.756	551;711
11	FS	1.621	731;553
12	S*	1.556	800
13	FS*	1.432	662
14	FS*	1.273	844
15	W*	1.203	666;10,2,2
16	W*	1.1015	880
17	VW	1.0898	971
18	W*	1.0458	10,6,2
19	W*	0.9850	12,4,0
20	W*	0.9518	10,6,6
21	VW*	0.8986	888
22	VW*	0.8726	10,10,2;12,8,0
23	VVW*	0.8415	11,7,7;13,5,5
24	W*	0.8341 0.8345	12,8,4
25	W*	0.8112 0.8119	10,10,6;14,6,2

Table (2.4) Interplanar spacing in $Hg_3In_2\square Te_6$ and $Hg_3Ga_2\square Te_6$, indexed using a *3 x 3 x 3* unit cell. Reflections equivalent to the *HgTe* pattern are marked with an asterisk. These reflections are also common in the ordered and disordered compounds of $Hg_3In_2\square Te_6$.

$Hg_3In_2\square Te_6$

Line No.		d spacing A^o	h,k,l
1	VS*	3.6442	333;511
2	VW	2.8912	533
3	VVW	2.8128	622
4	VW	2.7212	444
5	W	2.5660	640
6	W	2.3821	800
7	VS*	2.1857	660;442
8	VVW	2.0976	840
9	VS*	1.8922	933
10	VW	1.7690	864
11	W	1.6404	10,4,4
12	S*	1.5706	12,0,0
13	S*	1.4444	9,9,3
14	S*	1.2834	12,6,6
15	FS*	1.2165	15,3,3
16	FS*	1.1116	12,12,0
17	FS*	1.0632	15,9,3
18	W*	0.9935	18,6,0
19	W*	{0.9603 0.9582	15,9,9
20	W*	{0.9081 0.9077	12,12,12
21	W*	{0.8783 0.8804	15,15,3
22	FS*	{0.8405 0.8402	18,12,6
23	FS*	{0.8187 0.8188	15,15,9

$Hg_3Ga_2\square Te_6$

Line No.		d spacing A^o	h,k,l
1	VS*	3.5859	333
2	W	2.8566	533
3	VW	2.6490	444
4	VW	2.5208	640
5	W	2.3880	553
6	VS*	2.1927	660
7	VW	2.1478	751
8	S	2.1072	840
9	VS*	1.8714	933
10	W	1.8292	10,2,0
11	VW	1.7814	8,6,4
12	FS	1.6156	10,4;4
13	FS*	1.5529	12,0,0
14	W	1.5176	10,6,4
15	FS*	1.4269	993
16	W	1.3754	12,6,0
17	FS*	1.2709	12,6,6
18	VW	1.2354	10,8,8
19	FS*	1.2010	999
20	W*	1.0977	12,12,0
21	W*	1.0537	15,9,3
22	VW	1.0271	12,12,6
23	VW*	0.9842	18,6,0
24	VVW	0.9512	15,9,9
25	VVW	0.9118	17,9,7;17,11,3

Table (2.5) Interplanar spacing and indexed reflections in *HgTe*.

Line No.	d spacing A^{o}	*h,k,l*
1 VS	*3.743*	*111*
2 W	*3.2341*	*002*
3 VS	*2.2801*	*220*
4 VS	*1.9463*	*311*
5 S	*1.6140*	*400*
6 S	*1.5096*	*331*
7 S	*1.3170*	*422*
8 S	*1.2621*	*333*
9 W	*1.1411*	*440*
10 S	*1.0907*	*531*
11 S	*1.0214* *1.0267*	*620*
12 W	*0.98499* *0.98485*	*533*
13 W	*0.93196* *0.93160*	*444*
14 FS	*0.90449* *0.90434*	*551*
15 S	*0.86310* *0.86296*	*642*
16 S	*0.84124* *0.84077*	*553*

with either an ordered or disordered structure, have been obtained using the appropriate experimental conditions. Lewis (1965) obtained an ordered crystal of $Hg_3In_2\square Te_6$ with a lattice parameter a_o = $6.295A^o$ corresponding to the value obtained here, confirming the finding of Woolley and Ray (1960); he also reported that Spencer had produced an ordered sample about this time. However, Lewis's compound had the composition $Hg_3In_{1.98}\square_{1.02}Te_6$ and Dahake (1967) suggested that this was the cause of the superlattice lines on the powder photograph, probably because an excess of mercury due to annealing does produce additional lines but their pattern is different from the characteristic pattern produced by an ordered superlattice. Stoichiometry, no doubt effects the ordering of the cation lattice but in the opposite way; the vacancies dominate and increasing their number to *1.02* per molecule will increase the degree of disorder. This is to be expected since similar defect compounds have practically no homogenity range. For example, efforts to reduce the number of vacancies in Ga_2S_3 with gallium atoms are futile; even with small additions the material simply reduces to a two phase mixture containing Ga_2S_3 and *GaS* (Parthé 1964, page 46).

Hahn and Klinger (1949) and Hahn (1952) found that prolonged annealing of $Ga_2\square Te_3$ and $In_2\square Te_3$ produced superlattice lines and it was suggested that this was due to ordering of the ions and vacancies on the cation lattice. Since crystals of compounds $Hg_3In_2\square Te_6$ and $Hg_3Ga_2\square Te_6$ which contain *50%* $In_2\square Te_3$ and *50%* $Ga_2\square Te_3$ respectively, can be produced in either the ordered or disordered form, it was thought that annealing at elevated temperatures followed by quenching would produce a disordered superlattice. Samples of $Hg_3In_2\square Te_6$ were sealed under vacuum in *4 mm* quartz tubes. The specimens were then suspended in a furnace, similar to the crystal growth type, at

preselected temperatures to within ±5°C between 227°C (500°K) and 627°C (900°K) for more than 200 hours and then quenched in water. Normally 100 hours was adequate. The Debye-Scherrer powder photographs obtained from samples of this crystal annealed at 302°C (585°K) or below showed the extra lines due to Bragg reflections from the ordered superlattice. Diminishing superlattice line intensities indicate decreasing order as the annealing temperature was raised. Quenching from 332°C (605°K) or above produced a disordered structure: the superlattice lines were absent. Thus the material goes from an ordered to a disordered structure over a temperature range of 30°C between 302°C to 332°C; the presence or absence of mercury vapour did not alter this basic finding. The disordered phase has a pseudo zincblende structure (point group $\bar{4}3m$) and a lattice parameter a_o of 6.289 ± 0.002A° identical within experimental error with the parameter found for the ordered structure (6.29 ± 0.002A°). This process was repeated on the compounds $Hg_5In_2\square Te_8$ and $Hg_5Ga_2\square Te_8$ with no result, the compounds remaining ordered for all annealing temperatures below the melting point. When $Hg_3Ga_2\square Te_6$ was also put through the same process, a change did occur between 400°C (673°K) and 500°C (773°K); the structure remained cubic but the lattice parameter changed from 6.21A° at 400°C to 6.01A° at 500°C. It was not shown conclusively that an order-disorder transformation occurred for this compound, but there is a phase change of some kind. This result is inconclusive because the high temperature at which this phase change occurs allows the material to lose mercury quite easily, consequently the effect was not investigated further.

While numerous metallic substitutional alloys exhibit an order-disorder transformation, the classic example being copper-gold alloys, the phenomenon has not been widely reported in a semiconducting material. It would appear then, that the compound $Hg_3In_2\square Te_6$ presents an

unusual variation and because of this it was thought useful, if possible, to measure the electrical behaviour in the vicinity of the transition. The ultrasonic measurements reported in this thesis have all been made on ordered crystals.

2.6 THE EFFECTS OF AN ORDER-DISORDER TRANSFORMATION ON SOME PHYSICAL PROPERTIES

In the previous section an order-disorder transformation occurring in crystals of the compound $Hg_3In_2\square Te_6$ was investigated using Debye-Scherrer *x*-ray techniques; it was found, as evidenced by the reducing intensity of the superlattice lines that the material became more disordered as the temperature was increased until ordering of the superlattice was completely destroyed at a critical temperature of $332 \pm 5^{o}C$. The sharpness of the superlattice lines indicates that it is long range order, in which the atoms are arranged in a specific array, rather than short range order which is being destroyed; the long range order parameter p becomes zero above the critical temperature. Short range order occurs when the ordering forces are weak, so that each atom may succeed in surrounding itself with unlike atoms for short periods of time and on average it is surrounded by more unlike atoms than it would be in a completely random arrangement.

Although *x*-ray studies on quenched specimens are perhaps the most direct method of investigating this phenomenon, any order dependant property is of interest and its measurement may, even if only indirectly help in elucidating the nature of ordered structures; certainly the information of effects of order on some bulk properties will contribute to understanding the actual mechanics of going through the transformation from an ordered to a disordered state. Some information is available on metallic alloys but measurements of the

effects on the electrical properties of a semiconducting material on going through this transition are scarce. Electrical measurements on $Hg_3In_2\square Te_6$ also serve to compare the material grown in the single crystal form for the ultrasonic experiments with the material produced by other workers. This is effective since it has been found that the electrical properties are dependant on an excess element in the compound, in particular mercury (Dahake 1967).

The order-disorder transformation, which is a co-operative phenomenon like the loss of ferromagnetism at the curie point, is attractively illustrated by A. H. Lipson's (1950) analogy: "It may be compared to the behaviour of a crowd of people; if one or two look up fixedly at the sky others may not be induced to do likewise, but if more people look upwards the inducement of others to do so becomes greater until when nearly everybody is looking up, the urge to do so is irresistible even for the most obstinate individual." The change frequently occurs over a temperature range of several hundred degrees as has been indicated by the specific heat plots of $CuZn$ (β brass) and Cu_3Au. In each case the smooth increase in the absence of an order-disorder transformation, is interrupted by a peak prior to the transition temperature; this suggests that energy is required not only to increase the vibrational motion of the atoms but also to enable some of the atoms to exchange places. Once disordering has started, the process rapidly increases until at the critical temperature, the phase is almost completely disordered and the specific heat curve returns to a value virtually the same as that required by a normal smooth specific heat curve. This peak (Figure 2.19) has been observed qualatively, in this material between 300^oC and 320^oC using a Perkins Elmar differential scanning calorimeter. In this type of scanning calorimetry the temperature of the sample

and a reference is increased in a controlled manner and are continuously maintained at the same level. This is accomplished by a negative feedback loop to control the power which is supplied to the sample and reference holders. When the sample absorbs or releases energy, more, or less power is required by the sample holder to maintain it at the same temperature as the reference holder. It is this differential power, continuously and automatically varied according to the energy requirements of the sample, which is recorded as an ordinate on the chart recorder. Since power is energy per unit time, the instrument records the rate of energy absorption as a function of sample temperature. Consequently, Figure (2.19) represents an endothermic reaction and because the recorder had a linear time base the area of the peak is equivalent to the energy required by the reaction.

The electrical properties, resistance, Hall coefficient and thermoelectric power were measured carefully on taking the sample through the transition region in a furnace (Figure 2.20) which consisted of two concentric quartz tubes. The 1 inch diameter inner quartz tube carried the heater which was made of kanthol wire. The space between the tubes was filled with alumina cement which insulated the furnace and held the heater wire in position. By spacing the winding turns a temperature profile having a flat plateau with steep sides was obtained, enabling the samples in both the Hall and resistivity experiments to be placed such that the temperature was constant over their length. This is not the requirement for thermoelectric experiments and in this case the sample was placed in a steep temperature gradient. The temperature of the furnace, and consequently the profile, was controlled by a Eurotherm controller of the type described in section (2.2).

Two sample holders were designed, one for measuring the Hall coefficient and resistivity (Figure 2.21) and the other for the thermoelectric power measurements (Figure 2.22). The base in each case was machined from sindanyo, an excellent thermal and electrical insulator. This allowed the samples to be heated to temperatures in excess of $330^{o}C$. Samples used for Hall and resistivity measurements were cemented between copper current contacts with a silver solution (Aquadag) and phosphor bronze pressure probes were employed to measure the appropriate potential. To avoid the shorting effect of the large area current contacts used, the length to width ratio of the Hall samples was greater than 3 (Isenberg et al 1948). The geometry of the resistivity samples also conformed to the requirements of Stephens et al (1971) who have shown that the resistivity can be obtained using the uncorrected expression

$$\rho = \frac{VA}{IS} \qquad (2.7)$$

where V is the potential difference, A is the area of the cross section, I is the total current and S is the potential contact separation, provided that the sample has a length to width ratio of 3 and its thickness is no greater than the width but not less than half the width and the potential contact separation is not greater than half the length of the sample. In each case the sample length was about 14 mm. The sample holder used for the thermoelectric measurements held two copper-constantan thermocouples in position with a phosphor bronze spring arrangement. These thermocouples also served the dual purpose of acting as potential contacts. In each type of measurement the potential was measured by a Tinsley potentiometer capable of measuring to $0.1\mu V$.

The circuit used to measure the resistivity and the Hall coefficient

(Figure 2.23) was basically the same except for the position of the potential probes. A constant current supply was used, for convenience and to allow accurate measurements. This was achieved using a simple transistor circuit which held the current constant to within *0.1%* over a resistance change in the sample between *5Ω* and *5kΩ*. The magnet used in the Hall measurements was also driven by a constant current supply capable of delivering up to *13A*, which was sufficient to provide a constant field of maximum strength of about *6.5 k gauss*. In order to measure the Hall voltage at several field values the magnet was calibrated with a Hall probe gaussmeter.

The usual steps were taken to obtain accurate measurement; for example in the case of the Hall measurements the potential which existed due to slight misalignment of the probes was backed off by a constant voltage supplied by a Tinsley potentiometer, measurements were also taken with both positive and negative current and field directions at about eight values of field strength at each temperature. The variation of Hall potential with field strength at each temperature was found to be a simple linear graph and the coefficient R_H was taken from the gradient (Figure 2.24). This behaviour is in common with that found by previous workers on this series of compounds.

The electrical resistivity is *35 ohm cm* at room temperature and falls in a linear manner with increasing temperature (Figure 2.25) due to intrinsic behaviour, a pattern consistent with previous results. Dahake (1967) and Spencer (1964) on single and polycrystalline specimens have shown that the resistivity is sensitive to a change in the most volatile element, mercury, by annealing in a vacuum and mercury vapour. A value of *35 ohm cm* falls within the range of these results presented for comparison in Table (2.6). This temperature dependant resistivity curve is unusual in that its linearity is abruptly changed at *300±5°C* and at *322±5°C* the curve again becomes linear.

The slope undergoes a distinct change and the kink which develops occurs over the temperature interval at which the order-disorder transformation occurred in the quenching experiments. It appears then that this measurement will allow an improved assessment of the temperature interval over which the order-disorder transformation occurs and assuming that the curve becomes linear when disordering is complete, the critical temperature T_c equals $322\pm5^{o}C$. The change in the slope of the curve on passing through the transition temperature suggests, since the material is intrinsic, that there is a change in the energy gap. Further quenched disordered samples have room temperature resistivities which are lower than in the ordered state and tend to fall on the extrapolated curve of the resistivity when in the disordered state. This behaviour is contrary to that observed in metals, for example in the copper gold system at the composition Cu_3Au and $CuAu$ which have a tendency to order, there is a corresponding reduction in the resistivity values at room temperature. The explanation advanced is that the increase in the periodicity of the lattice due to ordering reduces the scattering. It would appear then, that in this semiconducting compound there is an increase in the band gap on ordering which is the dominating effect, causing the resistivity to be greater than that of the disordered material at room temperatures. This also explains some anomolies in results of this type of measurement (Table 2.6) obtained by previous workers. Hence, it would be reasonable to conclude, that even though the stoichiometry of the material at these temperatures is changing due to a loss in mercury and thereby altering the measurements, the change in the resistivity curve between $300\pm5^{o}C$ and $322\pm5^{o}C$ is due primarily to an order-disorder transformation having taken place and this will effect the band gap. The effect of changing the stoichiometry has been demonstrated by annealing samples in mercury

vapour with a consequent reduction in the resistivity which is linked with both the annealing time and the temperature. The kink which occurred in the resistivity measurements also occured in the curve of the thermoelectric power measurements (Figure 2.26) at the same temperature.

The Hall coefficient R_H at room temperature is $2100\ cm^3/C$ a value consistent with the doping level indicated by the resistivity measurements and within the range of values given in Table (2.6). These measurements show that the material is p type. The temperature dependance of R_H is normal, the curve becoming linear due to intrinsic behaviour at about 150^oC. Once again, a kink in the curve during the transition temperature interval after which the slope assumes a new value (Figure 2.27). As before this kink occurs over a temperature interval between 300 ± 5^oC and 322 ± 5^oC. The carrier density (Figure 2.28), was obtained using

$$R_H = \frac{3}{4}\pi^{\frac{1}{2}}\frac{1}{ne}\frac{F(2S+5/2)}{F^2(S+5/2)} \qquad (2.8)$$

where a scattering parameter of S equal to zero was assumed for the gamma function. This follows Wright and Dahake (1968) who used this value because of the quasi-metallic behaviour exhibited by alloys in this series which have less than $20\%\ In_2Te_3$ content, even though for their samples of 50% and 75% composition degeneracy is only partial, as is the case here. This calculated carrier density was then substituted into

$$n_c = n_h = 2\left(\frac{2\pi kT}{h^2}\right)^{3/2}(m_e^* m_h^*)^{3/4}\, e^{-Eg/2kT} \qquad (2.9)$$

which relates, in the intrinsic region, the density of electrons in the conduction band n_c and the density of holes in the valence band n_h to temperature and the effective mass of the carriers m_e^* and m_h^*. The band gap *Eg* was then obtained from the slope *Eg/2kT* of a plot of $log\ n_c/T^{3/2}$ against *1/T* (Figure 2.28). The values obtained are *0.37eV* for the ordered phase and *0.21eV* for the disordered phase; this change of *0.16eV* on going through the transition indicates that the band structure is profoundly modified when the atoms rearrange themselves. These results confirm the resistance measurements, where the resistivity of the disordered material is less than the resistivity of ordered material. Comparison with the results obtained by previous workers can only be tentative, because they were mainly concerned with measurements below room temperature. However, Dahake (1967) did measure the Hall coefficient R_H on single crystal samples from 77^oK to about 400^oK ($\sim 130^oC$). For some samples, the curve obtained of R_H against *1/T* was linear over a temperature range from about 60^oC to about 130^oC, the material being intrinsic. This allowed the band gap to be estimated and the results presented in Table (2.7) are interesting. The as grown sample which was found by Dahake to be disordered has a band gap of *0.165eV* and sample (5) which was annealed for *100 hours* at 250^oC, a process which causes ordering, has a band gap of *0.34eV*. Sample (2), which was annealed at 300^oC for *75 hours* has an energy gap of *0.075eV*, this possibly suggests an increasing degree of disorder; in fact the electrical measurements and especially the differential calorimeter curve (Fig. 2.19) indicate that disordering is well under way at this temperature. Because of the limited temperature range over which the samples exhibited intrinsic behaviour, these calculations are approximate, but they are consistent with the measurements obtained here of *0.37eV* (ordered) and *0.21ev* (disordered).

Table (2.6) Resistivity of $Hg_3In_2\square Te_6$ at 300^oK by Dahake (1967)

Sample	ρ ohm cm	Remarks
1	*500*	*as grown*
2	*100*	*annealed in vacuum for 75 hours at 300°C*
3	*230*	*annealed in vacuum for 50 hours at 250°C*
5	*10*	*annealed in Hg for 100 hours at 250°C*

Table (2.7) Energy gaps calculated from the results obtained by Dahake (1967)

Sample	Eg (eV)	Remarks
1	*0.165*	*as grown, disordered*
2	*0.075*	*annealed in vacuum for 75 hours at 300°C*
5	*0.34*	*annealed in Hg for 100 hours at 250°C*

Heating a sample to these temperatures can cause a change in its stoichiometry which effects the electrical properties, to assess this effect a Hall sample was annealed at *200°C* for *40 hours* and the measurements repeated. The percentage fall in carrier density at a temperature of *143°C*, where the material started to become intrinsic was *48%*. This allowed a rough estimate to be made of the percentage change in carrier density which was about *6%* during the time required to take the measurements over the full temperature range. Therefore, these measurements must be treated with caution, but they do indicate together with the *x*-ray quenching experiments that a change occurs between the temperature interval *300°C* to *320°C*, which is consistent with an order disorder transformation having taken place.

The main result of this work is to show that the lowest minimum in the conduction band characteristic of the disordered material should separate more widely from the highest valence band maximum when ordering occurs, because of the reduction in entropy and the resulting increase in the strength of some of the bonds. The direct effect is for the energy gap to increase. This has also been observed in In_2Te_3 (Gasson et al 1960) and in certain solid solutions III_2-VI_3 and *II-VI* compounds (Spencer et al 1962). However, other conduction band minima may fall towards the valence band since other bonds may decrease in strength. In some cases this might lead to a net decrease in energy gap. Since ordering alters the symmetry of the crystal and usually means that a larger unit cell must be used to describe its lattice, the Brillouin zone shape will usually change and if it does its size will decrease. Even if the Brillouin zone does not change, the electronic band structure, especially in the conduction band, may alter because of the periodicity changes. The shape and potential energy of existing minima may become different and fresh minima may appear or old ones shift position in *k* space. Any of these alterations would produce change in effective mass and therefore in the transport properties.

Equilibrium diagram of Hg_3Te_3-Ga_2Te_3

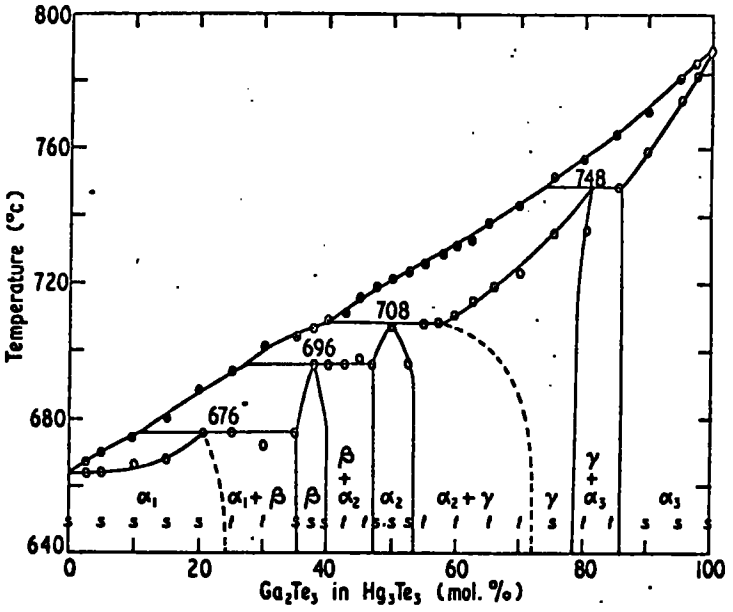

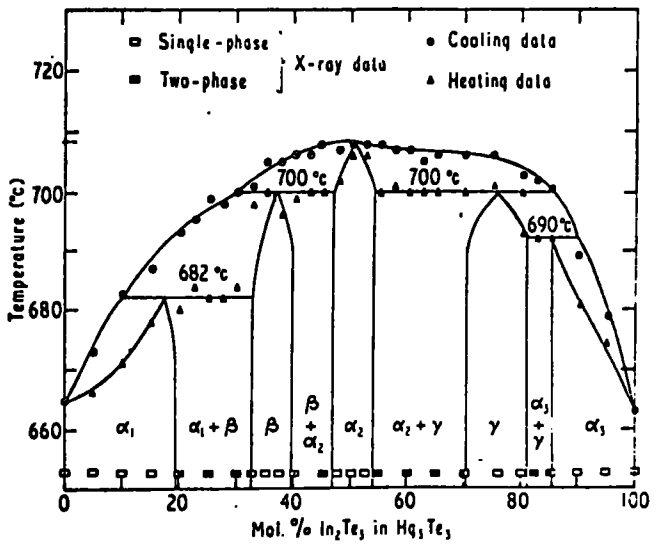

Phase diagram of the Hg_3Te_3-In_2Te_3 alloy system.

Fig. (2.1) and (2.2) Phase Diagrams

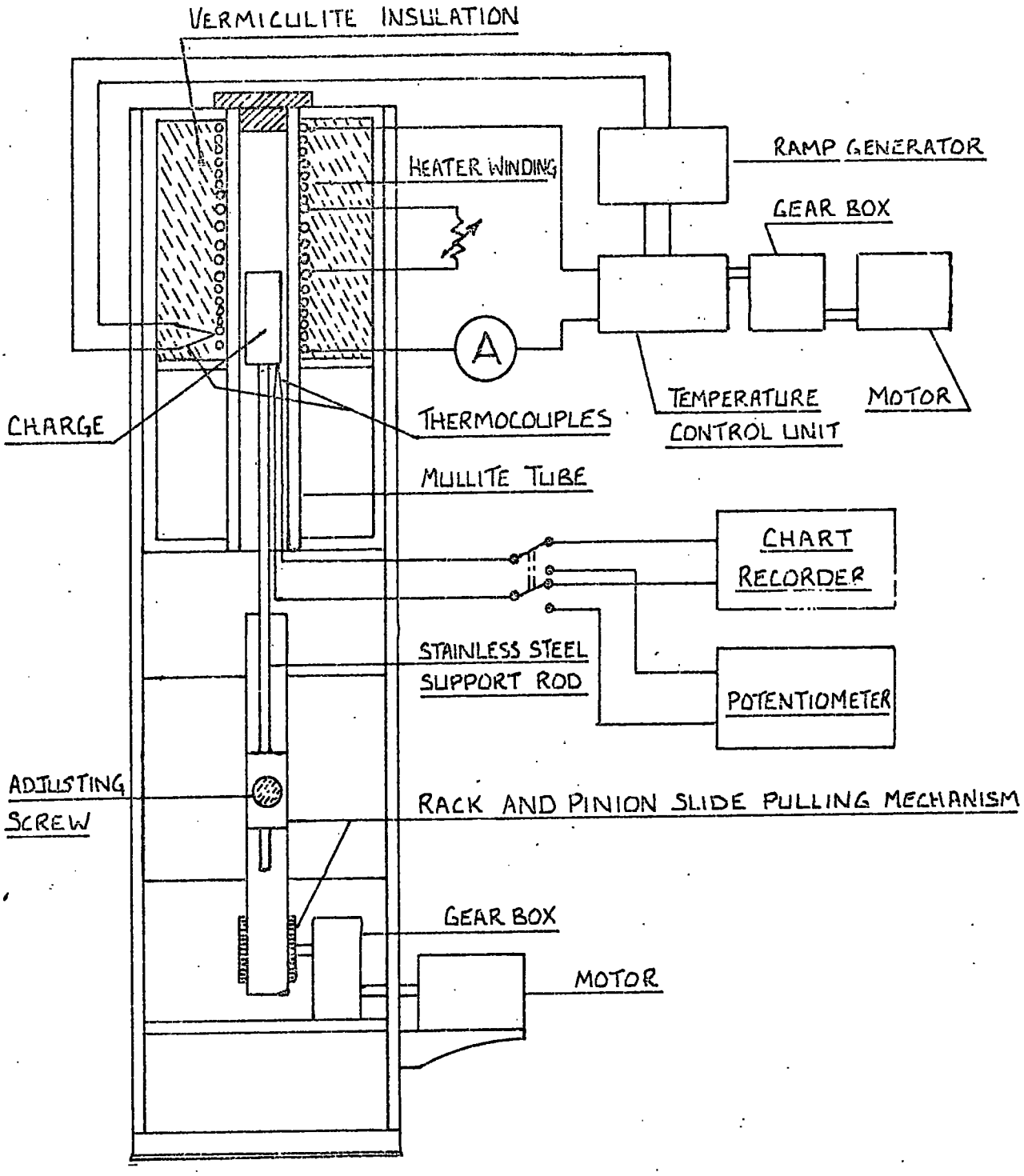

Fig. (2.3) Crystal Growth Furnace

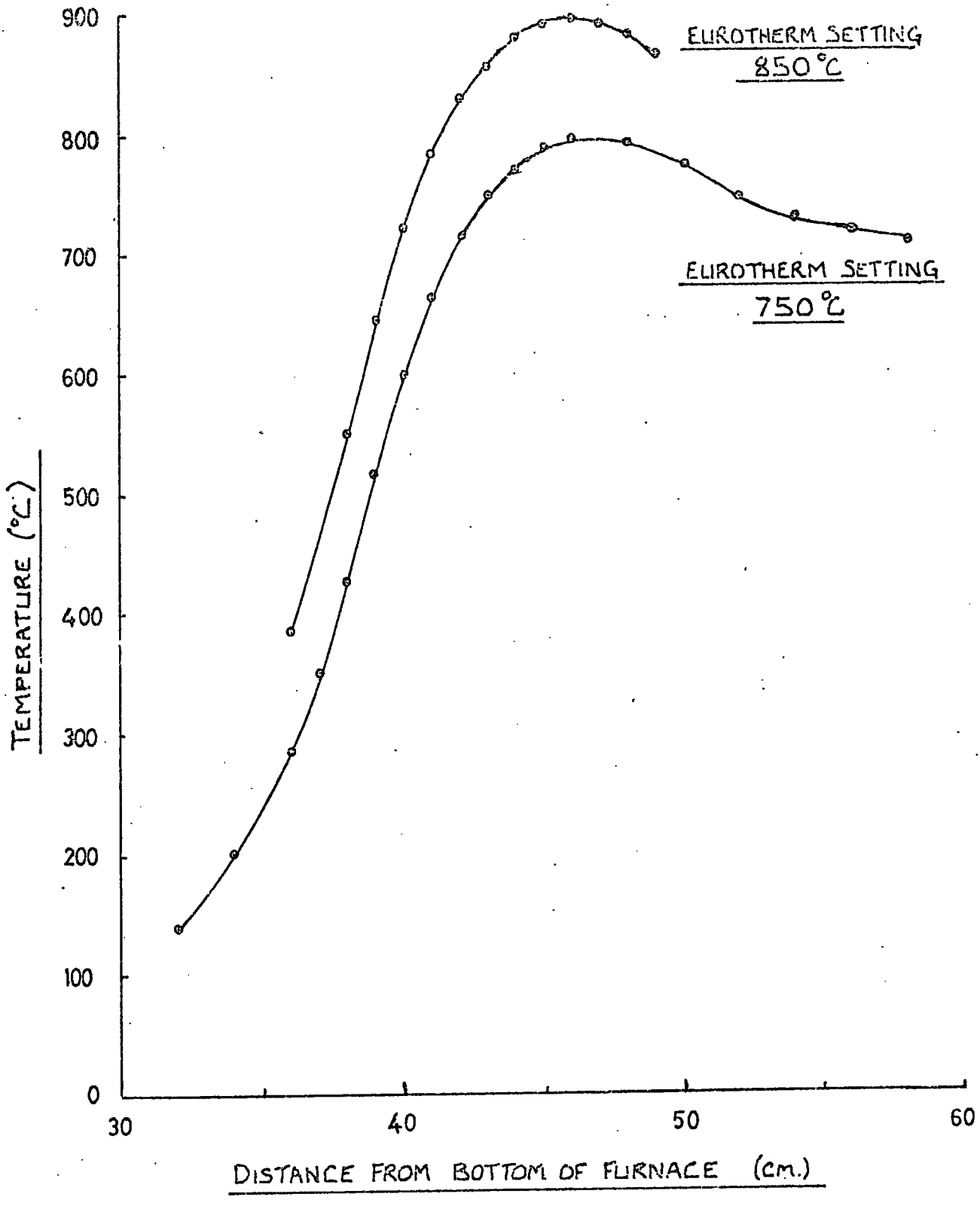

Fig. (2.4) Temperature profile of the furnace

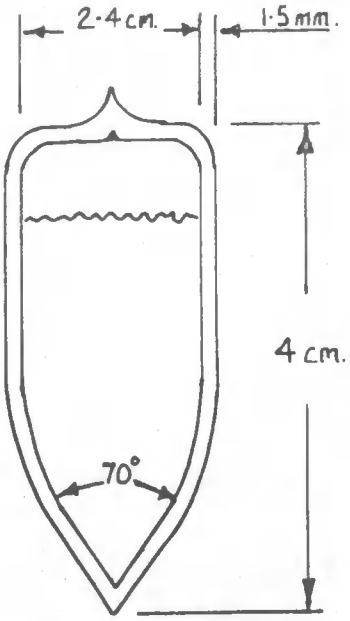

Fig. (2.5) The diagram gives the dimensions of the most successful type of crucible and the photograph illustrates the appearance of a boule.

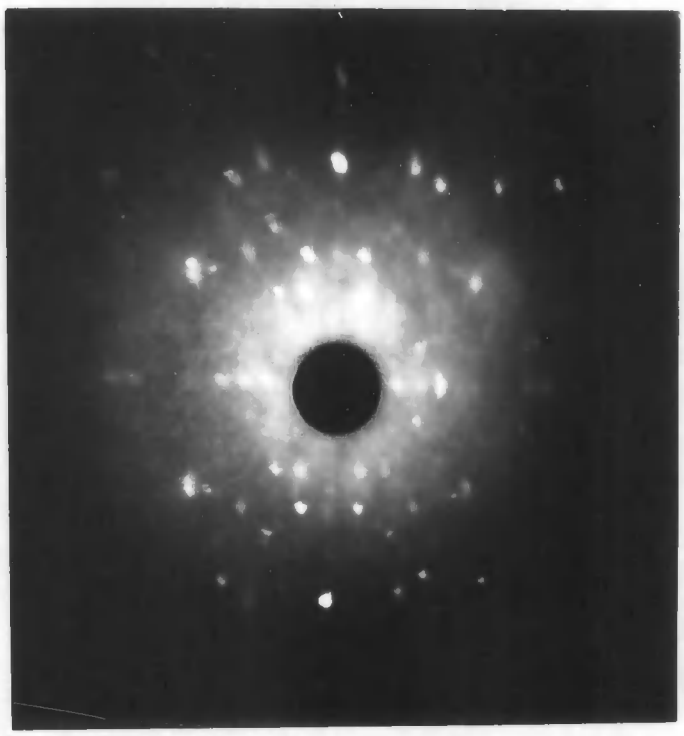

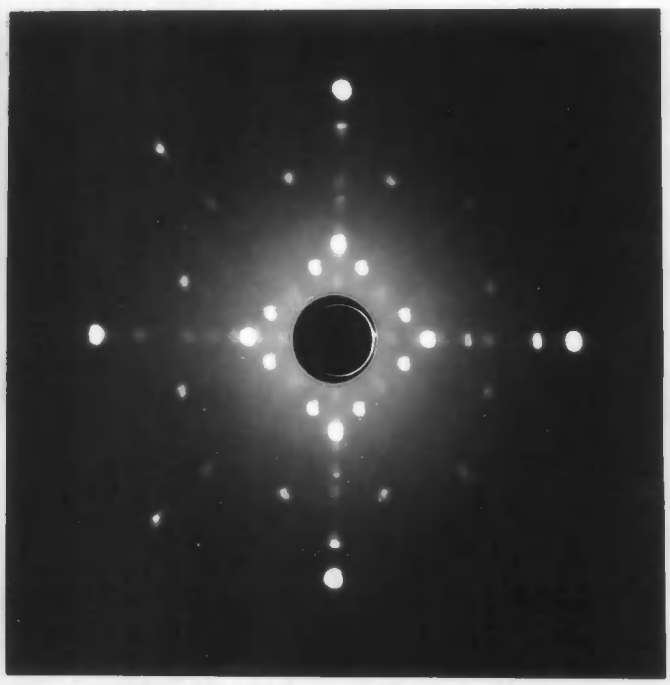

Fig. (2.6) Laue photographs showing 2-fold, 3-fold and 4-fold symmetry of $Hg_3In_2\square Te_6$ crystals.

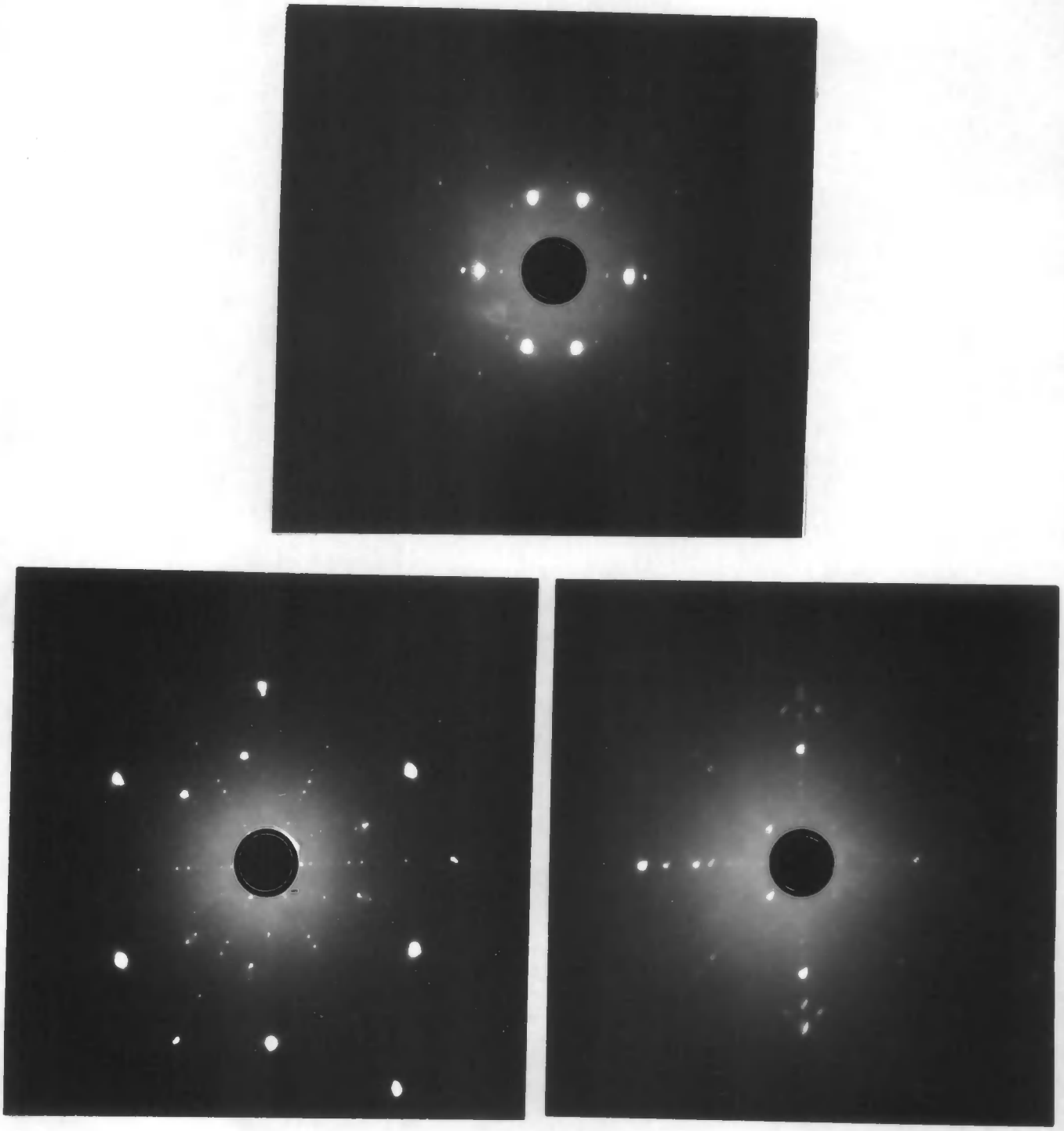

Fig. (2.7) Laue photographs showing 2-fold, 3-fold and 4-fold symmetry of $Hg_5Ga_2\square Te_8$ crystals.

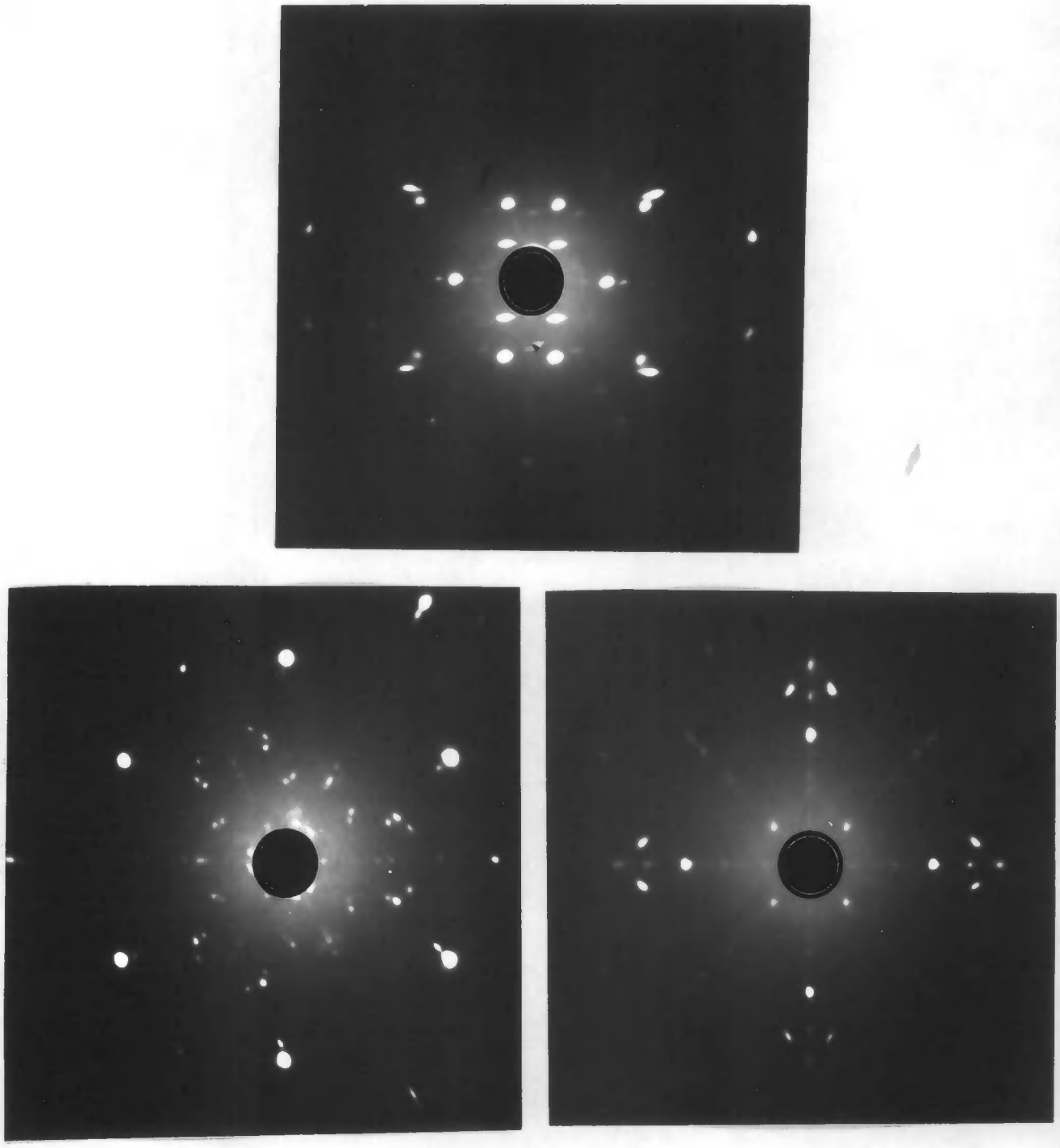

Fig. (2.8) Laue photographs showing 2-fold, 3-fold and 4-fold symmetry of $Hg_3Ga_2\square Te_6$ crystals.

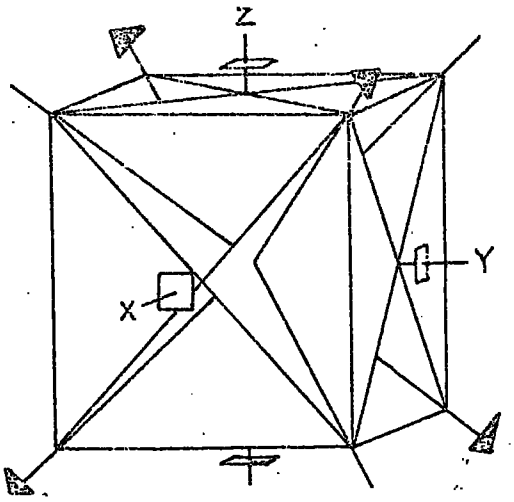

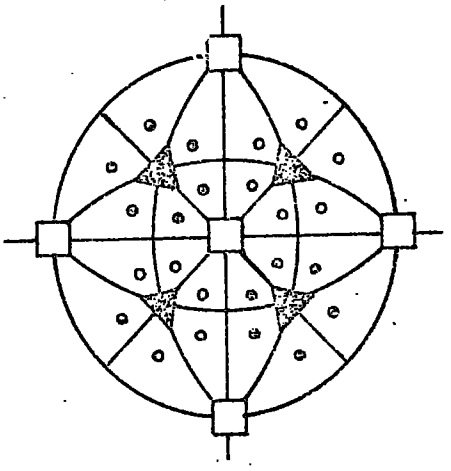

Fig. (2.9) Elements of symmetry and stereogram of the $\bar{4}3m$ point group.

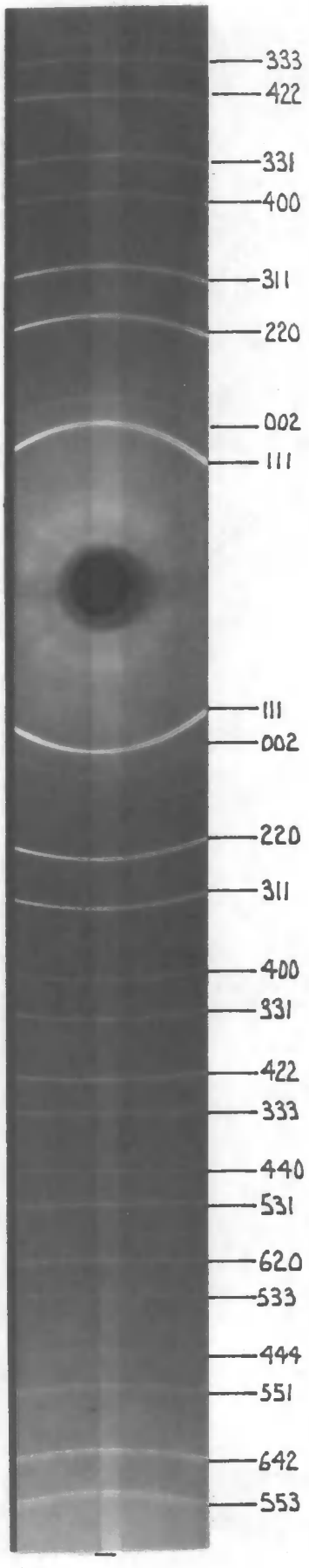
333
422
331
400
311
220
002
111
111
002
220
311
400
331
422
333
440
531
620
533
444
551
642
553

HgTe

Fig. (2.10)

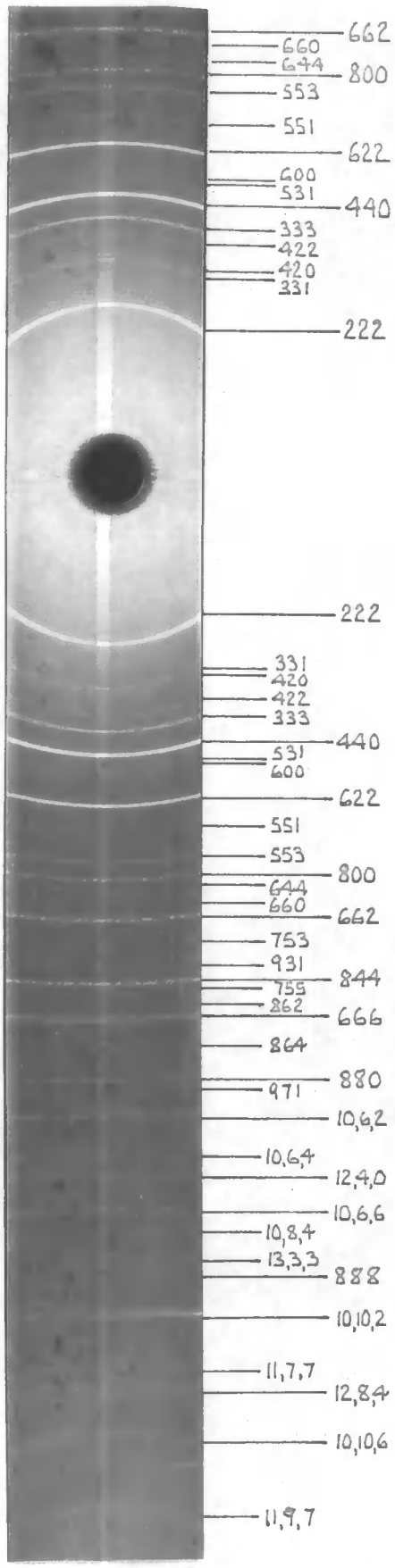

Fig. (2.11)

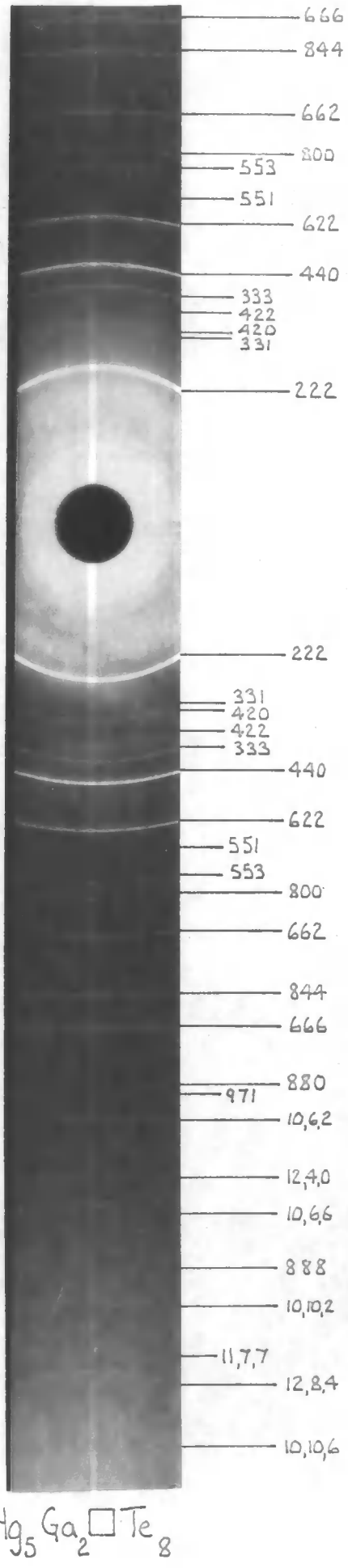

Fig. (2.12)

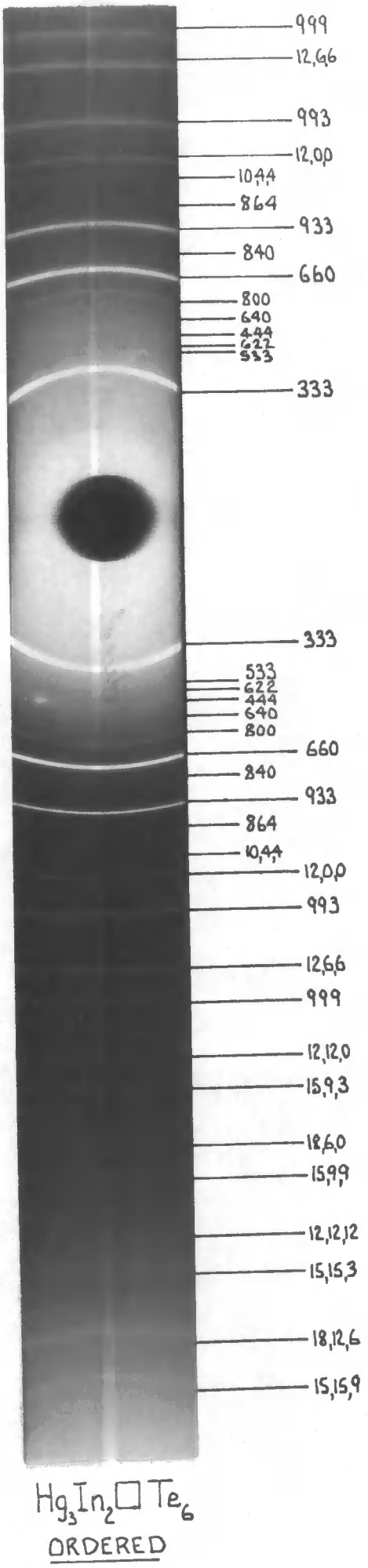

Fig. (2.13)

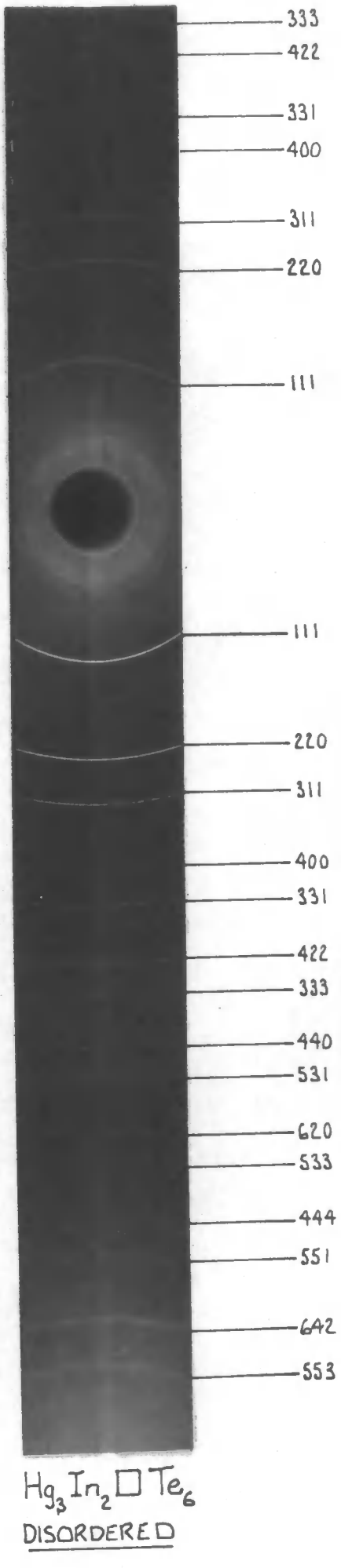

Fig. (2.14)

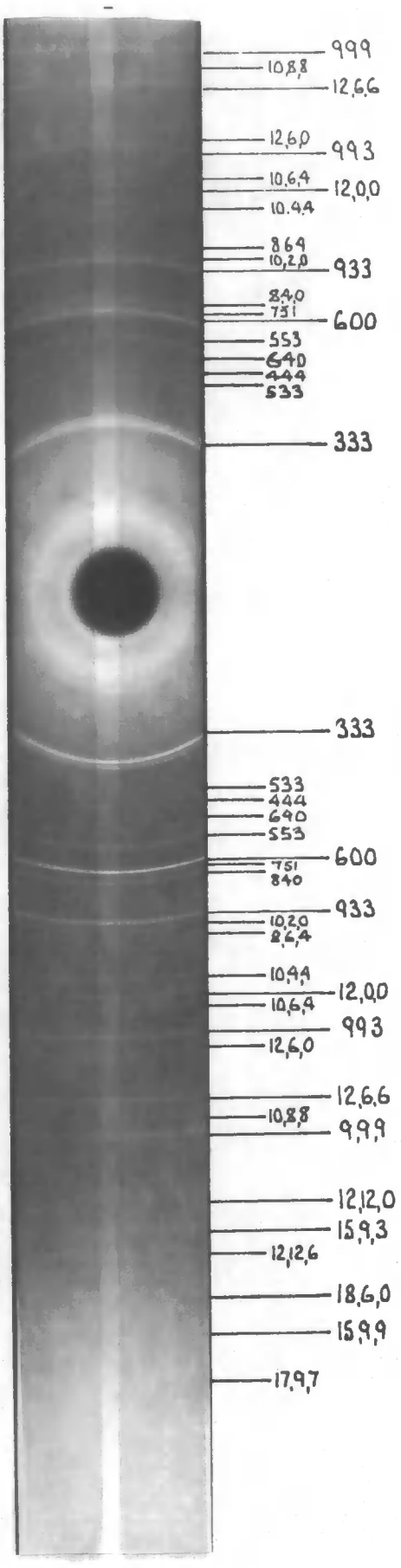

$Hg_3Ga_2\square Te_6$

Fig. (2.15)

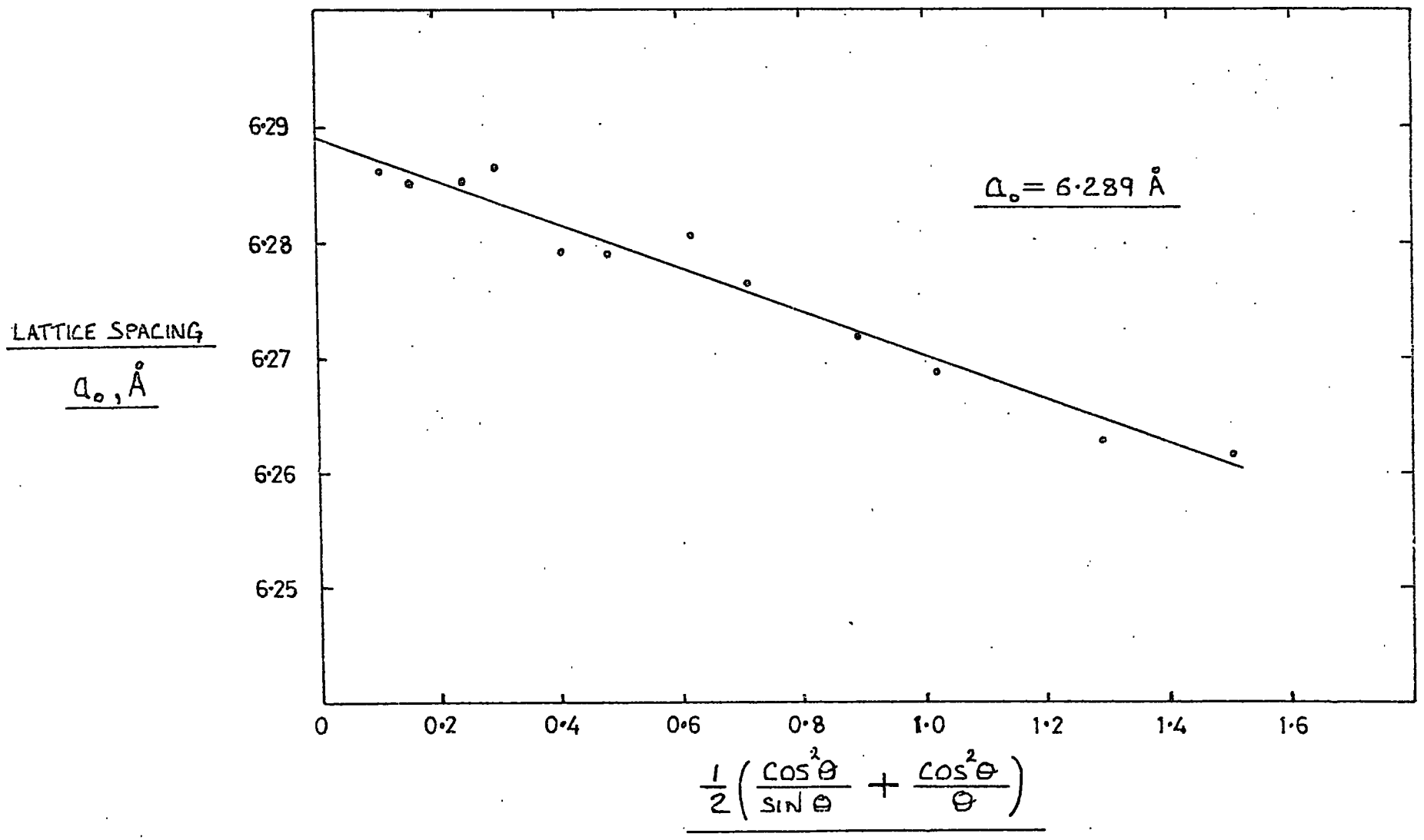

Fig. (2.16) Nelson-Riley plot of $Hg_3In_2\square Te_6$

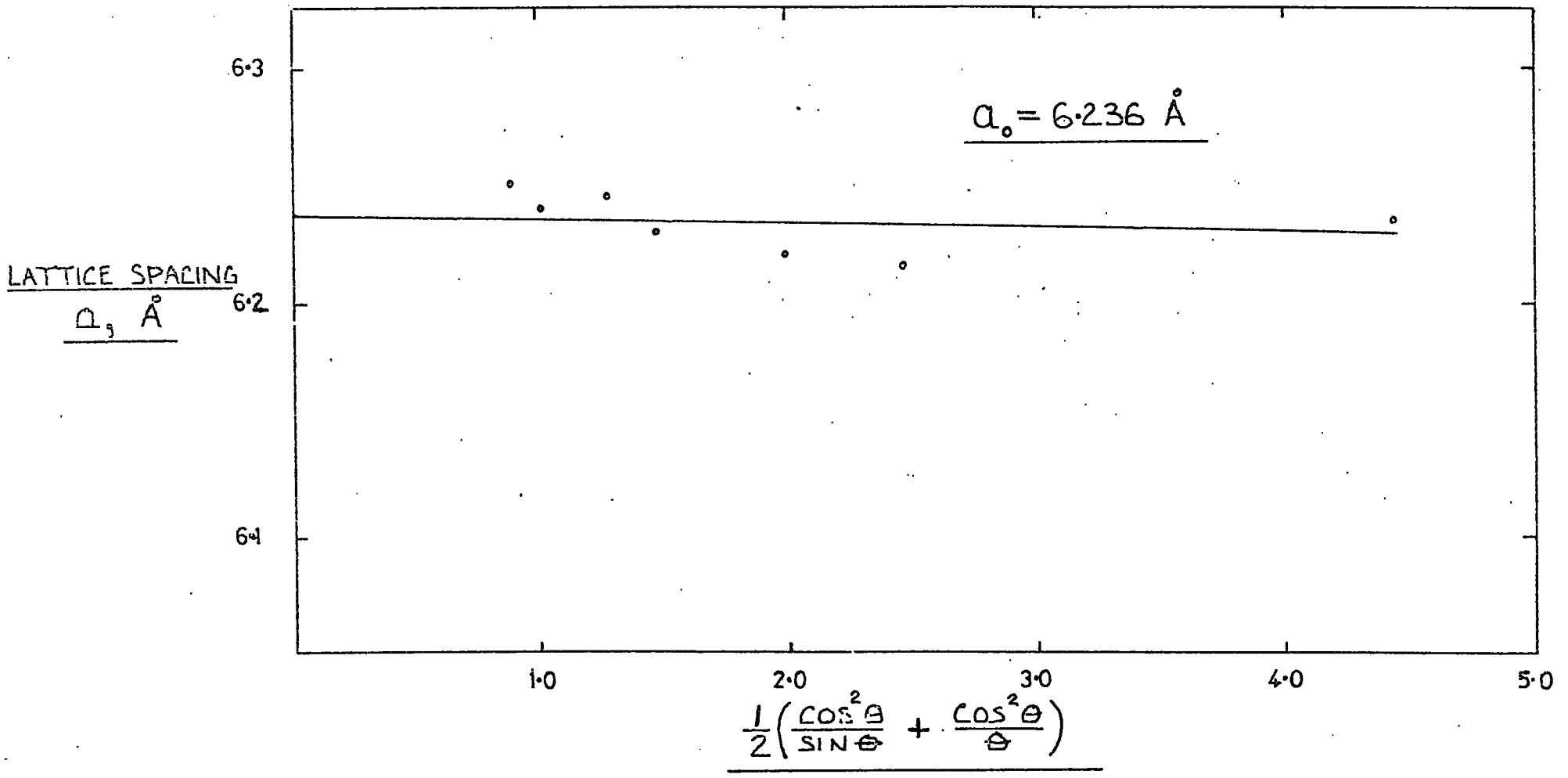

Fig. (2.17) Nelson-Riley plot of $Hg_5Ga_2\square Te_8$

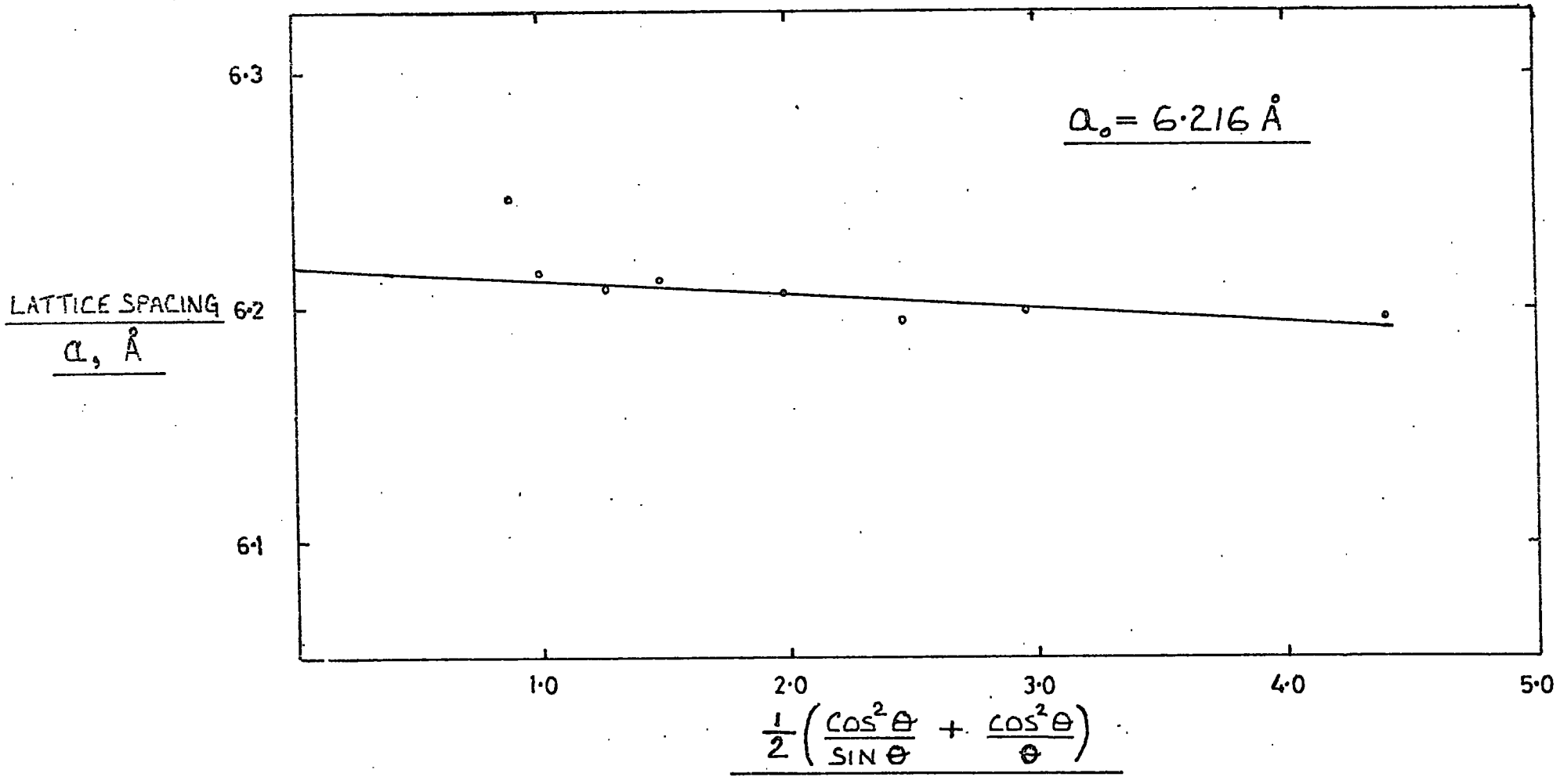

Fig. (2.18) Nelson-Riley plot of $Hg_3Ga_2\square Te_6$

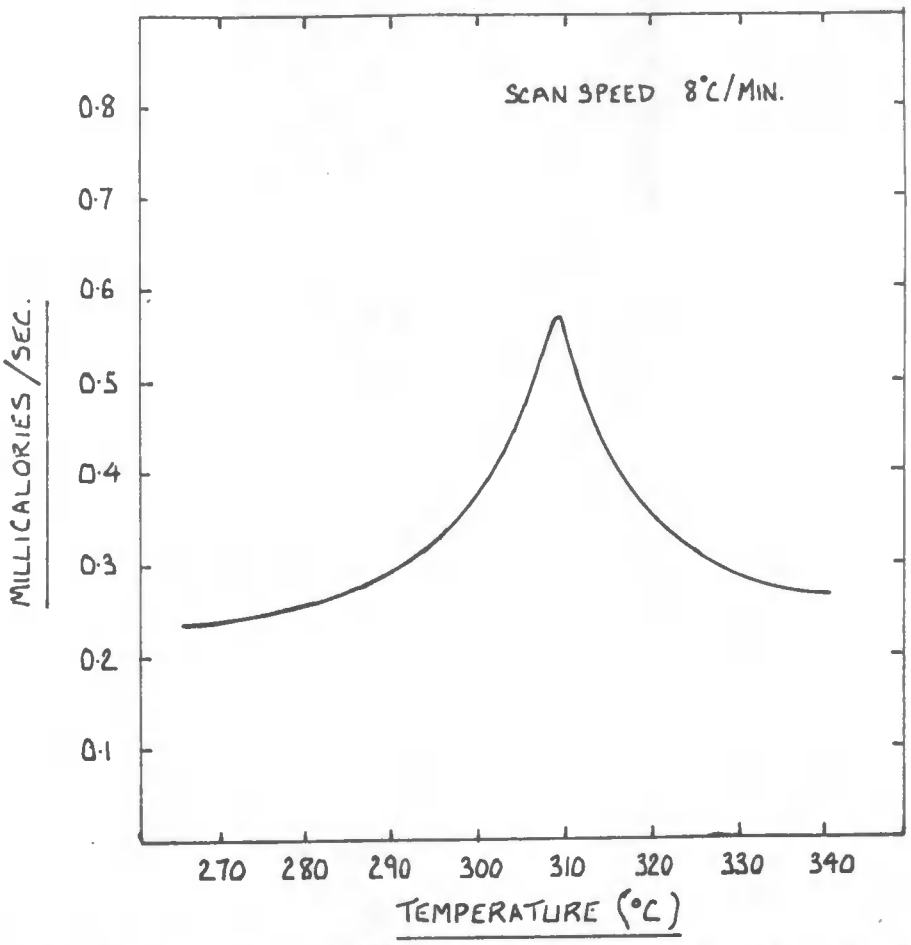

Fig. (2.19) Trace produced by scanning calorimeter on going through the order-disorder transistion in $Hg_3In_2\square Te_6$.

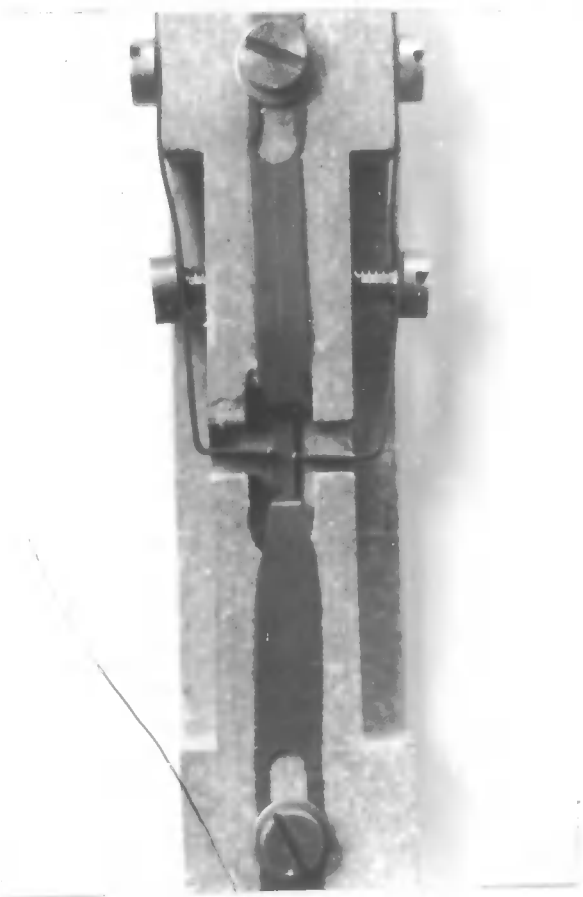

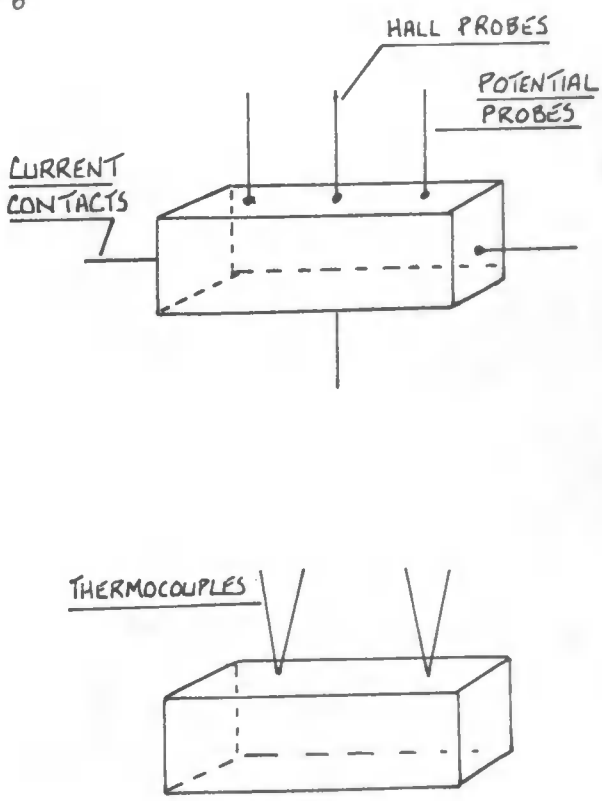

Figs. (2.21) and (2.22) Basic sample holder and modifications required for each electrical measurement.

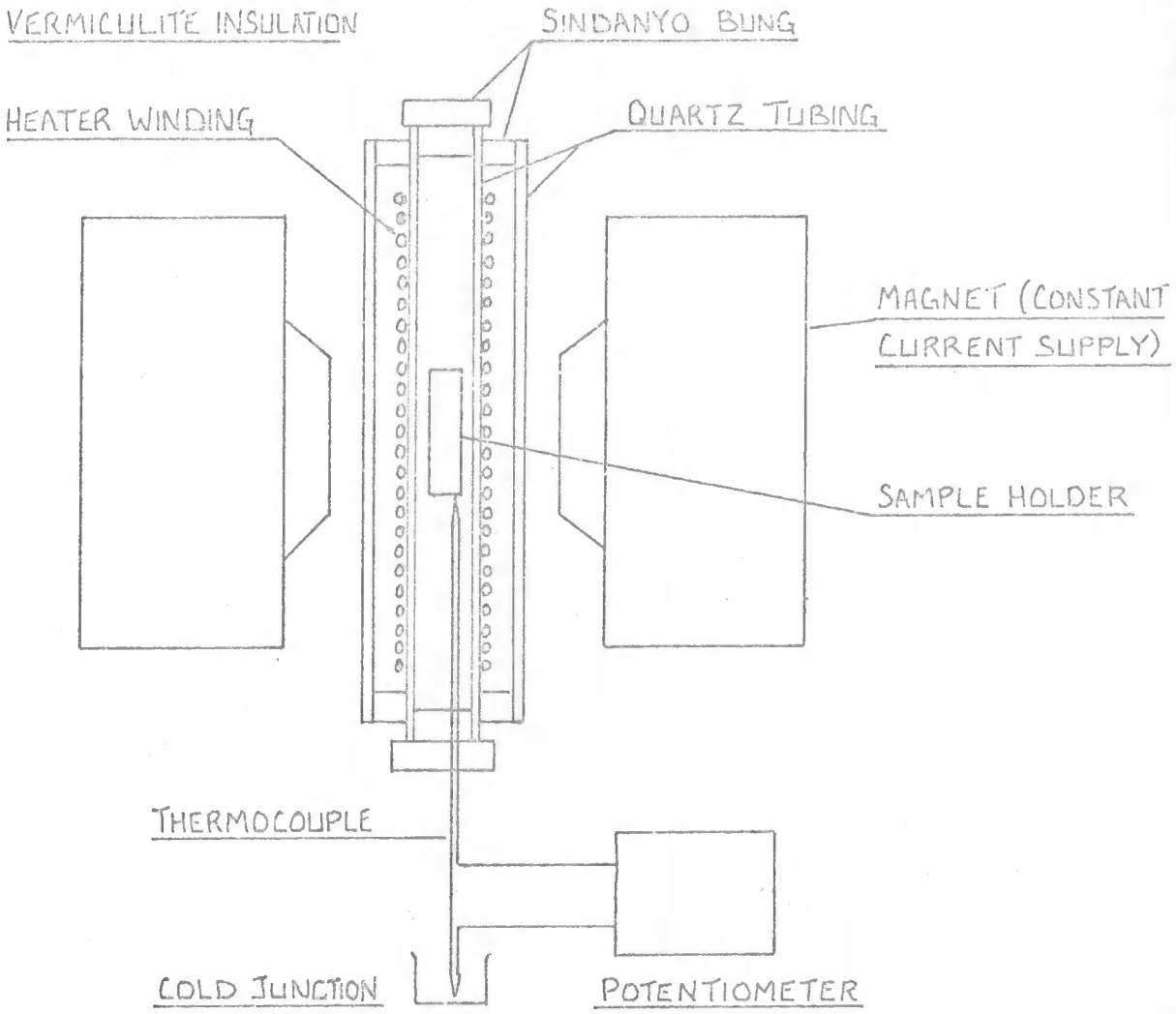

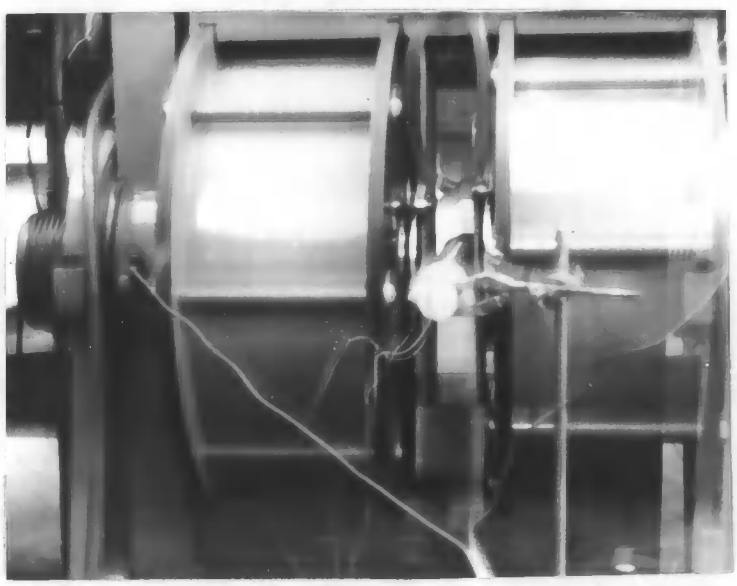

Fig. (2.20) Furnace used for the electrical measurements

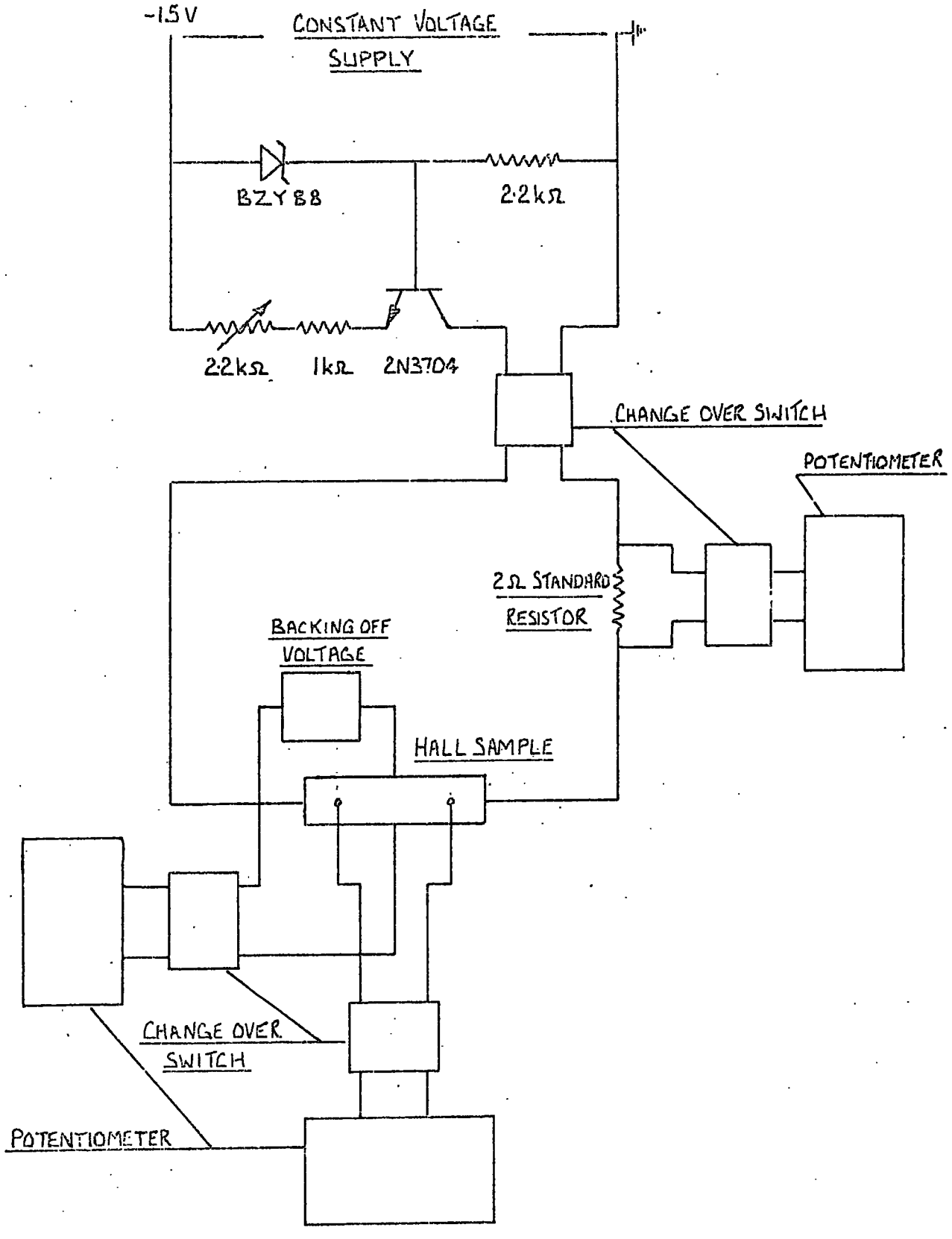

Fig. (2.23) Circuit used for Hall and resistance measurements.

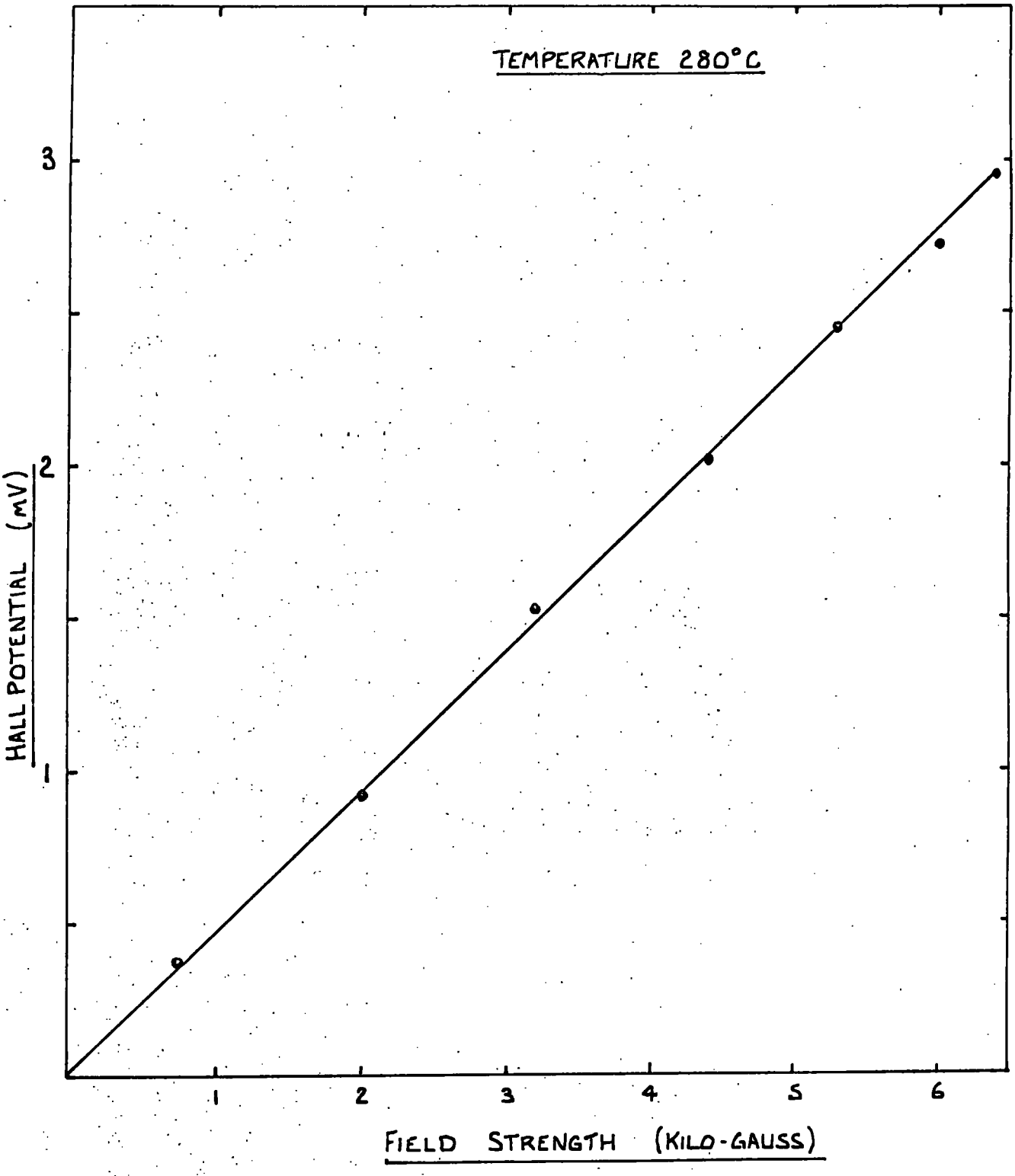

Fig. (2.24) Showing the linear relationship obtained between Hall potential and field strength at a fixed temperature.

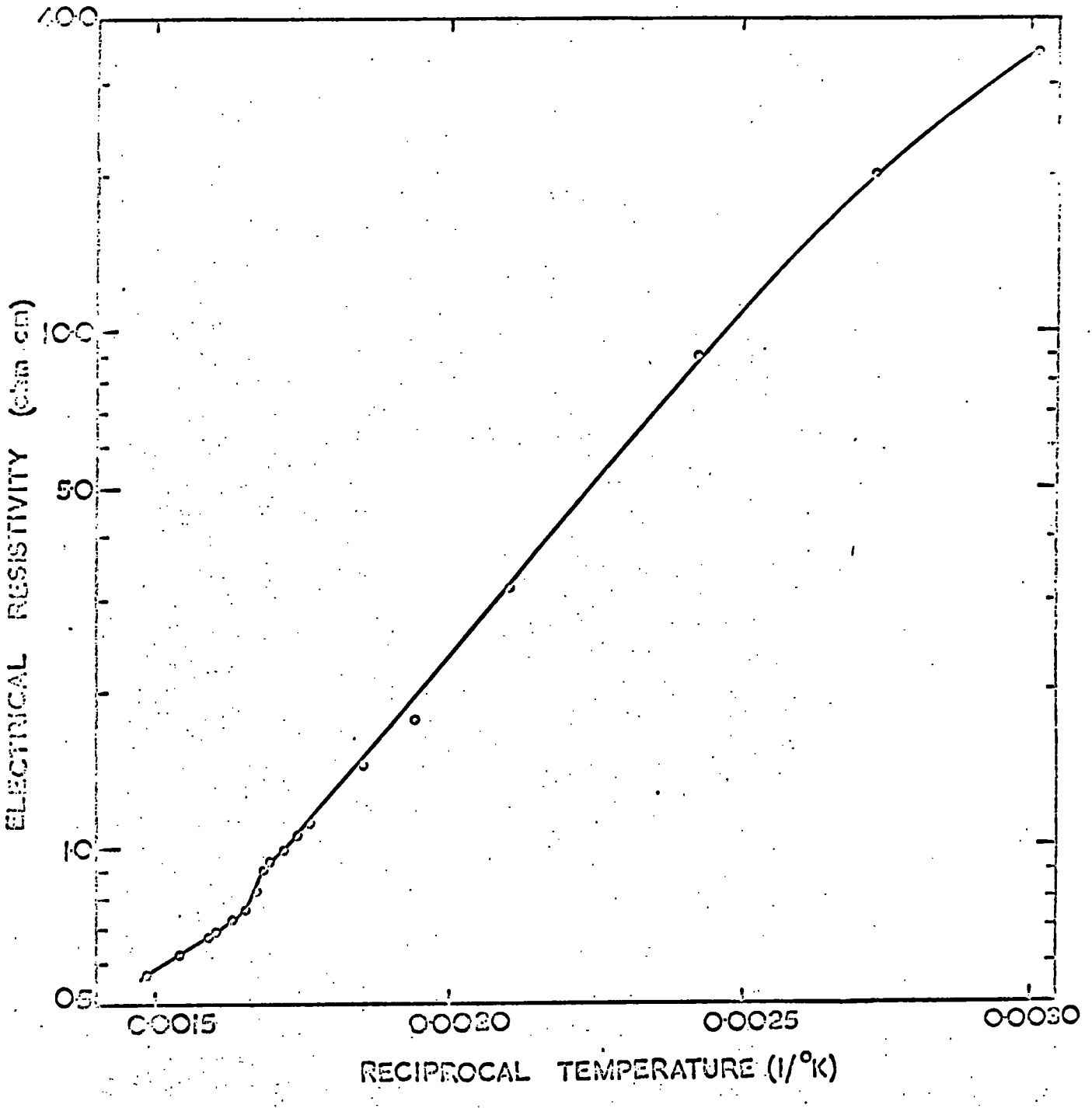

Fig. (2.25) The electrical resistivity of $Hg_3In_2\square Te_6$ plotted against the inverse temperature. The slopes are markedly different in the two phases as a result of the change in the energy gap.

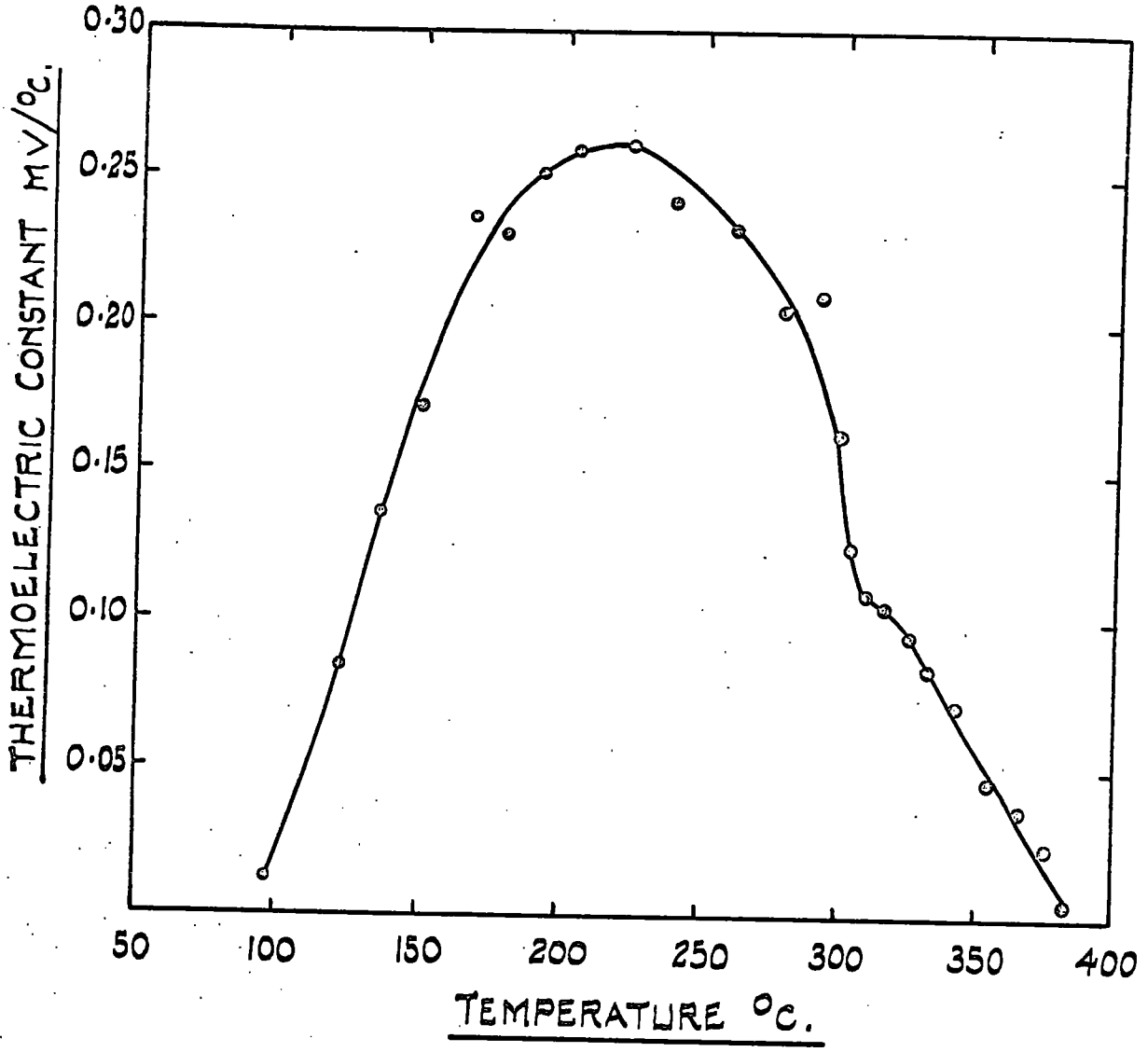

Fig. (2.26) Temperature dependence of the thermoelectric power through the order-disorder transistion in $Hg_3In_2\square Te_6$.

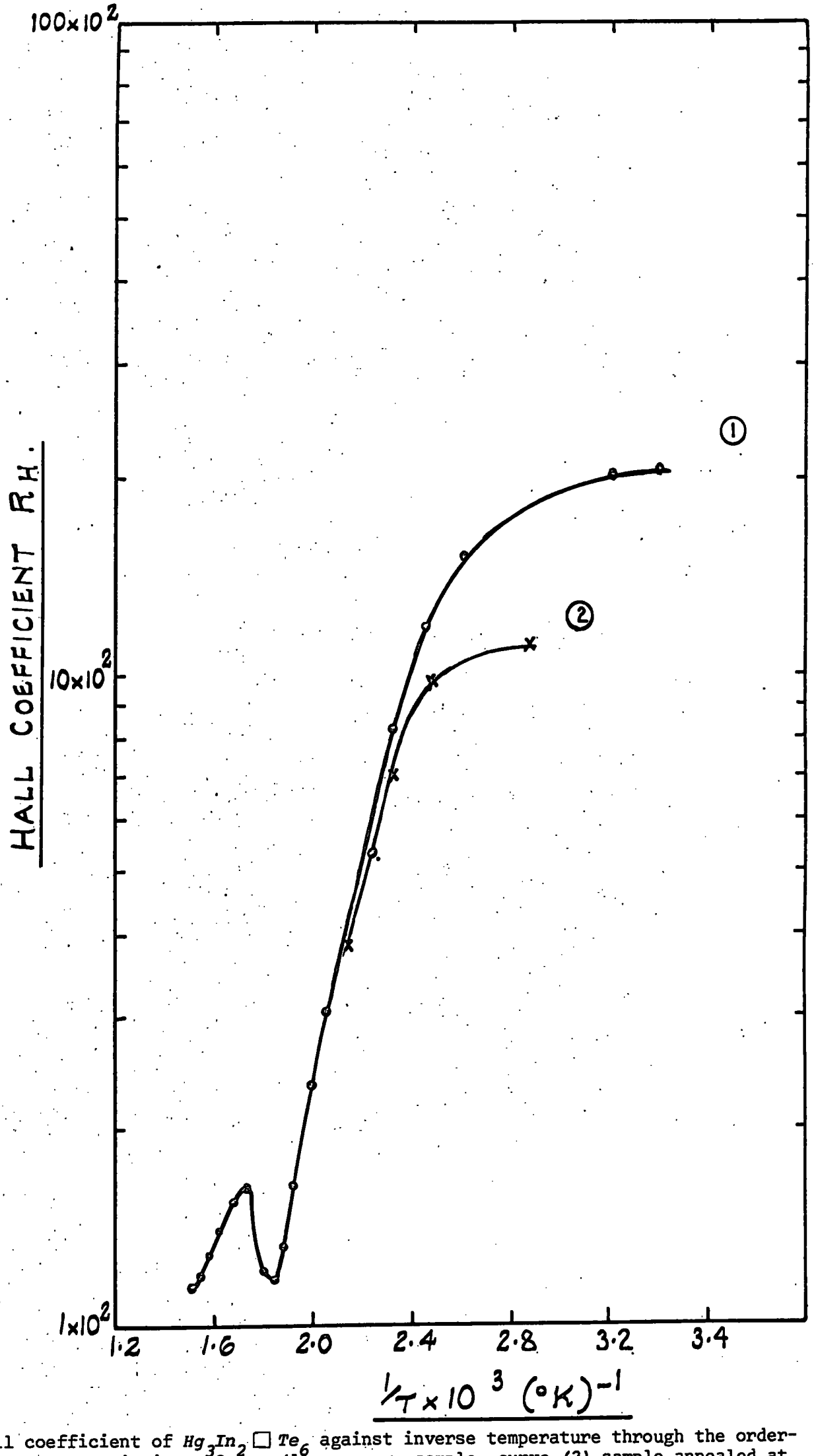

.27) Hall coefficient of $Hg_3In_2 \square Te_6$ against inverse temperature through the order-disorder transistion. Curve *(1)* as grown sample, curve *(2)* sample annealed at *200°C* for 40 hours.

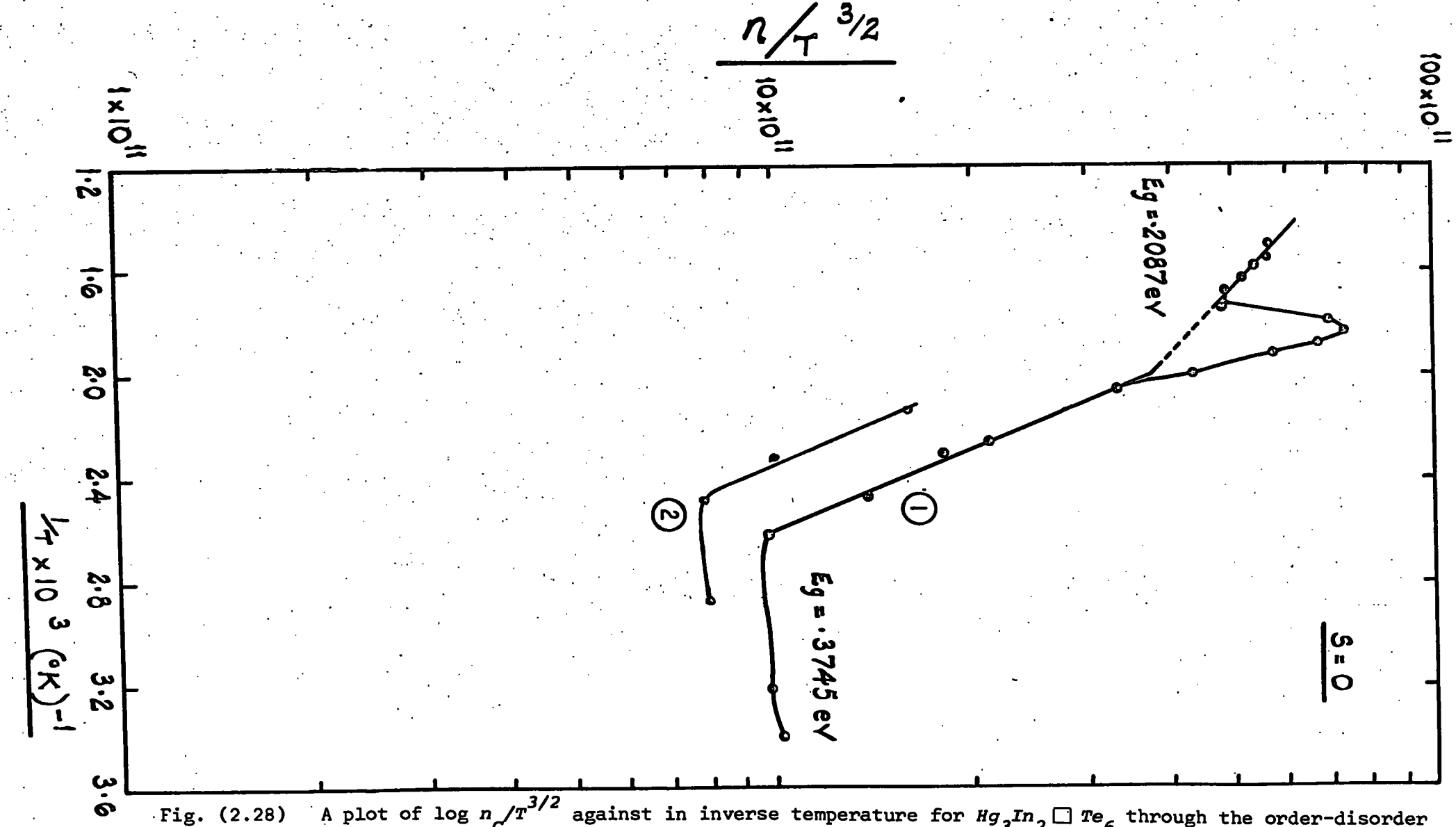

Fig. (2.28) A plot of log $n_c/T^{3/2}$ against in inverse temperature for $Hg_3In_2 \square Te_6$ through the order-disorder transformation. Curve *(1)* - as grown sample; curve *(2)*-sample annealed at 200^oC for 40 hours.

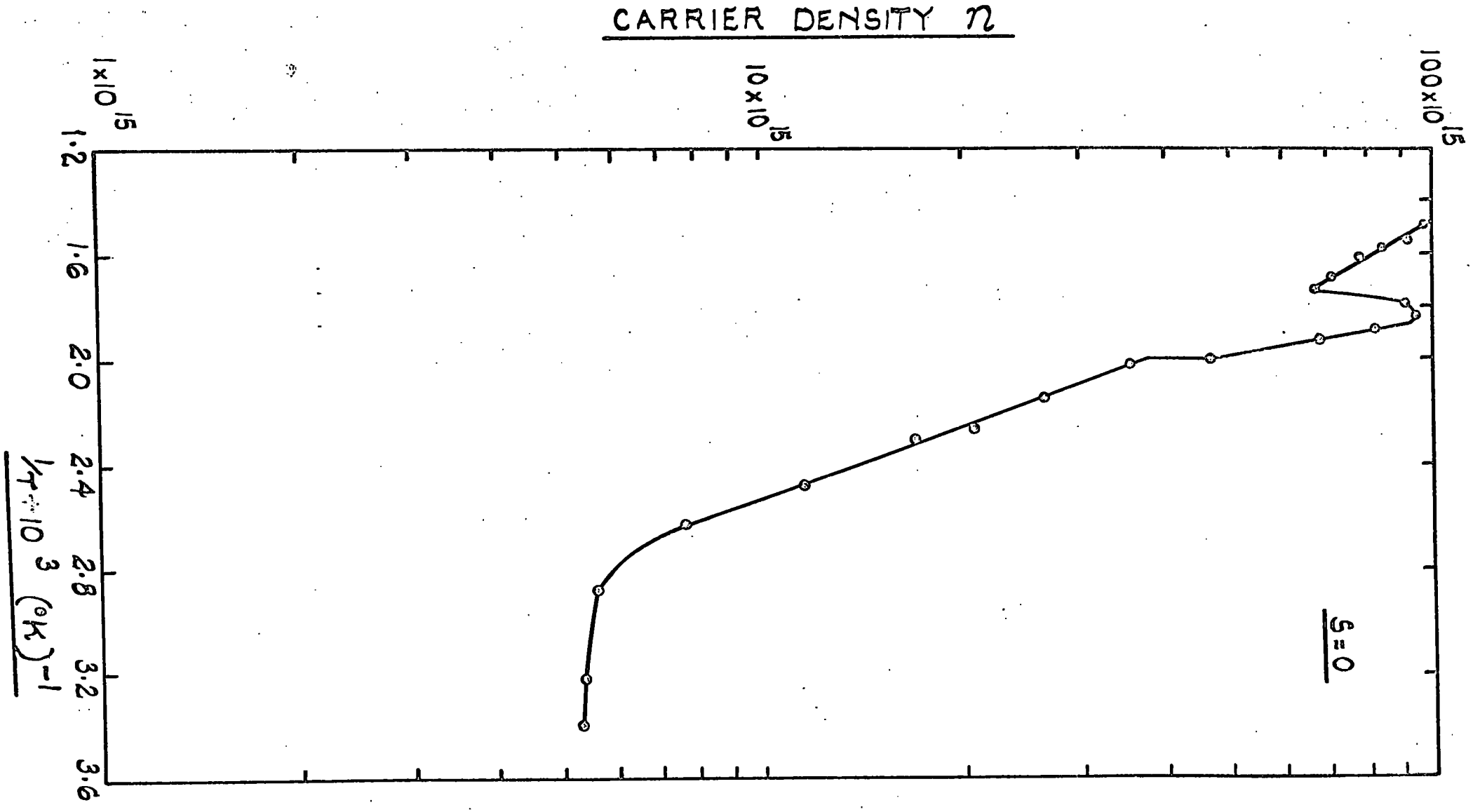

Fig. (2.29) Plot of carrier density against inverse temperature through the order-disorder transistion in $Hg_3In_2\square Te_6$.

CHAPTER 3

THE PROPAGATION OF ULTRASONIC WAVES IN SOLIDS

3.1 INTRODUCTION

A study of the propagation of ultrasonic stress waves in solids yields information about the velocities and the attenuation or energy loss in these waves. In the simplest case, two types of stress wave can be propagated *(i)* a pure longitudinal or a pure compressional plane wave where the particle motion is in the direction of propagation and *(ii)* a pure transverse or pure shear plane wave where the particle motion is transverse to the direction of propagation through the elastic solid. In general, however, for both a crystalline and an isotropic solid the waves are neither pure longitudinal nor pure transverse: the particle displacement has components both along and transverse to the direction of propagation. When the solid is finite in extent and hence bounded by surfaces, surface waves may be propagated. Measurement of the wave velocities and the density of the solid enables the elastic constants of the material to be determined which are related to the interatomic binding forces.

3.2 STRESS, STRAIN AND DISPLACEMENT RELATIONSHIPS

To enable the equation of motion of an ultrasonic stress wave to be related to the crystal symmetry, an outline of the basic theory behind the stress-strain relationship is now given.

A body, in which one part of the body exerts a force on another part is said to be in a state of stress. A volume element situated within the stressed body may have two types of force acting on it; body forces such as gravity, and forces exerted on the surface of the element by the material surrounding it. These latter forces are

proportional to the surface area of the element and the force per unit area is the definition of stress. The stress, or force per unit area acting across a surface element in a stressed body is related to the orientation of the element by

$$P_i = \sigma_{ij} l_j \tag{3.1}$$

where l_j are the components of a unit vector normal to the surface of the element. Hence the stress tensor σ_{ij} where $i,j = 1, 2, 3$ represents the components of a force per unit area acting on the element of area. The subscript i denotes the direction of the normal to the plane on which the stress component acts and the subscript j denotes the direction of the stress component. Since it is usual to assume that the stress throughout the body is homogeneous and that body torques are absent, these conditions allow the tensor to be symmetrical, so that

$$\sigma_{ij} = \sigma_{ji} \tag{3.2}$$

and it makes no difference if the subscripts are interchanged.

The strain tensor is defined in terms of variation in displacement S_i with position X_i in a body. This gives nine components

$$S_{i,j} = \frac{\partial S_i}{\partial X_i} \qquad (i,j = 1, 2, 3) \tag{3.3}$$

the comma notation for differentiation is used. These have the following meanings: $S_{1,1}$, $S_{2,2}$, $S_{3,3}$ are extensions per unit length parallel to the axis OX_1, OX_2, and OX_3 respectively, $S_{1,2}$ is the rotation about OX_3 towards OX_1 of a line element parallel to OX_2, $S_{2,1}$ is the rotation about OX_3 towards OX_2 of a line element parallel to OX_1, and similary for the other $S_{i,j}$. If the displacement is due to rotation without strain, the corresponding $S_{i,j}$ are antisymetrical

$$S_{i,j} = -S_{j,i} \quad \text{if} \quad i \neq j \tag{3.4}$$

Then since a second rank tensor can be expressed as the sum of a symmetrical and an antisymmetrical tensor,

$$S_{i,j} = \varepsilon_{ij} + \omega_{ij} \tag{3.5}$$

where

$$\varepsilon_{ij} = \tfrac{1}{2}(S_{i,j} + S_{j,i}) = \varepsilon_{ji} \tag{3.6}$$

is the symmetrical component and

$$\omega_{ij} = \tfrac{1}{2}(S_{i,j} - S_{j,i}) = -\omega_{ji} \tag{3.7}$$

is the antisymmetrical component. The symmetrical part of $S_{i,j}$ is defined as the strain tensor ε_{ij}. Then

$$\varepsilon_{ij} = \begin{vmatrix} S_{1,1} & \tfrac{1}{2}(S_{1,2} + S_{2,1}) & \tfrac{1}{2}(S_{1,3} + S_{3,1}) \\ \tfrac{1}{2}(S_{1,2} + S_{2,1}) & S_{2,2} & \tfrac{1}{2}(S_{2,3} + S_{3,2}) \\ \tfrac{1}{2}(S_{1,3} + S_{3,1}) & \tfrac{1}{2}(S_{2,3} + S_{3,2}) & S_{3,3} \end{vmatrix} \tag{3.8}$$

The diagonal components are the tensile strains and the other components measure the shear strains, where ε_{ij} when $i \neq j$ is twice the change in angle between two line elements parallel to the appropriate axis OX_i and OX_j. A more complete approach would have revealed second order terms in the strain tensor, which are neglected (see Truell, Elbanm and Chick 1969).

Provided the material is only strained within the elastic limit, Hookes law holds and the relationship between stress and strain is

$$\sigma_{ik} = C_{ikjl}\varepsilon_{jl} \qquad (i, k = 1, 2, 3) \tag{3.9}$$

which defines the elastic stiffness constant tensor of the fourth rank C_{ikjl}. This expression defines nine equations each with nine coefficients, therefore, there are *eighty one* coefficients in the most general form. The symmetry in the stress-strain tensors due to the absence of body torques requires the same symmetry in the elastic constant tensor,

$$C_{ikjl} = C_{kijl} = C_{iklj} \tag{3.10}$$

which immediately reduces the coefficients to *thirty six*. Finally, on straining an elastic medium there exists an elastic potential which amounts to having the strain energy

$$E = \tfrac{1}{2} C_{ikjl}\, \varepsilon_{ik}\, \varepsilon_{jl} \tag{3.11}$$

be a function of state and independant of the path by which the state is reached; this imposes the further symmetry relation

$$C_{ikjl} = C_{jlik} \tag{3.12}$$

which reduces the number of elastic constants from *thirty six* to *twenty one*. Therefore, the general linear stress-strain relationship in an elastic medium depends on *twenty one* coefficients.

The symmetry of C_{ikjl} in the first and last pair of indices allows the notation to be simplified by use of the matrix notation in which each pair of indices takes on one value as follows:

tensor notation	11	22	33	23 32	13 31	12 21
matrix notation	1	2	3	4	5	6

For example C_{1123} can be written as C_{14} and C_{2312} as C_{46}. In this notation Hooke's law becomes

$$\sigma_i = C_{ij}\varepsilon_j \quad (i,j = 1, 2, 3) \tag{3.13}$$

This law using tensor notation (equation 3.9) can also be written in the reciprocal form in which

$$\varepsilon_{ik} = S_{ikjl}\,\sigma_{jl} \tag{3.14}$$

This expresses the strain as a function of stress. The S_{ikjl} are called the elastic compliance moduli and relate directly to the elasticity of the material, whereas the elastic moduli C_{ikjl} relate to the stiffness. The symmetry imposed on the elastic stiffness moduli applies equally to the elastic compliance moduli for the same reasons; consequently, S_{ijkl} and C_{ijkl} are related by the expression in the matrix notation

$$S_{ij} = (-1)^{i+j}\,\Delta^C_{ij}/_{\Delta^C} \tag{3.15}$$

where Δ^C is the determinant of the C_{ij} terms and Δ^C_{ij} is the minor of the element C_{ij}.

The symmetry of the crystal systems allows a further reduction in the number of independant elastic constants; only crystals in the triclinic class retain the full number. Analytical methods are used for the trigonal and hexagonal classes, but a direct inspection method (Fumi 1952; Fieschi and Fumi 1953) yields the number of constants required to describe the elastic behaviour of each of the other crystal classes. The matrix for the cubic class is

$$\begin{vmatrix} C_{11} & C_{12} & C_{12} & 0 & 0 & 0 \\ C_{12} & C_{11} & C_{12} & 0 & 0 & 0 \\ C_{12} & C_{12} & C_{11} & 0 & 0 & 0 \\ 0 & 0 & 0 & C_{44} & 0 & 0 \\ 0 & 0 & 0 & 0 & C_{44} & 0 \\ 0 & 0 & 0 & 0 & 0 & C_{44} \end{vmatrix} \qquad (3.16)$$

where only three constants C_{11}, C_{12} and C_{44} describe the elastic properties, since the symmetry restrictions allow

$$C_{11} = C_{22} = C_{33},\ C_{12} = C_{13} = C_{23} \text{ and } C_{44} = C_{55} = C_{66}$$

all other coefficients are zero.

3.3 THE PHYSICAL SIGNIFICANCE OF THE ELASTIC STIFFNESS CONSTANTS C_{ij} OF A CUBIC CRYSTAL

The physical significance of the elastic constants is not immediately obvious. In general, the quantity C_{ij} expresses the stress strain ratio σ_i/ε_j under the condition that all strains other than ε_j are zero. The meaning of this statement can be appreciated by applying it to the cubic crystal as follows.

If a normal stress σ_n (Figure 3.1) is applied to two *(110)* faces of a cubic crystal and stresses are applied to the other faces to ensure that only the normal strain ε_n parallel to the $|110|$ *direction* occurs, then

$$\frac{\sigma_n}{\varepsilon_n} = C_n \qquad (3.17)$$

and

$$C_n = \frac{(C_{11} + C_{12} + 2C_{44})}{2} \qquad (3.18)$$

If the sample is under a shear strain such that the angle between the $|001|$ and the $|110|$ directions decreases, then this may be achieved by a shear stress applied to the *(110)* faces in the $|001|$ direction (Figure 3.1); this being the only stress necessary. Then for this example the ratio

$$\frac{\sigma_n}{\varepsilon_n} = C_{44} \tag{3.19}$$

In a similar way, a shear stiffness may be defined if the shear stresses are applied in the $|\bar{1}10|$ direction on the *(110)* faces to produce a shear strain measured by the decrease in angle between the $|110|$ and the $|\bar{1}10|$ direction. The stress-strain ratio is in this case

$$C' = \frac{(C_{11} - C_{12})}{2} \tag{3.20}$$

Thus, the three independent elastic stiffness constants of a cubic crystal can be expressed as two shear C_{44} and C' and one normal stiffness constant C_n.

3.4 VOLUME COMPRESSIBILITY AND BULK MODULUS

The proportional decrease in volume of a crystal when subjected to unit hydrostatic pressure is defined as being the volume compressibility K and its inverse is called the bulk modulus B. The stress exerted in terms of the pressure is

$$\sigma_{kl} = -p\delta_{kl} \tag{3.21}$$

where

$$\delta_{kl} = \begin{cases} 0 & \text{if } k \neq l \\ 1 & \text{if } k = l \end{cases} \tag{3.22}$$

is the Kronecker delta. This when used with Hooke's Law (equation 3.13) gives the dilation

$$\varepsilon_{ij} = -pS_{ijkl}\delta_{kl} = -pS_{iikk} \tag{3.23}$$

The change in volume of a unit cube (Figure 3.2) which has its edges parallel to the principal axes, three mutually perpendicular directions which remain orthogonal during deformation, is given by

$$\Delta = \varepsilon_1 + \varepsilon_2 + \varepsilon_3 = \varepsilon_{ij} \tag{3.24}$$

and so the volume compressibility $(K = -\Delta/P)$ is S_{iikk}. In the matrix notation this becomes

$$K = S_{11} + S_{22} + S_{33} + 2(S_{12} + S_{23} + S_{31}) \tag{3.25}$$

which is the sum of the nine coefficients in the upper left hand corner of the compliance matrix. This reduces for cubic crystals to

$$K = 3(S_{11} + 2S_{12}) \tag{3.26}$$

and its inverse is the bulk modulus or volume stiffness which is given by

$$B = \frac{C_{11} + 2C_{12}}{3} \tag{3.27}$$

Both these expressions also hold for isotropic materials.

3.5 EQUATIONS OF MOTION AND SOLUTIONS

The equation of motion for an elastic medium is obtained by considering the forces acting on an element of volume in the medium.

In particular, if the difference between pairs of forces acting on opposite faces of a small rectangular parallelopiped is considered, one arrives at the components of the resultant force (neglecting body forces) acting on the volume (for details see Kolsky 1953). Then by equating the force components $\sigma_{ij,j}$ to the acceleration components $\ddot{S}_i$ for a medium of density ρ, the following equation of motion is obtained:

$$\sigma_{ij,j} = \rho\ddot{S}_i \quad (i = 1, 2, 3) \tag{3.28}$$

Substituting the stress-strain relationship (equation 3.9) in this expression gives

$$C_{ijkl}\varepsilon_{kl,j} = \rho\ddot{S}_i \tag{3.29}$$

where

$$\varepsilon_{kl,j} = \tfrac{1}{2}(S_{l,kj} + S_{k,lj}) \tag{3.30}$$

then

$$C_{ijkl}(S_{l,kj} + S_{k,lj}) = 2\rho\ddot{S}_i \tag{3.31}$$

and since C_{lkjl} is symmetrical, this reduces to

$$C_{ijkl}S_{l,kj} = \rho\ddot{S}_i \quad (i = 1, 2, 3) \tag{3.32}$$

an equation of motion involving the elastic constants.

Ultrasonic waves can be propagated in any direction in a crystalline medium regardless of whether or not it is isotropic. In each direction three independent waves can be transmitted, each with a distinct velocity and with particle displacements which are mutually orthogonal. In general, none of these displacements coincide with either the wavefront normal or with a direction at right angles to it, hence the wave cannot be classified as either pure longitudinal or pure transverse. However, there are certain specific directions in the crystal in which the wavefront normal does coincide with the particle displacement vector and a pure longitudinal (or compressional) wave can be propagated. The other two displacement vectors of the orthogonal set will then lie in the plane of the wavefront in which case pure transverse (or shear) waves will be propagated.

The equation for the components of any one of the plane waves is,

$$S_l = So_l \, e^{i(\omega t - \underline{k}.\underline{r})} \quad (l = 1, 2, 3) \tag{3.33}$$

which travels in the direction given by the propagation vector $\underline{k}(k_1, k_2, k_3)$ drawn normal to the wavefront. A unit vector $\underline{n}(n_1, n_2, n_3)$ can also be defined in this direction giving the relationship

$$\underline{k} = (\frac{\omega}{v})\underline{n} = (\frac{2\pi}{\lambda})\underline{n} \quad , \tag{3.34}$$

where ω is the angular frequency, v is the phase velocity and λ is the wavelength. $\underline{S}(S_1, S_2, S_3)$ is the particle displacement vector which in general is not parallel to the wave vector $\underline{k}$. Then a general solution of the equation of motion (3.30) was obtained by Christoffel on substituting

$$S_{l,kj} = -n_k n_j So_l \, (\frac{\omega^2}{v^2}) e^{i(\omega t - \underline{k}.\underline{r})} \tag{3.35}$$

and

$$\ddot{S}_i = -So_i \omega^2 e^{i(\omega t - \underline{k}.\underline{r})} \tag{3.36}$$

in the equation (3.30) to give

$$C_{ijkl} So_l n_k n_l = \rho v^2 So_i \quad (i = 1, 2, 3) \tag{3.37}$$

Perhaps this is more convenient when it is written as three equations in the matrix notation

$$\begin{aligned} (L_{11} - \rho v^2)So_1 &+ L_{12}So_2 &+ L_{13}So_3 &= 0 \\ L_{12}So_1 &+ (L_{22} - \rho v^2)So_2 &+ L_{23}So_3 &= 0 \\ L_{13}So_2 &+ L_{23}So_2 &+ (L_{33} - \rho v^2)So_3 &= 0 \end{aligned} \tag{3.38}$$

where L_{11} to L_{33} are a series of moduli which are functions of the elastic stiffnesses C_{ij} and the direction cosines n_1, n_2 and n_3. Then in general for any crystal symmetry,

$$\begin{aligned} L_{11} &= n_1^2 C_{11} + n_2^2 C_{66} + n_3^2 C_{55} + 2n_2 n_3 C_{56} \\ &\quad + 2n_3 n_1 C_{15} + 2n_1 n_2 C_{16} \\ L_{12} &= n_1^2 C_{16} + n_2^2 C_{26} + n_3^2 C_{45} + n_2 n_3 (C_{46} + C_{25}) \\ &\quad + n_3 n_1 (C_{14} + C_{56}) + n_1 n_2 (C_{12} + C_{66}) \\ L_{13} &= n_1^2 C_{15} + n_2^2 C_{46} + n_3^2 C_{35} + n_2 n_3 (C_{45} + C_{36}) \\ &\quad + n_3 n_1 (C_{13} + C_{55}) + n_1 n_2 (C_{14} + C_{56}) \\ L_{22} &= n_1^2 C_{66} + n_2^2 C_{22} + n_3^2 C_{44} + 2n_2 n_3 C_{24} \\ &\quad + 2n_3 n_1 C_{46} + 2n_1 n_2 C_{26} \end{aligned} \tag{3.39}$$

$$L_{23} = n_1^2 C_{56} + n_2^2 C_{44} + n_3^2 C_{34} + n_2 n_3 (C_{44} + C_{23})$$
$$+ n_3 n_1 (C_{36} + C_{45}) + n_1 n_2 (C_{25} + C_{46})$$

$$L_{33} = n_1^2 C_{55} + n_2^2 C_{44} + n_3^2 C_{33} + 2 n_2 n_3 C_{34}$$
$$+ 2 n_3 n_1 C_{35} + 2 n_1 n_2 C_{45}$$

The compatibility condition for the solution of equations (3.36) requires that the determinant of the coefficients of So_1, So_2 and So_3 be zero; this is written

$$\begin{vmatrix} L_{11} - \rho v^2 & L_{12} & L_{13} \\ L_{12} & L_{22} - \rho v^2 & L_{23} \\ L_{13} & L_{23} & L_{33} - \rho v^2 \end{vmatrix} = 0 \qquad (3.40)$$

This is a cubic equation in ρv^2, the roots of which give the velocities of the three independent waves. The values of So_1, So_2 and So_3 the components of the displacement vector are such that the wave is neither pure longitudinal or pure transverse.

3.6 PROPAGATION DIRECTIONS AND VELOCITIES IN CUBIC CRYSTALS

The use of ultrasound waves for measurements in single crystals is confined wherever possible to pure compressional or pure transverse modes propagated in principle directions through the crystal; such waves will be discussed with reference to cubic crystals only. Thus the symmetry conditions reduce the elastic constants to C_{11}, C_{12} and C_{44}, which reduces the moduli of the determinant (3.37) to

$$L_{11} = n_1^2 C_{11} + (n_2^2 + n_3^2) C_{44} \tag{3.41}$$

$$L_{12} = n_1 n_2 (C_{12} + C_{44})$$

$$L_{13} = n_3 n_1 (C_{12} + C_{44})$$

$$L_{22} = (n_1^2 + n_3^2) C_{44} + n_2^2 C_{11}$$

$$L_{23} = n_2 n_3 (C_{12} + C_{44})$$

$$L_{33} = (n_1^2 + n_2^2) C_{44} + n_3^2 C_{11}$$

The conditions, as previously stated, that a pure longitudinal wave be propagated is that the wavefront normal coincides with the displacement vector $\underline{S}$;

$$\underline{S} \times \underline{n} = 0 \quad \textit{hence} \quad \underline{S} \| \underline{n} \tag{3.42}$$

To propagate a pure transverse wave this vector must be perpendicular to the wavefront normal, namely

$$\underline{S} \cdot \underline{n} = So_1 n_1 + So_2 n_2 + So_3 n_3 = 0 \tag{3.43}$$

There are three simple orientations in a cubic crystal in which it is possible to meet these requirements.

$$|100| \textit{ where } n_1 = 1 \; ; \; n_2 = n_3 = 0, \tag{3.44}$$

$$|110| \textit{ where } n_1 = \frac{1}{\sqrt{2}} = n_2 \; ; \; n_3 = 0$$

and $|111|$ *where* $n_1 = n_2 = n_3 = \frac{1}{\sqrt{3}}$

The orientation of most interest is the $|110|$ direction since the velocity equations resulting from the solution of equation (3.38) are

$$\rho v_1^2 = \tfrac{1}{2}(C_{11} + C_{12} + 2C_{44}) \tag{3.45}$$

since $\underline{S}$ is along the $|110|$ direction; this is a longitudinal wave. Also

$$\rho v_s^2 = C_{44} \tag{3.46}$$

when $\underline{S}$ is along the $|001|$ direction and

$$\rho v_s^2 = \frac{C_{11} - C_{12}}{2} \tag{3.47}$$

when $\underline{S}$ is along the $|1\bar{1}0|$ direction; these waves are transverse. Therefore measurement of the velocity of one longitudinal and two transverse waves polarized in the appropriate directions enables all three elastic constants to be determined from these equations. Figure (3.3) illustrates the situation.

3.7 ATTENUATION

The attenuation of a plane high frequency ultrasonic wave propagated through a sample can be determined from the envelope of the wave (Figure 3.4). The amplitude at any position x into the sample is given by

$$\sigma(x) = \sigma_o e^{-\alpha x} \tag{3.48}$$

where σ_o is the initial amplitude and α is the attenuation coefficient. This expression can be written as

$$\log_e \sigma(x) = \log_e \sigma_o - \alpha x \tag{3.49}$$

Then for two different points x_1 and x_2 where $x_1 < x_2$ the difference of the expressions at the two points is

$$\alpha = \left[\frac{1}{x_2 - x_1} \right] \log_e \left[\frac{\sigma(x_1)}{\sigma(x_2)} \right] \tag{3.50}$$

and since any ratio of two amplitudes such as $\sigma(x_1)$ and $\sigma(x_2)$ must, in order to be expressed in decibels or nepers be written as

$$20 \log_{10} \left[\frac{\sigma(x_1)}{\sigma(x_2)} \right] \quad dB \tag{3.51}$$

or

$$\log_e \left[\frac{\sigma(x_1)}{\sigma(x_2)} \right] \quad nepers \tag{3.52}$$

then

$$\alpha = \left[\frac{1}{x_2 - x_1} \right] 20 \log_{10} \left[\frac{\sigma(x_1)}{\sigma(x_2)} \right] \quad dB/cm \tag{3.53}$$

or

$$\alpha = \frac{1}{x_2 - x_1} \log_e \left[\frac{\sigma(x_1)}{\sigma(x_2)} \right] \quad nepers/cm \tag{3.54}$$

and conversion between the two units is affected by

$$\alpha \ (dB/cm) = 8.686\alpha \ (nepers/cm) \tag{3.55}$$

Another expression for the energy loss is that of the logarithmic decrement δ which is defined for an underdamped harmonically oscillating system in free decay as

$$\delta = \frac{W}{2E} \ , \tag{3.56}$$

where W is the energy loss per cycle in the specimen, and E is the total vibrational energy stored in the specimen per cycle. This

definition is equivalent to the relationship

$$\delta = \log_e \left(\frac{\sigma_n}{\sigma_{n+1}} \right) \tag{3.57}$$

where σ_n and σ_{n+1} are the amplitudes of two consequtive cycles. It follows from equation (3.53) that

$$\delta \text{ (nepers)} = \alpha \text{ (nepers/cm)} \; \lambda \text{ (cm)} \tag{3.58}$$

or

$$\delta = \frac{\alpha \text{(nepers/cm)}}{f \text{(1/sec)}} \; v \text{(cm/sec)} \tag{3.59}$$

Finally

$$\alpha \text{(dB/}\mu\text{sec)} = 8.68 \times 10^{-6} v \text{ (cm/sec)} \; \alpha \text{ (nepers/cm)} \tag{3.60}$$

or

$$\alpha \text{(dB/}\mu\text{sec)} = 8.68 \times 10^{-6} f \text{ (1/sec)} \; \delta \text{ (nepers)}. \tag{3.61}$$

Also

$$\alpha \text{(dB/}\mu\text{sec)} = \alpha \text{(dB/cm)} \times 10^{-6} v \text{ (cm/sec)} \tag{3.62}$$

which is the most important relationship since the ultrasonic comparitor measures attenuation in *dB/μsec*.

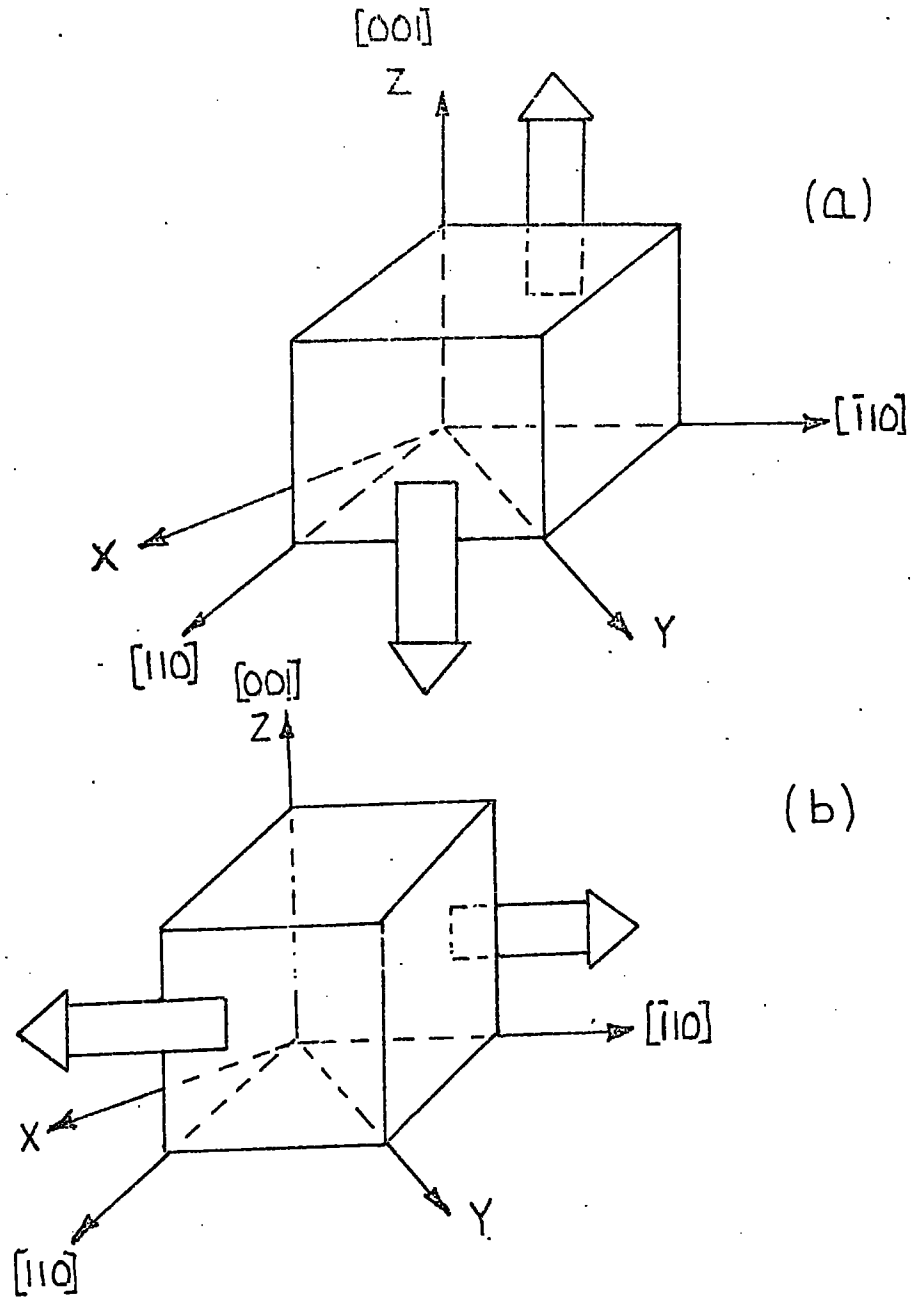

Fig. (3.1) Illustrates the physical interpretation of the elastic shear moduli C_{44} *(a)* and $(C_{11} - C_{12})/2$ *(b)* of a cubic crystal.

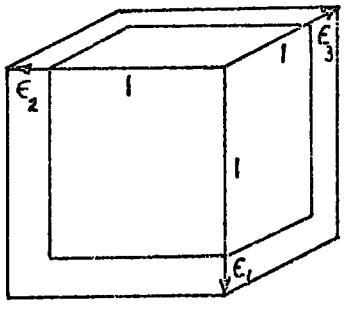

Fig. (3.2) The strain of a unit cube cut with its edges parallel to the three principle axes of strain.

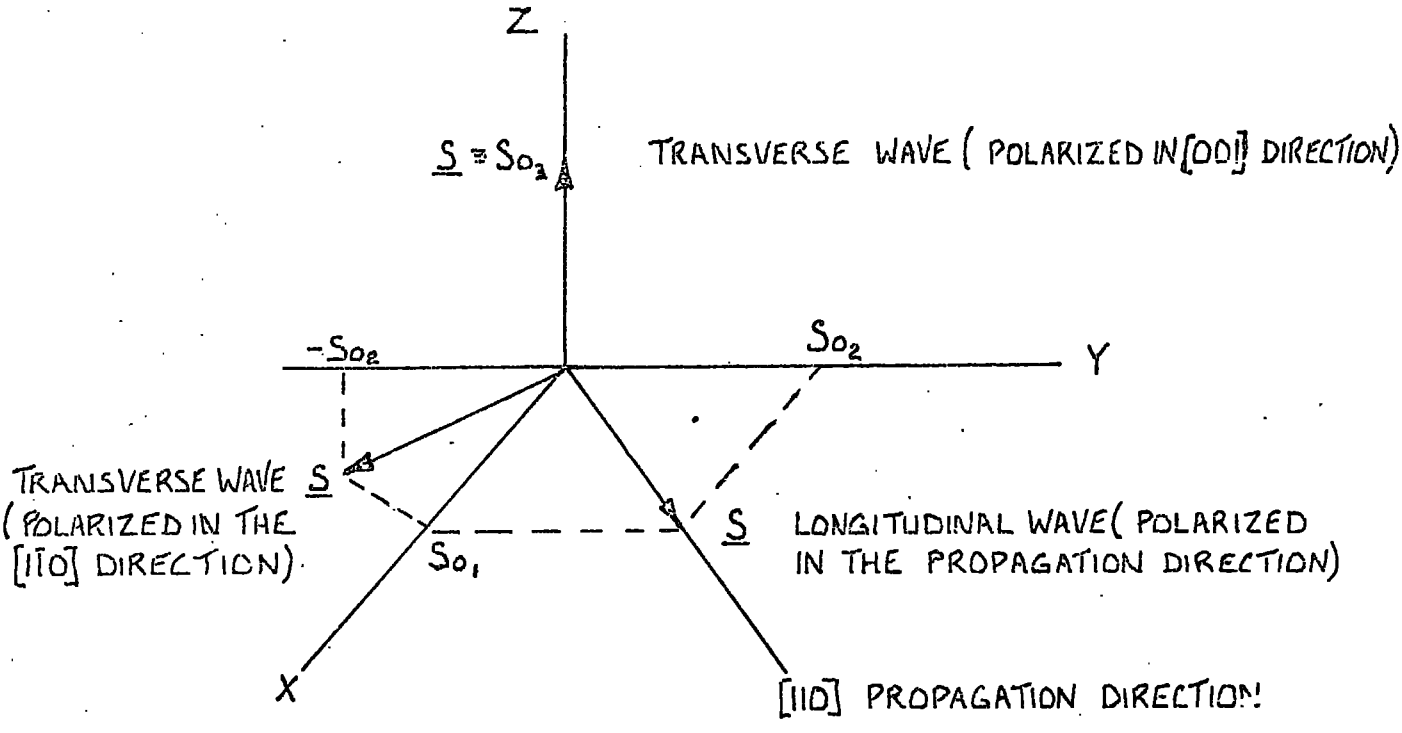

Fig. (3.3) Illustrates the propagation direction of the sound wave and the polarization required to obtain all the elastic constants of a cubic crystal.

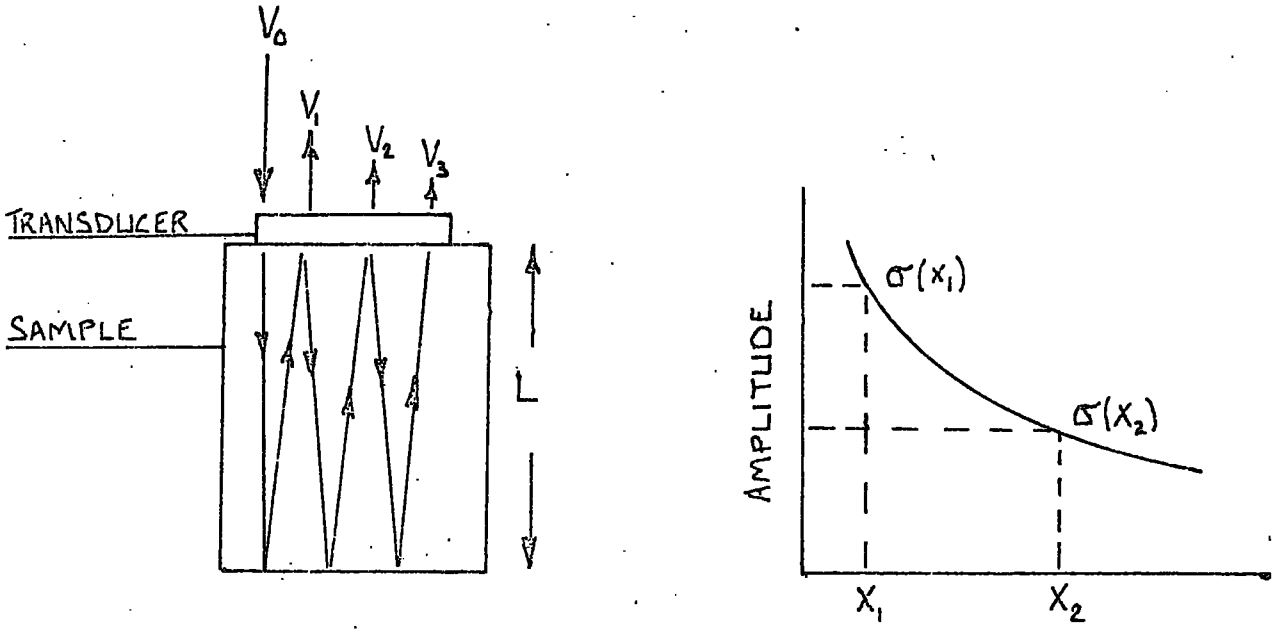

Fig. (3.4) Physical basis of attenuation measurements.

C H A P T E R 4

VELOCITY AND ATTENUATION MEASUREMENTS

4.1 INTRODUCTION

The pulse echo method of measuring the velocity of ultrasonic waves in solids has been in use for some time but measurements of the attenuation of these waves have only been made relatively recently. McSkimin (1964) has given a comprehensive review of the various ultrasonic techniques for measuring the mechanical properties of solids and liquids.

The purpose of this chapter is to discuss the single-ended pulse echo technique of generating and measuring the velocity and attenuation of an ultrasonic wave propagated through a solid. The attendant difficulties in making the measurements over a temperature range from $77^{o}K$ to room temperature are examined and an estimate is made of the significance of the associated errors on the experimental accuracy.

4.2 DESCRIPTION OF THE SINGLE ENDED PULSE ECHO METHOD OF MEASUREMENT

The velocity and attenuation of ultrasonic waves in single crystals of the mercury-indium and mercury-gallium tellurides have been measured by the single-ended pulse echo technique, a basic outline of which is shown in the block diagram Figure (4.1). A piezoelectric quartz transducer bonded to the sample is hit with a pulsed *R.F.* wave which is tuned to the fundamental or one of the odd harmonics of the transducer. The resulting ultrasonic wave is coupled into the specimen and a series of reverberations is set up in the material during the pause between the input pulses. A small fraction of each echo generates an electrical signal in the originating transducer; these signals are amplified in a high gain receiver, after which they are detected and filtered. The

resulting envelope of the pulse train is displayed on an oscilloscope (Figure 4.2).

The equipment used in these experiments was a Matec Inc., Attenuation Comparitor, Model 9000 using a Model 960 *R.F.* plug in unit. This apparatus incorporates within one frame all the units shown on the block diagram (Figure 4.1). The *R.F.* pulsed wave is generated within the plug-in unit and its frequency can be varied continuously between *10 MHz* and *310 MHz*. The amplitude of this wave is also continuously variable to a maximum of *3kV* peak to peak at *10 MHz*. Above this frequency there is a slight reduction in the maximum amplitude of the pulse. The pulse repetition rate, controlled by a synchronous switch can be varied between *10* and *1000* pulses per second and the pulse width can be adjusted between *0.5* and *5μsec*.

The receiver, which covers the frequency range *10 MHz* to *310 MHz* has a band width of *4 MHz* and a maximum gain of *80 dB*, which is required to compensate for the high insertion loss, typically *30* to *60 dB* associated with quartz transducers and the high attenuation experienced in some materials. A typical echo train is shown in Figure (4.2); the first peak is due to leakage of *R.F.* power through the sample holder and the second and subsequent peaks are echos propagated through the specimen length twice, four times, six times etc. Hence the time delay between successive echos is the time required for a round trip through the specimen. This delay time is measured by a calibrated delay generator to an accuracy of *1%* when the following procedure is adopted.

The leading edge of the exponential waveform is matched to the leading edge of successive echos, the time delay position of each echo being noted. To ensure uniformity, the gain of the receiver must be adjusted so that each echo has the same amplitude when matched to the leading edge of the exponential trace. Also, the pulse amplitude of the *R.F* generator is held constant since any change will alter the

rise time of the echos and produce erroneous measurements. A high rise time in the envelope of the echos increases the sensitivity of the measurements. This can be obtained by making the initial *R.F.* pulse have a large amplitude, a condition which is also dependent on the attenuation of the material under test, hence it is not always convenient.

Relative attenuation measurements are obtained by matching an exponential trace, produced by a calibrated comparator, to peaks in the echo train, the trailing edge of which is chopped to ensure that it does not run on into the next pulse. Absolute values of attenuation are seldom required and in any case they are difficult to obtain, because of the inherent problems associated with attenuation loss in the transducer and its bond with the sample. However, the exponential trace does allow sensitive measurements of relative attenuation as a function of some external parameter, which in this case is temperature.

4.3 PIEZOELECTRIC TRANSDUCERS

Sound waves are generated or received at the transducer by utilizing the piezoelectric effect first discovered by the Curie brothers. Certain single crystals exhibit this phenomenon; when the crystal is deformed by the application of an external stress, electric charge appears on the appropriate crystal surfaces and the polarity of this charge reverses, when the direction of the strain is reversed. Conversely, when a piezoelectric single crystal is placed in an electric field, the crystal exhibits strain, that is the dimensions of the crystal change and when the direction of the applied electric field is reversed, the direction (sign) of the resulting strain is reversed. This is called the converse or inverse piezoelectric effect.

Of the thirty two classes of crystal symmetry, twenty one have no centre of symmetry and of these twenty can exhibit piezoelectricity. This effect has been demonstrated qualitatively in numerous crystal

materials, but of these only a few are used in practical transducer design. The most common transducers are cut from quartz (SiO_2) which belongs to the trigonal ($R\bar{3}m$) crystal class. A quartz crystal is illustrated in Figure (4.3); the main body forms a hexagonal prism with rhombohedral ends. The *Z-axis* or optic axis is an axis of threefold rotational symmetry and is non polar. A crystal section perpendicular to the *Z-axis* has a hexagonal shape, therefore, three lines joining opposite hexagon apices can be drawn, one of these is chosen as the *X-axis* and the *+X, +Y, +Z* right handed axial is completed by defining the *+Y - axis* as the normal to the *+X, +Z* plane. These axes are the polar axis and transducers cut with their faces perpendicular to them display the piezoelectric effect. Sections cut normal to the *X-axis* are used to generate longitudinal waves and those cut normal to the *Y-axis* generate transverse waves (Figure 4.3). These sections, called *X* and *Y* cut types respectively, are cut in the form of a disc, the *Y* cut type having a flat on one side to indicate the direction in which the wave is polarized. The discs are completely coated with a thin gold film except for a central ring of quartz on one face (Figure 4.3); the inner and outer diameters of this ring are *4 mm* and *4.5 mm* respectively. Electrical contact is made to the inner disc and the outer ring is earthed to the sample holder to complete the circuit; the completely coated side is attached to the specimen.

In operation maximum acoustic energy is obtained by vibrating the transducer in its fundamental mechanical mode, but, if necessary, higher frequency waves can be generated by exciting in the odd harmonic modes. Consider an *X-cut* plate vibrating in the thickness direction, the natural frequency of the transducer occurs when there is maximum elongation of the faces in opposite directions, a situation described by a standing elastic wave with displacement antinodes on both faces. When excited in the first normal mode of vibration, there is only a single nodal plane

and the transducer thickness is equal to half a wavelength. Consequently, the extreme of this mode of operation is about *100 MHz;* beyond this frequency the discs become too thin and fragile to be of practical use. If the disc is excited at its n^{th} harmonic, its thickness is divided into *n* equal parts with compressions and expansions taking place in adjoining sections. When *n* is even, compressions occur in *n/2* of the sections and expansions take place in the remainder, thus there is no net strain in the quartz. However, when *n* is odd, *(n-1)/2* compressions neutralize the same number of expansions leaving either a compression or an expansion in the remaining section. The pulse ultrasonic equipment has been used to excite a transducer of fundamental frequency *10 MHz* at harmonic frequencies up to *290 MHz* but the conversion efficiencies are low at the high frequency end.

4.4 BONDING OF THE TRANSDUCER TO THE SAMPLE

Success in obtaining a good echo pattern using the pulse-echo ultrasonic technique depends critically on the quality of the bond between the transducer and the specimen. Consequently, the bonding material and the preparation of the bond must meet the following requirements.

(i) The seal should have uniform thickness and be thin compared with the ultrasound wavelength; otherwise after a round trip has been completed a fraction of the sound will be reflected back and forth within the bond causing the first and succeeding echos to be composed of several component waves with phase delays between them. If the bond had no thickness, there would be no phase shift.

(ii) All particles or air bubbles should be excluded from the bonding material.

(iii) The seal should retain a good match between transducer and specimen and have constant attenuation loss over the temperature range of the measurements. A good bond can be obtained with materials which remain viscous over the temperature range required ($77^{o}K$ to ambient); materials which conform to this requirement include 250,000 centistoke silicon fluid and nonaq stopcock grease; these made excellent bonds between *X-cut* transducers and the single crystal specimens over almost the complete temperature range, although they do deteriorate about room temperature. When used with *Y-cut* transducers a bond made with silicon fluid tends to break away at about $200^{o}K$; if nonaq stopcock grease is used, the bond breaks down at about $250^{o}K$. It was difficult to obtain a good bond using either of these materials on specimens which had been polished to a mirror finish (*0.5* micron diamond dust). To improve the cohesive qualities, each specimen was lightly etched with the cleaning etchant (section 2.4). An alternative method was to polish the specimen to a matt finish (*13* micron diamond dust), in some cases this proved more successful.

The bonds produced, by the following technique enabled a good echo pattern to be displayed, which was stable over a wide temperature range.

(i) The transducer and polished specimen faces were first cleaned with acetone and dried.

(ii) A small drop of bonding fluid was placed on both cleaned faces and the transducer was rung onto the specimen.

(iii) Finally, a *30 gm* weight chosen for convenience, was placed on the transducer in a vacuum chamber (10^{-6} *torr*) for approximately four hours. This removed any trapped air bubbles in the fluid and ensured a thin uniform seal.

4.5 ERRORS INVOLVED IN PULSE ECHO ULTRASONIC MEASUREMENTS

The measured attenuation of successive echos must be interpreted with caution as there are many possible causes of attenuation other than direct absorption by the medium itself, these include losses due to *(a)* scattering from inhomogenities *(b)* diffraction *(c)* nonparallelism and wedging effects and *(d)* dissipation of sound energy in the bond. These effects are now considered in turn.

(a) Scattering: Any sort of inhomogeneity in the sample under test will give rise to scattering which breaks up the intensity of the beam, altering the appearance of the echo pattern. This type of behaviour occurs in the megacycle range if the material contains foreign bodies; residual thermal stesses have the same effect. Also, extensive scattering can be caused in polycrystalline specimens, if the grain size is not small compared with the wavelength of the ultrasound; this was not applicable here. The appearance of the echo patterns indicated that these scattering effects were absent in the single crystals used; consequently the samples were of adequate quality for the ultrasonic measurements.

(b) Diffraction Effects: The transducer, when excited, produces a radiation pattern travelling through the specimen. In general, the beam is not collimated and the radiation will not be entirely confined to the cylindrical region below the transducer. Thus interference can take place in a small sample between waves reflected from the back of the specimen and waves reflected from the walls. This changes the exponential nature of the echo pattern modulating the envelope. Excitation of the transducer in the higher frequency harmonic modes will reduce the angle of the beam, eventually causing the envelope to become exponential. Samples of a size sufficient to avoid this effect at the frequency employed *10 MHz* were used.

Even when interference due to side wall reflections is absent, there remains the problem of the diffraction field of the source which includes divergence. This is identified by the location of a maximum in the echo pattern near the position a^2/λ where a is the transducer radius and λ is the wavelength of the ultrasonic wave. A rough criterion of the importance of diffraction effects on attenuation measurements can be obtained by applying a correction (Granato and Truell 1956) of *1 dB/distance of* a^2/λ. This has been verified in experiments on *HgTe* (Alper 1968). Although diffraction effects do play a role in attenuation in the low frequency range, they are not important in velocity measurements of the order of accuracy employed here.

(c) Non-Parallelism and Wedging Effects: The transducer used to produce and detect the ultrasound is a phase sensitive device and the measured response is an integrated value over the area of the transducer. Phase variations which occur over this area lead to interference and an accompanying error, especially in attenuation measurements. If the specimen faces are not perfectly parallel, an originally plane wave, when reflected back through a small angle, meets the transducer at an angle; consequently, the different surface area elements detect different phase of the wave (Figure 4.4). This causes the echo pattern envelope to deviate from the exponential and gives rise to a series of maxima. The wedging angle in the specimens used was measured as less than 4×10^{-4} *radians* with a dial micrometer which is capable of measuring to *0.0001 inch*. The magnitude of the error produced by this angle in the attenuation measurements can be estimated using an approximate correction formula (Truell and Oates 1963),

$$\alpha_{error} = \frac{8.68\,\pi^2 f^2 a^2 \theta^2 n}{vL} \quad dB/\mu sec \tag{4.1}$$

which is applicable for high frequency or high attenuation measurements; here f is the wave frequency, a is the transducer radius, θ is the angle deviation from parallel, n is the echo number, v is the velocity of the ultrasound and L is the sample length. For a $Hg_3In_2\square Te_6$ specimen at $77^{O}K$ the error produced in the attenuation of a longitudinal wave of the frequency used *(10 MHz)* is less than

$$\alpha_{error} = 0.0388\ dB/\mu sec \qquad (4.2)$$

where $L = 0.3988\ cm$, $a = 0.6\ cm$, $n = 8$ and $v = 0.2812 \times 10^{-6}\ cm/sec$, which is small compared to the measured attenuation. The exponential nature of the echo pattern indicates that this is a realistic value. At this frequency any change in the velocity produced by non-parallelism is negligible. The error does become significant at higher frequencies but it can be reduced by using a small diameter transducer and a long specimen. Unfortunately, small transducers produce a large diffraction loss and the difficulties in growing large single crystals limits the specimen length.

Finally, the available information on attenuation losses in bonding materials is limited. Bobylev and Kravchenko (1967) have measured the loss in bonding films and give a value of approximately $8 \times 10^{-3}\ dB/\mu sec$ per reflection at *150 MHz*. Losses within this order can be tolerated provided they remain within these limits over the temperature range of the experiment. Many tests in this laboratory have been made and the results justified this assumption.

Measurements of the absolute value of attenuation have not been attempted nor are required in these experiments. The changes which occur in the attenuation as a function of temperature are the measurements of interest. Hence, relative accuracy is the important criterion and this is better than ±5%. The attenuation measured in crystals of $Hg_3In_2\square Te_6$ at *10 MHz* is high *(2.75 dB/μsec)*, the values just keeping within the scale of the measuring instrument at certain temperatures; at higher

frequencies the situation becomes worse, preventing the formation of satisfactory echo trains. Unfortunately, the attenuation measured in the mercury gallium telluride crystal samples was too high to be satisfactorily measured over the whole temperature range, however, this was possible on crystals of $Hg_3In_2\square Te_6$; these results will be presented.

The main limitation in measuring velocity is imposed by the measuring instrument, a calibrated delay generator which measures the transit time to an accuracy of *1%*. The error involved in measuring the sample length by micrometer is *0.2%*, this and other sources of error compared to the transit time error are negligible. The maximum scatter in the experimental points on the elastic moduli curves for all three compounds occurs in the results obtained from propagating a longitudinal wave down the $|110|$ direction. The maximum deviation of any point from the line of regression fit to the results is *2.5%*, giving a deviation of *1%* in the velocity measurements, this is because the elastic moduli are dependent upon the square of the velocity ($E = \rho v^2$). The quoted error in the transit time measurements compares exactly with this deviation.

The total expected error in the measurement of the elastic moduli from all sources is

error in density	≃	*0.02%*
error in length	≃	*2 x 0.2%*
error in transit time	≃	*2 x 1%*
total error in elastic moduli	≃	*2.5%*

The change in length of the specimens due to thermal expansion over the temperature range of the experiment will naturally cause an error in the velocity measurements. An estimate of the probable size of this

error can be obtained from the measured values of the thermal expansion coefficient of *HgTe* itself. The value at $77^{o}K$ is $(\Delta L/L)_{77} = .6 \times 10^{-4}$ giving a maximum error in the velocity at this temperature of *0.06%*, calculated using the room temperature length. This is negligible even if the thermal expansion coefficient is an order of magnitude greater for the ternary compounds used here, which is most unlikely.

The effect of small misorientations leads to an error in the elastic constants because the equations (3.38, 3.39 and 3.40) developed, are for specific directions, $|110|$ in this case. In these experiments the single crystals aligned to within $\pm 0.5^{o}$ of the crystallographic axis by use of Laue back reflection photographs (Section 2.4). By accident an $Hg_5Ga_2\square Te_8$ sample was misaligned by 4^{o} from the $|110|$ crystallographic axis and velocity measurements were taken over the complete temperature range when propagating longitudinal and both shear ultrasonic waves. The error produced by this misorientation angle in the velocity of each type of wave is,

$$\frac{\Delta v}{v} = 2.56 \times 10^{-2} \text{ for a wave polarized in the } |110| \text{ direction,}$$

$$\frac{\Delta v}{v} = 4.9 \times 10^{-2} \text{ for a wave polarized in the } |1\bar{1}0| \text{ direction}$$

and

$$\frac{\Delta v}{v} = 8.35 \times 10^{-2} \text{ for a wave polarized in the } |001| \text{ direction.}$$

Maximum error occurs in the slow shear wave which is related to the elastic constants by $\rho v^2 = (C_{11} - C_{12})/2$. Waterman (1959) has shown that the per unit change in velocity due to small misorientations in cubic crystals is proportional to the square of the misorientation angle. Hence assuming that the crystals are misaligned to the error limit of the goniometer $\pm 0.5^{o}$; the error which could be introduced in the wave

polarized in the |001| direction is 0.13%. This is insignificant relative to the 1% error imposed by the measuring equipment on the velocity value, even though the misorientation error is a maximum for the slow shear wave.

4.6 THE EXPERIMENTAL SYSTEM

The sample holder (Figure 4.5) was designed to maintain electrical contact with the transducer, which of course is bonded to the sample, during the temperature range of the experiment from $77^{o}K$ to ambient without altering the character of the bond. To achieve this; the specimen *(A)* was held in tension between a movable platform *(B)* located on three vertical guide legs *(C)*, only two of which are shown for convenience, and the sample holder head. Springs *(D)* on the guide legs exert the pressure which was controlled by means of an adjusting screw *(E)*. *R.F.* power was fed to the inner electrode of the transducer via a spring loaded copper brush *(G)*, centrally positioned in the sample holder head by a P.T.F.E. sleeve. The diameter of this sleeve allowed the outer electrode ring of the transducer to be earthed to the sample holder head, allowing the circuit of the *R.F.* pulsed oscillator to be completed. A stainless steel tube joining the sample holder and the cryostat cover *(F)*, positioned the sample just above the bottom of the cryostat. This tube was also used to carry the coaxial line connecting the oscillator and the transducer contact.

The cryostat (Figure 4.5) enabled the temperature of the sample to be raised or lowered at a slow rate by causing the heat given or taken from the sample to leak across a partial vacuum. It consisted of a double walled circular brass container, the inner diameter being 3 *cm*, giving sufficient clearance to allow the sample holder to slide into position. A flange, containing a slot for an *O* ring seal was brazed to the top of the container and this provided a seat for the

cover which was screwed down to give an airtight seal. The outer wall was a brass tube sealed at the bottom and brazed into position. This provided a space between the walls, which was evacuated by the usual diffusion pump-backing pump combination. Finally, there was a mechanism which allowed the dewar, containing liquid nitrogen, to be raised or lowered slowly over the end of the cryostat. This coupled with the partial vacuum created between the cryostat walls gave a measure of control over the temperature of the sample; allowing ample time for the ultrasonic measurements to be taken at regular temperature intervals.

The temperature was measured by precalibrated copper-constanton thermocouples, the junction being made by spark welding. One junction was sited adjacent to the sample and another, the reference junction in series with the sited junction, was held at $0^{o}C$ by immersion in melting ice. The emf produced by the temperature difference between the junctions was measured by a Tinsley potentiometer, capable of measuring to an accuracy of $0.1\mu V$.

To prevent the development of a temperature gradient across the sample it was immersed in a non-flammable, five component, organic mixture of *14.5%* chloroform, *25.3%* methylene chloride, *33.4%* elthye bromide, *10.4%* transdichloro-ethylene and *16.4%* trichloromethylene (Keyes 1962). The effect of a temperature gradient across the sample would be to alter the elastic moduli E and the density ρ. Hence there will be a change in the ultrasonic wave velocity v. The per unit change in v and E are related, assuming ρ constant, by

$$\frac{\Delta v}{v} = \frac{1}{2}\frac{\Delta E}{E} \qquad (4.3)$$

and the elastic constant data for $Hg_3In_2\square Te_6$ gives the percentage modulus variation with temperature by the relationship

$$\frac{\Delta E}{E} = 2.4 \times 10^{-4} \Delta T \qquad (4.4)$$

for a longitudinal wave. Then for a $0.1^{o}K$ temperature variation in the sample during the measurement the percentage change in the velocity was 1.2×10^{-3}% which is infinitesimal and is completely masked by the probable error of 1% caused by the measuring equipment. The error produced in the velocity measurements in the compounds $Hg_5Ga_2\square Te_8$ and $Hg_3Ga_2\square Te_6$ is in the same order. A temperature gradient in excess of $0.1^{o}K$ could influence the attenuation but this is easily recognised; the echo pattern taking a shape similar to that produced by a wedge shaped sample.

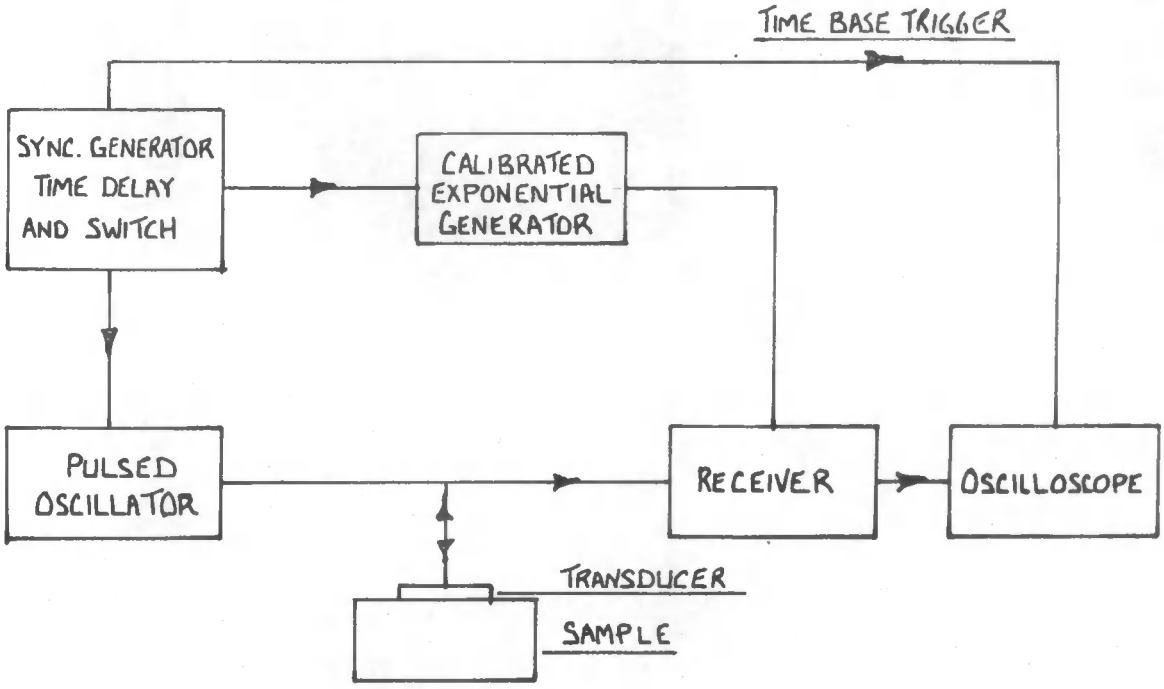

Fig. (4.1) Block diagram of the ultrasonic pulse echo system

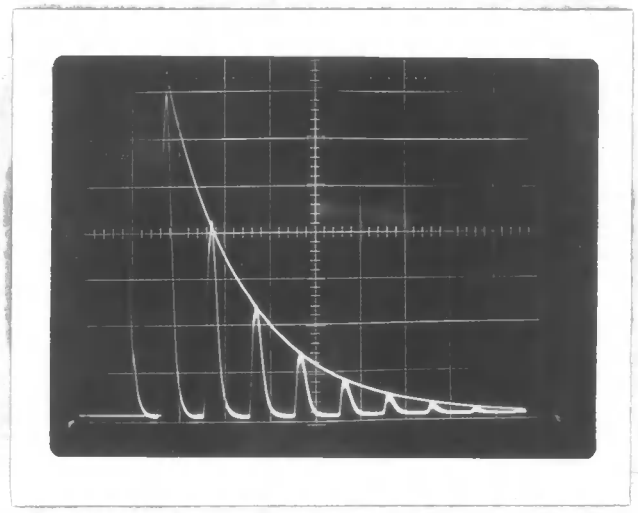

Fig. (4.2) Typical pulse train

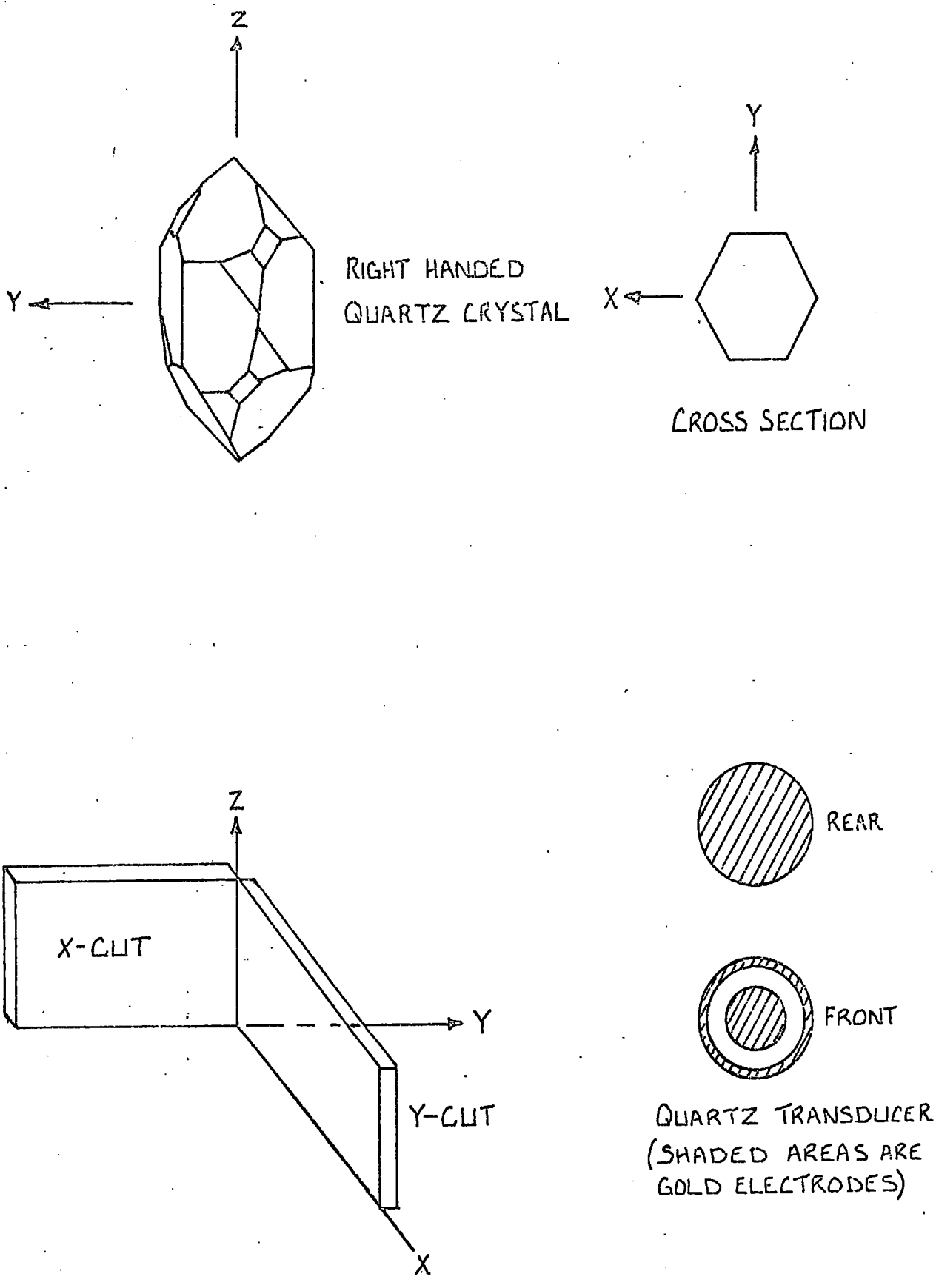

Fig. (4.3) Cuts taken from quartz crystal to give longitudinal and transverse transducers.

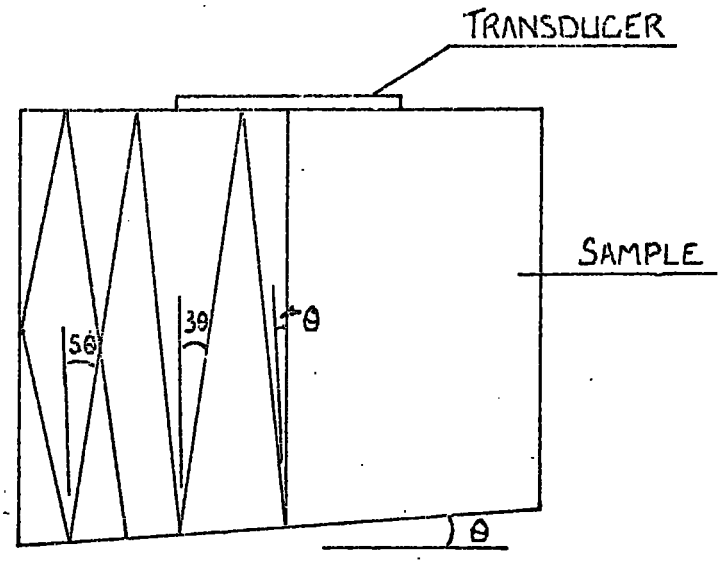

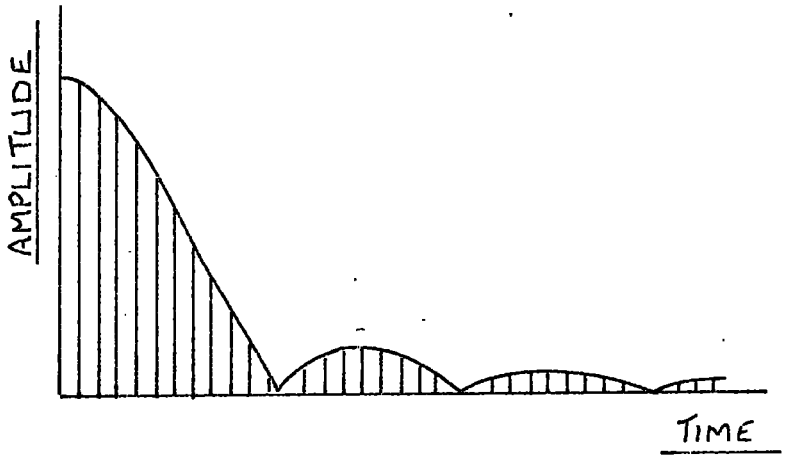

Fig. (4.4) Wedge sample and modulated pulse train

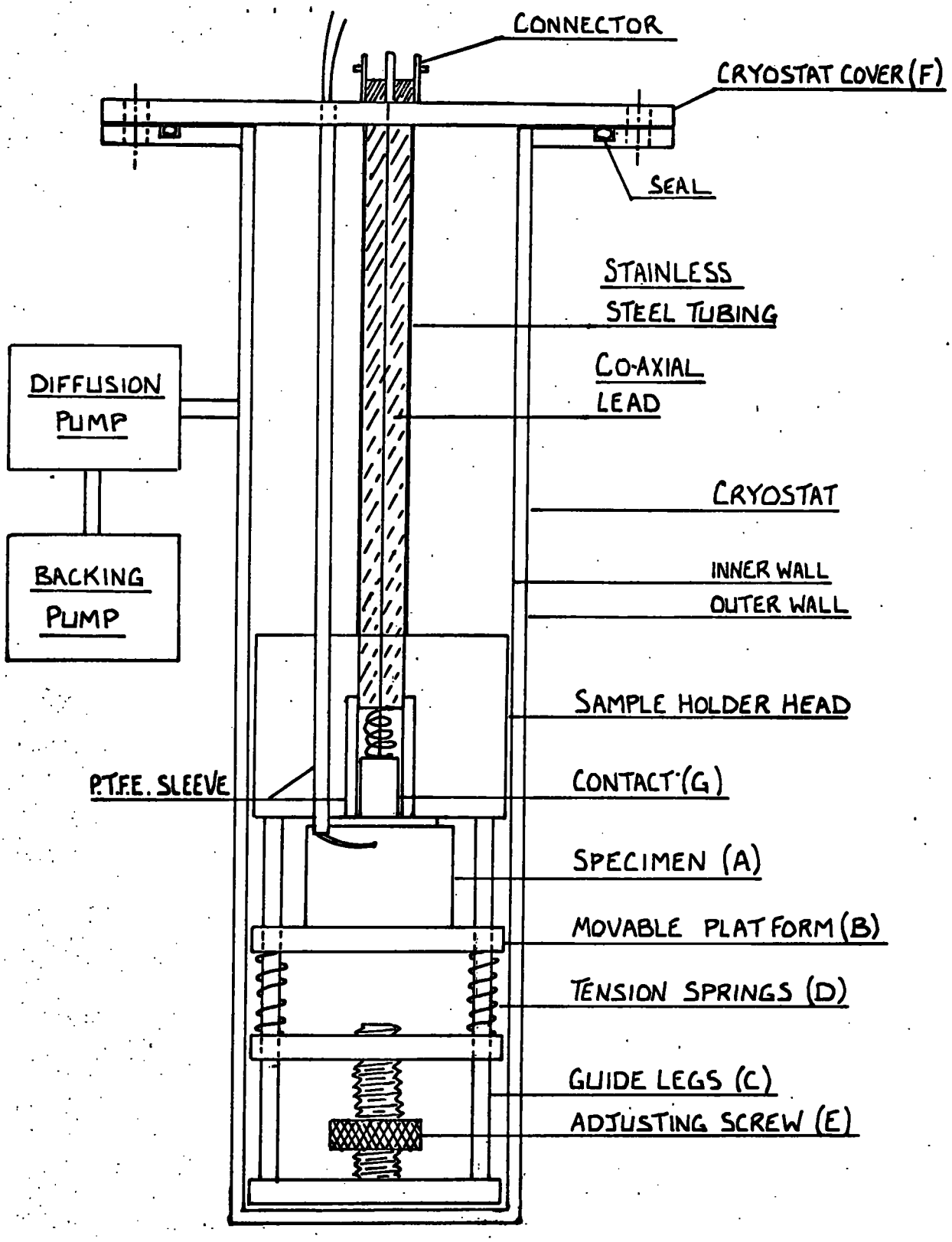

Fig. (4.5) Sample holder and cryostat used in the ultrasonic experiments

CHAPTER 5

RESULTS DERIVED FROM THE VELOCITY MEASUREMENTS AND DISCUSSION

5.1 THE ELASTIC MODULI AND ASSOCIATED PARAMETERS

5.1.1 Velocity Measurements The elastic moduli $(C_{11} + C_{12} + 2C_{44})/2$, C_{44} and $(C_{11} - C_{12})/2$, corresponding to the three wave velocities in the $|110|$ direction in the cubic compounds $Hg_3In_2\square Te_6$, $Hg_5Ga_2\square Te_8$ and $Hg_3Ga_2\square Te_6$ are presented as a function of temperature in Figures (5.1), (5.2) and (5.3). These results, calculated using the wave velocity expressions (3.45), (3.46) and (3.47), are an average of a series of measurements made over the temperature range 77^oK to about ambient. The maximum temperature at which a measurement was made depended critically on the quality of the bond and the material used (section 4.4). In each case, the curve drawn is a line of regression fit from a computer calculation on the experimental points. The maximum deviation of any point from the curves was found in the moduli corresponding to the longitudinal wave velocity and was 2%; deviations for the transverse waves were always much less than this, being at most 0.5% for any compound.

The temperature dependence of these moduli is best illustrated by the slope of each curve $(\Delta E/\Delta T)$. A table of values (5.1) is given. All three moduli of each compound decrease with increasing temperature in common with those of HgTe (Alper and Saunders 1967) and $Hg_5In_2\square Te_8$ (Alper et al 1968), the temperature dependence of which is also listed. Table (5.1) shows that the per unit change in the moduli of each compound is comparable with that of the parent compound HgTe and, with the exception of $Hg_3Ga_2\square Te_6$, the moduli C_{44} and $(C_{11} - C_{12})/2$ are less temperature dependent than the moduli associated with the longitudinal wave $(C_{11} + C_{12} + 2C_{44})/2$.

The elastic moduli of each compound at 77^oK, taken as the common temperature, together with the values obtained for HgTe (Alper and

Table (5.1) The temperature dependence of the measured elastic moduli of each compound expressed in per unit values

	$Hg_3In_2\square Te_6$	$Hg_5In_2\square Te_8$	HgTe	$Hg_3Ga_2\square Te_6$	$Hg_5Ga_2\square Te_8$
$\Delta\left(C_{44}\right)/\Delta T$	0.05×10^{-2}	0.013×10^{-2}	0.1×10^{-2}	0.07×10^{-2}	zero
$\Delta\left(C_{11} - C_{12/2}\right)/\Delta T$	0.023×10^{-2}	0.12×10^{-2}	0.023×10^{-2}	0.06×10^{12}	0.002×10^{-2}
$\Delta\left((C_{11} + C_{12} + 2C_{44})/2\right)/\Delta T$	0.14×10^{-2}	0.9×10^{-2}	0.21×10^{-2}	0.032×10^{-2}	0.127×10^{-2}

Saunders 1967) and $Hg_5In_2\square Te_8$ (Alper et al 1968) are listed in Table (5.2). Calculated from these moduli are the elastic constants C_{11}, C_{12} and C_{44}, and related parameters such as the bulk modulus, anisotropy ratio, the Cauchy relationship and the Debye temperature. Also, for the sake of completeness, the elastic compliance constants S_{11}, S_{12} and S_{44}, calculated using the transformation expression (3.15), are also presented in Table (5.2). The elastic moduli of similar compounds are in each case comparable and the underlying trend, which also applies for the elastic constants C_{11}, C_{12} and C_{44}, is for the values to reduce through the compound series $HgTe$, $Hg_5In_2\square Te_8$ and $Hg_3In_2\square Te_6$. This is repeated in the series $HgTe$, $Hg_5Ga_2\square Te_8$ and $Hg_3Ga_2\square Te_6$.

5.1.2 Anisotropy Ratio This factor which is simply the ratio of the shear stiffness moduli

$$A_R = \frac{2C_{44}}{C_{11} - C_{12}} \qquad (5.1)$$

can be used to assess the anisotropic nature of a cubic crystal. A purely isotropic material has a single shear modulus and this ratio is unity. The results obtained here, show that each crystal is markedly anisotropic and the value falls within the range occupied by similar compounds (for $ZnTe$, $A_R = 2.05$ and for ZnS, $A_R = 2.35$), further they reduce through each compound series repeating the trend shown in the elastic constant data.

5.1.3 The Cauchy Relationship and the Force Constants

In addition to the symmetry conditions imposed on the elastic stiffness C_{ijkl} by Hooke's Law and the positive definite form of the strain energy (section 3.2), a further symmetry condition can be applied when (i) a structure is such that each atom is located at a centre of symmetry and (ii) the potential energy depends only on the magnitude of the interatomic distance between pairs of atoms; that is a central force law. The internal strains of such a structure are zero (Musgrave, page 234

Table (5.2)

Comparison between each compound of the elastic moduli, elastic stiffness constants (units are 10^{11} dyn cm^{-2}) and the elastic compliance constants (units are 10^{-11} cm^2 dyn^{-1}) at $77^{o}K$.

Elastic Constant	$Hg_3In_2\square Te_6$	$Hg_5In_2\square Te_8$	HgTe	$Hg_3Ga_2\square Te_6$	$Hg_5Ga_2\square Te_8$
$(C_{11} + C_{12} + 2C_{44})/2$	5.48	6.25	7.13	5.66	6.24
$(C_{11} - C_{12})/2$	0.846	0.84	0.88	1.03	0.91
C_{44}	1.99	2.08	2.21	2.14	2.18
C_{11}	4.33	5.02	5.8	4.55	4.97
C_{12}	2.64	3.33	4.04	2.49	3.14
S_{44}	0.503	0.481	0.452	0.467	0.459
S_{11}	0.429	0.426	0.439	0.358	0.395
S_{12}	- 0.163	- 0.170	- 0.166	- 0.127	- 0.153

or Born and Huang, page 134) which reduces the energy density of the lattice directly to a value given by the classical expression (3.11). The symmetry implied by this reduction is

$$C_{ijkl} = C_{ikjl} = C_{iljk} \tag{5.2}$$

and the number of independent elastic constants is reduced from *21* to *15*, where

$$C_{23} = C_{44} \;,\quad C_{14} = C_{56} \tag{5.3}$$

$$C_{13} = C_{55} \;,\quad C_{23} = C_{46}$$

$$C_{12} = C_{66} \;,\quad C_{36} = C_{45}$$

These are known as the Cauchy relations and in the case of a cubic crystal

$$C_{12} = C_{44} \quad (= C_{66}) \tag{5.4}$$

The extent to which this relationship is fulfilled is often used to assess the validity of the assumption of a central force model. Here, the ratio C_{12}/C_{44} reduces through each compound series; the compound $Hg_3Ga_2\square Te_6$ has the closest value *(1.16)* to unity. These compounds do not obey the Cauchy relationship. However it is useful to have an estimate of the force constants since comparison between them for the different compounds gives a qualitative estimate of the change in bonding forces through each compound series.

Born, by considering nearest neighbour interactions only, developed a two-constant model to describe the elastic behaviour of diamond and zincblende lattices. A test of the adequacy of the model for a given compound is the "Born relation"

$$A = \frac{|4\, C_{11}(C_{11} - C_{44})|}{(C_{11} + C_{12})^2} = 1 \qquad (5.5)$$

This parameter is rather less than unity for each compound (Table 5.3) but the deviation is not excessive and the model can evidently provide a reasonable first approximation. Deviations from this model in binary compounds falling within the *II-VI* groups are attributed to the mixed ionic-covalent nature of the binding forces, the trend being that as the compounds become more ionic in character (Potter 1957) the value of the ratio *A* decreases possibly as a result of the longer range ionic forces. This pattern is not repeated in the ternary compounds measured here.

By this model elastic constants are related to the Hooke's law constants α and β (which arise from the radial and angular forces respectively) as follows:

$$C_{11} = \frac{\alpha}{2d} \qquad (5.6)$$

$$C_{11} + C_{12} = \frac{\beta}{d} \qquad (5.7)$$

$$C_{44} = \frac{\alpha}{2d}\left(1 - \frac{\beta^2}{\alpha^2}\right) \qquad (5.8)$$

where d is the nearest neighbour distance $\sqrt{3}\, a_o/4$ for zincblende structures. The calculated values of α and β are given in Table (5.3), and demonstrate that these interatomic forces decrease through the sequence $HgTe$, $Hg_5In_2\square Te_8$ ($Hg_5Ga_2\square Te_8$) $Hg_3In_2\square Te_6$ ($Hg_3Ga_2\square Te_6$).

5.1.4 Ionicity The cubic zinc sulphide (zincblende) structure can be considered as being derived from a face centred cubic lattice array which generates *N* octahedral interstitial sites and *2N* tetrahedral sites: if half the tetrahedral sites are fitted in an ordered way by a second type of ion, then the zincblende structure results. The

tetrahedral co-ordination is favoured by: *(a)* an ionic radius ratio below *0.414; (b)*cations with high polarizing power (e.g. Zn^{2+}, Hg^{2+}, Ga^{3+}, In^{3+}) and ions which are readily polarizable (e.g. Se^{2-}, Te^{2-}) and *(c)* factors which tend to give tetrahedral covalent bonds (e.g. *B.N., SiC*) or hydrogen bonds (e.g. NH_4F). Clearly it is unrealistic to distinguish between the purely ionic and purely covalent compounds in this structure, and the charges on the ions are merely a formal indication of their valency.

This type of lattice has been considered by various workers and a summary of their findings has been given by Born and Huang (1954). It is shown that the transverse optical frequency is related to the longitudinal mode frequency, the ionic charge *Ze*, the static and high frequency dielectric constants ε_o and ε_α by the expression

$$\omega_o^2 = \omega_1^2 \left(\frac{\varepsilon_\alpha}{\varepsilon_o} \right) \left(\frac{\varepsilon_o + 2}{\varepsilon_\alpha + 2} \right) - \frac{4\pi (Ze)^2}{3\bar{m} v_a} \left(\frac{\varepsilon_\alpha + 2}{3} \right) \qquad (5.9)$$

where $\bar{m}$ is the reduced mass of the primitive cell and v_a is its volume $(a_o^3/4)$ for zincblende structures. By considering ionic overlap potentials Szigeti (1950) derived a relationship between the bulk modulus *B* and the optical modes which can be written

$$\omega_1^2 = \frac{4Ba_o}{\bar{m}} \left(\frac{\varepsilon_\alpha + 2}{\varepsilon_o + 2} \right) \left(\frac{\varepsilon_o}{\varepsilon_\alpha} \right) \simeq \frac{4Ba_o}{\bar{m}} \qquad (5.10)$$

The frequency values obtained by using this expression are low compared to the values obtained from measured restrahlen frequencies but it is assumed that this is due to the covalent bonding existing in these lattices. ω_1 in equation (5.9) may be eliminated by using the Lyddane, Sachs and Teller (1941) relationship $\omega_o^2 = \omega_1^2 (\varepsilon_\alpha/\varepsilon_o)$ to give

$$\omega_o^2(\varepsilon_o - \varepsilon_\alpha) = \frac{4\,(Ze)^2}{\bar{m}v_a}\left[\frac{\varepsilon_\alpha + 2}{3}\right]^2 \qquad (5.11)$$

which was used by Spitzer and Fan (1955) to estimate the effective charge on *InSb*. Potter (1957) has developed a semi-empirical method of determining ω_1 and hence the value of Z from equation (5.9) by using the elastic moduli instead of the estimated dielectric constant difference. He compared with the group IV elements several binary compounds of the zincblende type having covalent or mixed ionic covalent bonding and showed that as the ionic character of the bond increases, the ratio C_{11}/C_{12} decreases in value. This ratio has a lower limit of unity imposed by Born's (nearest neighbour theory) lattice stability condition and it is assumed that at this level the lattice is completely ionic. Further, this condition suggest the bulk modulus reduces to C_{11} or C_{12} and equation (5.10) is

$$\omega_1^2 = \frac{4\,C_{11}a_o}{\bar{m}} \qquad (5.12)$$

for a completely ionic lattice, An expression which compares exactly with a relationship given by Born's theory for the fundamental frequency ω of the optical mode of vibration of a diamond lattice (covalent). Thus the similarity of the relationship between the modulus C_{11} and the longitudinal optical mode for the extreme covalent bond and the completely ionic bond suggested that equation (5.12) can be used to obtain a reasonable estimate of ω_1 for all zincblende lattices. The value obtained, coupled with the other parameters required by equation (5.9) enables an estimate of the effective ionic charge $(e^* = Ze)$ to be made. Comparison between a curve of C_{11}/C_{12} against the ionicity e^*/e determined by this

method and the values obtained using equation (5.11) shows reasonable agreement. An alternative expression

$$\frac{e^*}{e} = \left| \frac{1}{1.65} (\alpha - 2.65) \right|^2 \qquad (5.14)$$

where $\alpha = C_{11}/C_{12}$, has been developed from the curve and this has been used to make an estimate of the ionicity of each compound. Results are presented in Table (5.3).

While extension of Potters work to ternary compounds must be treated very cautiously, the results do show that the trend is for the ionicity to decrease with replacement of the mercury atoms by either indium or gallium atoms. In general, the extent to which polarization in binary zincblende compounds has enforced deviations from the predictions of the simple ionic radius ratio theory can be seen from the fact that very few of the elements forming these structures have formal values of ρ less than *0.414*, the value for *Hg-Te* being *0.5* and that for *In-Te* and *Ga-Te* is *0.357* and *0.281* respectively. Hence the replacement atoms fit into the lattice easily and it could be argued that a reduction in ionicity with an increase in replacement atoms arises because polarization of the *III-VI* bonds is less than that of the *II-VI* bonds, this being even more apparent for the bonds formed by the gallium atoms.

5.1.5 Debye Temperature Theoretically the specific heat at constant volume

$$C_v = \left(\frac{dQ}{dT} \right)_v = \left(\frac{\partial E}{\partial T} \right)_v \qquad (5.15)$$

is of interest since it is defined in terms of the energy of the system which in turn links with the vibrational energy. In metals and semiconductors this is considered to be associated with lattice

vibrations as the contribution from the electronic system is small. Hence the vibrational energy of a crystal containing N atoms can be considered to be equivalent to the energy of a system of $3N$ harmonic oscillators. This feature is common to all theories of specific heat and the distinction between the various theories is based on the difference in the proposed frequency spectrum of the oscillators. The theory of Debye (1912), which describes the experimental data well, is widely used because it is a one parameter model. The Debye temperature can be estimated from the elastic moduli as well as from heat capacity data. Debye assumed that the medium was a continuum for an elastic wave with a wavelength large compared to interatomic distances. Further, the fact that the crystal actually consists of atoms is taken into account by limiting the total number of vibrational modes to $3N$. In other words, the frequency spectrum corresponding to a perfect continuum is cut off so as to comply with a total of $3N$ modes. This procedure leads to a maximum frequency f_m; defined by

$$\int_0^{fm} N(f)\,df = 3N = \frac{4}{3}\pi V f_m^3 \int \left(\frac{1}{v_1^3} + \frac{1}{v_2^3} + \frac{1}{v_3^3}\right)\frac{d\pi}{4\pi} \qquad (5.16)$$

where V is the volume of the solid and $d\pi$ is an element of solid angle. Hence the total number of modes is actually the sum of the contributions from each type of elastic wave with velocities v_1, v_2 and v_3 averaged over all direction. In the specific heat context it is more useful to use a parameter related to temperature rather than frequency, this is the Debye temperature and is defined as

$$\theta = \frac{h}{k} f_m = \frac{h}{k}\left(\frac{9}{4\pi}\frac{N}{V}\right)^{1/3}\left[\int\left(\frac{1}{v_1^3} + \frac{1}{v_2^3} + \frac{1}{v_3^3}\right)\frac{d\Omega}{4\pi}\right]^{-1/3} \qquad (5.17)$$

where h and k are Planck's and Boltzmann's constants respectively. The specific heat at low temperature in terms of this parameter is then

$$C_v = \frac{12\pi^4 Nk}{5} \left(\frac{T}{\theta} \right)^3 \qquad (5.18)$$

At higher temperatures the expression is not so simple but is well defined. Initially this theory (1912) gave excellent agreement with experimental observations but Blackman (1935) showed that θ varied with temperature and agreement between values obtained from calorimetric and ultrasonic measurements occurs only at absolute zero, the error being approximately 10% at other temperatures. Hence values of θ_o calculated here have been made at 0^oK by extrapolation of the elastic moduli curves.

In order to obtain a solution to equation (5.17) it is first necessary to express the wave velocities in terms of the elastic constants obtained from the secular equation (3.38). The velocity surface produced has then to be evaluated and the shape is such that numerical integration is employed. Indirect but accuract methods of evaluating this integral for cubic structures have been developed; the graphical method due to Leibfried (1955), which is based on a polynominal expansion of the integrand developed by Quimby and Sutton (1953), is employed here. The appropriate graph (Alers 1965) of elastic moduli parameters C and K has been used to obtain a value of the parameter J which when used in the following expression gives the Debye temperature

$$\theta = \frac{h}{k} \left(\frac{3N}{4\pi V} \right)^{1/3} \left(\frac{C_{11} - C_{44}}{\rho} \right)^{1/2} J \qquad (5.19)$$

Table (5.3) Parameters determined from the elastic constants C_{ij} measured at $77^{o}K$.
The Debye temperature is based on values of C_{ij} obtained by extrapolating to $0^{o}K$.

	$Hg_3In_2\square Te_6$	$Hg_5In_2\square Te_8$	HgTe	$Hg_3Ga_2\square Te_6$	$Hg_5Ga_2\square Te_8$	ZnS
Bulk modulus: $(C_{11} + 2C_{12})/3$	3.20	3.89	4.62	3.18	3.75	
Anisotropy ratio: $2C_{44}/(C_{11} - C_{12})$	2.36	2.48	2.51	2.08	2.38	
Cauchy relation: C_{12}/C_{44}	1.33	1.60	1.83	1.16	1.44	
Born stability condition: $4C_{11}(C_{11} - C_{44})/(C_{11} + C_{12})^2$	0.84	0.85	0.86	0.88	0.84	
Force constants						
α	2.4×10^4	2.9×10^4	3.8×10^4	2.45×10^4	2.68×10^4	
β	1.9×10^4	2.4×10^4	3.2×10^4	1.90×10^4	2.19×10^4	
Ionicity: e^*/e	0.37 ± 0.04	0.47 ± 0.05	0.65 ± 0.05	0.25 ± 0.04	0.42 ± 0.04	0.65 (Potter 1957)
Debye temperature	147 ± 4°K	142 ± 6°K	141 ± 4°K	161 ± 4°K	151 ± 4°K	

The elastic constants used in the expressions of C, K and θ, are of course, values at $0^{o}K$. The Debye temperature obtained for each compound is presented in Table (5.3). These results show that while the difference between the Debye temperature of each compound is not very great, they do reduce somewhat in value through the series $HgTe$, $Hg_5In_2\square Te_8$ $(Hg_5Ga_2\square Te_8)$ and $Hg_3In_2\square Te_6$ $(Hg_3Ga_2\square Te_8)$. Further, the compounds containing gallium have a higher Debye temperature than an equivalent indium compound. To enable the comparison to be expanded, Debye temperatures for other *II-VI* compounds are presented and it is interesting to note that the values fall into a pattern; compounds composed of elements belonging to the higher periodic grouping have the lowest Debye temperature. The present results fit into this pattern; since gallium is within period four and indium in period five, the compounds containing gallium have a higher Debye temperature than the equivalent indium compounds. Further both the gallium and indium compounds containing the smallest percentage of mercury atoms (period six), $Hg_3In_2\square Te_6$ $(Hg_3Ga_2\square Te_6)$ have the highest Debye temperature. This pattern also seems to apply to *III-V* and *I-VII* compounds and the elements germanium (period 4) and silicon (period 3). ZnS $\theta_o = 346^{o}K$ (S. Bhagavantum 1955), $ZnSe$ $\theta_o = 273^{o}K$, $ZnTe$ $\theta_o = 220^{o}K$ (Alper 1968), $CdTe$ $\theta_o = 158^{o}K$ (McSkimm and Thomas 1962), $HgTe$ $\theta_o = 141^{o}K$ (Alper and Saunders 1967).

5.2 VELOCITY SECTIONS

In single crystals the ultrasound velocity depends upon the propagation direction $\underline{s}$; for any particular direction $\underline{n}$, three waves can be propagated. In general, these need not be either a pure longitudinal wave in the sense that the particle displacement vector is parallel to the wavefront normal $(\underline{s}\,||\,\underline{n})$, or a pure transverse wave, where the particle displacement vector is transverse to the wavefront

normal ($\underline{s} \times \underline{n} = o$); but regardless of direction the respective particle displacements of all three waves are orthogonal. To obtain the velocity of each wave, the determinant of the coefficients of Christoffel's equation

$$\begin{vmatrix} L_{11} - \rho v^2 & L_{12} & L_{13} \\ L_{12} & L_{22} - \rho v^2 & L_{23} \\ L_{13} & L_{23} & L_{33} - \rho v^2 \end{vmatrix} \begin{vmatrix} So_1 \\ So_2 \\ So_3 \end{vmatrix} = 0 \tag{3.38}$$

is equated to zero and solved for any chosen propagation direction. This is achieved by writing it as a general cubic equation in ρv^2:

$$(\rho v^2)^3 + A(\rho v^2)^2 + B(\rho v^2) + C = 0 \tag{5.20}$$

where

$$A = -(L_{11} + L_{22} + L_{33}) \tag{5.21}$$

$$B = (L_{11}L_{22} + L_{11}L_{33} + L_{22}L_{33} - L_{23}^2 - L_{12}^2 - L_{13}^2) \tag{5.22}$$

and

$$C = (L_{11}L_{23} + L_{12}^2L_{33} + L_{13}^2L_{22} - L_{11}L_{22}L_{33} - 2L_{12}L_{13}L_{23}) \tag{5.23}$$

The L_{ij} are quadratic functions of the direction cosines n_1, n_2 and n_3 and the elastic constants (see page 43). Then substituting the values of C_{ij} and the appropriate direction cosines will give a value of the functions A, B and C which allows the wave velocities to be

obtained from equation (5.20). If all possible values of the direction cosines are taken, the resultant velocities trace out these separate velocity surfaces. In this instance the elastic constants C_{11}, C_{12} and C_{44} of each compound at $77^{o}K$ have been used to obtain a solution. Two cross sections of the velocity surfaces, which correspond to the *(001)* and *(1$\bar{1}$0)* planes of a cubic lattice, have been determined for *HgTe* and its associated compounds in both the mercury-indium-telluride and mercury-gallium-telluride series. The results are presented in Figures (5.4) to (5.13).

The *(001)* plane is of interest because the determinant of equation (3.38) can be simplified if the wave normal lies in a cube face, so that the direction cosines have the form $(n_1, n_2, 0)$. This reduces the Kelvin-Christoffel stiffnesses to

$$L_{11} = n_1^2 C_{11} + n_2^2 C_{44} \tag{5.24}$$

$$L_{22} = n_1^2 C_{44} + n_2^2 C_{11} \tag{5.25}$$

$$L_{33} = (n_1^2 + n_2^2) C_{44} \tag{5.26}$$

and

$$L_{12} = n_1 n_2 (C_{12} + C_{44}) \tag{5.27}$$

L_{13} and L_{23} are zero. Substituting these expressions in the determinant allows it to be written, for the sake of economy, in the form

$$H \left| H^2 - (C_{11} - C_{44})H + (C_{11} - C_{12} - 2C_{44})(C_{11} + C_{12}) n_1^2 n_2^2 \right| = 0 \tag{5.28}$$

where $H = \rho v^2 - C_{44}$. This equation has a linear and a quadratic factor. Reference to the secular equation makes it clear that the root $H = 0$,

$$\rho v^2 = C_{44} \tag{5.29}$$

is associated with a displacement in the $|001|$ direction, regardless of the propagation direction in the (001) plane. This is a pure shear wave of constant velocity which traces out a circle on the (001) cross-section of the velocity surface. The two remaining roots are

$$H = \tfrac{1}{2}\left[(C_{11} - C_{44}) \pm \left\{ (C_{11} - C_{44})^2 - 4n_1^2 n_2^2 (C_{11} - C_{12} + 2C_{44}) \right.\right. \tag{5.30}$$

$$\left.\left. (C_{11} + C_{12}) \right\}^{\frac{1}{2}}\right]$$

where the positive sign corresponds to a wave which is predominately longitudinal in character and may be referred to as a quasi-longitudinal wave. Similarly, the negative sign relates to a quasi-transverse wave. The symmetry of these velocity sections exhibits the Laue symmetry of the plane. A particular solution to equation (5.28) in the $|100|$, $|010|$, $|\bar{1}00|$ and $|0\bar{1}0|$ directions shows that the velocities of the transverse waves are both $v_{TS} = v_{TF} = (C_{44}/\rho)^{\frac{1}{2}}$ and the velocity of the longitudinal wave is $v_L = (C_{11}/\rho)^{\frac{1}{2}}$. The velocity of each wave in the $|110|$ and equivalent directions is given by equations (3.45), (3.46) and (3.47).

The direction cosines for wave normals lying in the $(1\bar{1}0)$ plane take the form $(n_1, n_1 = n_2, n_3)$ which reduce the Kelvin-Christoffel stiffnesses to

$$L_{11} = n_1^2 C_{11} + (n_1^2 + n_3^2) C_{44} = L_{22} \tag{5.31}$$

$$L_{33} = (2n_1^2 + n_3^2) C_{44} \tag{5.32}$$

$$L_{12} = \frac{n_1^2 (C_{11} + C_{12})}{2} \tag{5.33}$$

and

$$L_{23} = n_1 n_3 (C_{12} + C_{44}) \tag{5.34}$$

Determinant (3.38) may be expanded and written as

$$\left[H - n_1^2(C_{11} - C_{12} - 2C_{44})\right] \left|H^2 - \left[C_{11} - C_{12} - n_1^2 (C_{11} - C_{12} - 2C_{44})\right]H\right.$$

$$\left. + (C_{11} - C_{12} - 2C_{44}) (C_{11} + C_{44} + 2C_{12})n_1^2 n_3^2\right| = 0 \qquad (5.35)$$

The roots are

$$H = n_1^2(C_{11} - C_{12} - 2C_{44}) \qquad (5.36)$$

which gives the velocity of the slow shear wave in this plane and

$$H = \tfrac{1}{2}\left| \left[C_{11} - C_{44} - n_1^2(C_{11} - C_{12} - 2C_{44}\right] \pm \left[\left[C_{11} - C_{44} - n_1^2 \right.\right.\right. \qquad (5.37)$$

$$\left.\left.\left. (C_{11} - C_{12} - 2C_{44})\right]^2 - 4 (C_{11} - C_{12} - 2C_{44})(C_{11} + C_{44} + 2C_{12})n_3^2 n_1^2\right]^{\frac{1}{2}}\right|$$

where the positive and negative signs correspond to quasi-longitudinal and quasi-transverse waves respectively. The symmetry of each velocity cross section is the same as the Laue symmetry of the plane: two fold. The velocity of the shear waves in the $|001|$ direction is the same $v = (C_{44}/\rho)^{\frac{1}{2}}$ a degeneracy predicted by the equal roots of equation (5.35), a situation which also occurs at 35^{o} to the *(001)* direction. The velocity of the longitudinal wave, the third root, is $v = (C_{11}/\rho)^{\frac{1}{2}}$. Then since the velocity of each wave in the $|110|$ direction is given by the original equations (3.45), (3.46) and (3.47) each velocity cross-section has two fold symmetry. In both the *(001)* and *(110)* planes the velocity cross-sections were obtained by solving equations (5.28) and (5.35) at one degree intervals. I am indebted to Dr. N. G. Pace for the use of a computer programme for this purpose.

These diagrams provide an opportunity to check the possible error in the velocity measurements due to misaligning the crystals which because of the goniometer scale is possible ±1%. The greatest change

in velocity about the pure mode direction probably occurs in the measurements on the $Hg_3In_2\square Te_6$ crystal, hence a misalignment error will be largest here. Then from the computer readout data the maximum error which occurs for 1^o misalignment is *0.02%* in the longitudinal wave velocity, *0.09%* in the fast shear wave velocity and *0.06%* in the slow shear wave velocity. These values are well within the *1%* accuracy claimed of the measuring system, hence a small misalignment is not critical.

Velocity cross-sections for each crystal in both *(001)* and *(110)* planes have the same geometrical shape, which is typical of a cubic material (Musgrave 1970). Isotropic materials produce velocity cross-sections which are circular in shape. Hence the relative degree of anisotropy of each crystal can be judged by the sharpness of the pattern in each plane. This can be related to the anisotropy ratio: *HgTe*, anisotropy ratio *(2.51)* has velocity cross-sections with a very pronounced pattern, while $Hg_3Ga_2\square Te_6$, anisotropy ratio *(2.08)*, has velocity cross-sections which have a more rotund shape.

5.3 ENERGY FLUX VECTORS FOR DIRECTIONS IN THE *(001)* PLANE

Of considerable interest both experimentally and theoretically are the energy flux vectors associated with elastic wave motion in anisotropic crystals. For example, in ultrasonic pulse-echo experiments, deviations of energy flow from the propagation direction can result in the wave impinging on the specimen side walls, giving rise to mode conversion and echo train deterioration. Thus, before any detailed studies of anisotropic, anelastic behaviour can be made, the energy flux vectors are required. Love (1944) has given the i^{th} Cartesian component of the energy flow P_i as

$$P_i = -\sigma_{ij}\dot{s}_j \tag{5.38}$$

where $\dot{s}_j$ is the j^{th} component of the particle displacement velocity. The plane wave equation (3.33) is substituted into this expression to give

$$P_i = -\frac{\omega^2}{2v} C_{ijkl} So_j So_k n_l \tag{5.39}$$

where v and n_l are respectively the wave propagation velocity and the propagation direction cosine relative to the l^{th} co-ordinate axis. So_j and So_k are the components of the particle displacement vectors relative to the j^{th} or k^{th} co-ordinate system. To develop an expression for the direction of the energy flux relative to a co-ordinate system which is co-incident with the cube edges of a cubic crystal, the expression (5.39) must be expanded. Take for example the component

$$P_l = C_{\substack{ijkl \\ l}} So_j So_k n_l \tag{5.40}$$

First put

$$j = 1, 2, 3, \quad \text{then}$$

$$P_l = C_{11kl} So_1 So_k n_l + C_{12kl} So_2 So_k n_l + C_{13kl} So_3 So_k n_l \tag{5.41}$$

Now let

$$k = 1, 2, 3, \quad \text{and}$$

$$\begin{aligned} P_l = {} & C_{1111} So_1 So_1 n_l + C_{12kl} So_2 n_l + C_{1131} So_1 So_3 n_l \\ & + C_{1211} So_2 So_1 n_l + C_{1221} So_2 So_2 n_l + C_{1231} So_2 So_3 n_l \\ & + C_{1311} So_3 So_1 n_l + C_{1321} So_3 So_2 n_l + C_{1331} So_3 So_3 n_l \end{aligned} \tag{5.42}$$

Finally let

$$l = 1, 2, 3, \quad \text{and}$$

$$P_1 = C_{1111}So_1So_1n_1 + C_{1112}So_1So_1n_2 + C_{1113}So_1So_1n_3$$

$$+ C_{1121}So_1So_2n_1 + C_{1122}So_1So_2n_2 + C_{1123}So_1So_2n_3$$

$$+ C_{1131}So_1So_3n_1 + C_{1132}So_1So_3n_2 + C_{1133}So_1So_3n_3$$

$$+ C_{1211}So_2So_1n_1 + C_{1212}So_2So_1n_2 + C_{1213}So_2So_1n_3$$

$$+ C_{1221}So_2So_2n_1 + C_{1222}So_2So_2n_2 + C_{1223}So_2So_2n_3$$

$$+ C_{1231}So_2So_3n_1 + C_{1232}So_2So_3n_2 + C_{1233}So_2So_3n_3$$

$$+ C_{1311}So_3So_1n_1 + C_{1312}So_3So_1n_2 + C_{1313}So_3So_1n_3$$

$$+ C_{1321}So_3So_2n_1 + C_{1322}So_3So_2n_2 + C_{1323}So_3So_2n_3$$

$$+ C_{1331}So_3So_3n_1 + C_{1332}So_3So_3n_2 + C_{1333}So_3So_3n_3$$

In the cubic system the elastic constant set includes only C_{11}, C_{12} and C_{44}, the remainder are zero (see page 38), which reduces the expression to

$$P_1 = \left|C_{11}So_1^2 + C_{44}(So_2^2 + So_3^2)\right|n_1 + (C_{12} + C_{44})\ So_1So_2n_2 \qquad (5.44)$$

$$+ C_{12} + C_{44})\ So_1So_3n_3$$

A similar expansion process shows that

$$P_2 = (C_{12} + C_{44})\ So_1So_2n_1 + \left|C_{11}So_2^2 + C_{44}\ (So_1^2 + So_3^2)\right|n_2 \qquad (5.45)$$

$$+ C_{12}So_2So_3n_3$$

and

$$P_3 = (C_{12} + C_{44})\, So_1 So_2 n_1 + (C_{12} + C_{44})\, So_2 So_3 n_2 + (C_{44}\, So_1^2 + C_{11} So_3^2) n_3 \quad (5.46)$$

The position of the energy flux vector in the *(001)* or *(xy)* plane, $P(P_1, P_2, 0)$ is considered since it corresponds to the *(001)* velocity sections and contains within it the pure mode $|110|$ direction. In this case the direction cosines are $(n_1, n_2, 0)$ and the components of the energy flux reduce to

$$P_1 = \left| C_{11} So_1^2 + C_{44}(So_2^2 + So_3^2) \right| n_1 + (C_{12} + C_{44})\, So_1 So_2 n_2 \quad (5.47)$$

and

$$P_2 = (C_{12} + C_{44})\, So_1 So_2 n_1 + \left| C_{11} So_2^2 + C_{44}(So_1^2 + So_3^2) \right| n_2 \quad (5.48)$$

Then, since P_3 the energy flux component along the $|110|$ direction (+ z axis) is zero for all three modes the energy flow is always within the *(001)* plane for any mode propagating along any direction in this plane and its direction may be described by an angle β which the energy flux vector makes with the $|001|$ direction (+ x axis).

$$\beta = \tan^{-1}\left(\frac{P_2}{P_1} \right) \quad (5.49)$$

For the pure transverse mode in which a wave can propagate with a velocity of $v = (C_{44}/\rho)^{\frac{1}{2}}$ in any direction within the plane, the polarization vector So_3 is in the $|100|$ direction and $So_1 = So_2 = 0$.

Equations (5.47) and (5.48) reduce to

$$P_1 = C_{44} So_3^2 n_1 \quad \text{and} \quad P_2 = C_{44} So_3^2 n_2 \tag{5.50}$$

and then

$$\beta_{TF} = \tan^{-1}\left(\frac{n_2}{n_1}\right) \tag{5.51}$$

In the case of the quasi-longitudinal and quasi-transverse modes in this plane

$$\beta = \tan^{-1} \frac{\left|C_{11}(\tan\phi)^2 + C_{44}\right| n_2 + (C_{12} + C_{44}) n_1 \tan\phi}{\left|C_{11} + C_{44}(\tan\phi)^2\right| n_1 + (C_{12} + C_{44}) n_2 \tan\phi} \tag{5.52}$$

where $\phi = \tan^{-1} So_2/So_1$ is the direction of the particle displacement vector. This ratio can be obtained from the secular equation (3.38) such that

$$\phi = \tan^{-1} \left| \frac{n_1^2 C_{11} + n_2^2 C_{44} - \rho v^2}{- n_1 n_2 (C_{12} + C_{44})} \right| \tag{5.53}$$

and v is the appropriate velocity obtained from equation (5.28). Alternatively the angle β_{TS} which the energy flux vector associated with the quasi-transverse mode makes with the positive x axis is obtained by replacing ϕ by $(\phi + \pi/2)$ in equation (5.52), since the particle displacement vectors are orthogonal.

For each of the compounds, the particle displacement directions and the energy flux directions associated with the three waves, which

can propagate along directions in the *(001)* plane are plotted in Figures (5.15) to (5.19) as angular deviations from the propagation direction versus the propagation direction in one quadrant. The symmetry ensures that this is repeated in the other quadrants. Particle displacement directions for the pure and quasi-pure transverse modes are not shown; the former is always perpendicular to the plane of the diagram and the latter always differs by $\pi/2$ from that for the quasi-longitudinal mode. A diagrammatic explanation is also given in Figure (5.14).

In each compound the condition that a pure longitudinal wave is propagated ($\underline{s}||\underline{n}$) is obeyed at 0^o and 45^o, the $|001|$, $|110|$ and equivalent directions. Since one of the transverse waves with a propagation vector in the *(001)* plane is always a pure mode, the propagation direction which supports the pure longitudinal mode must by orthogonality carry another pure transverse mode. At these pure mode propagation directions, the deviation of the energy flux vector of each wave from the propagation direction is zero. This occurs because of the symmetry of the mode axis. Waterman (1959) has discussed the effect of symmetry of propagation direction on the energy flux vector and showed that for a pure longitudinal mode, the energy flux vector cannot deviate from the propagation direction. The same result holds for a pure transverse mode provided the propagation direction is two fold, four fold or a six fold rotational axis or normal to a plane of reflection symmetry. If the propagation direction is not within these categories, then in general, a deviation of the energy flux from the propagation direction may be expected.

5.4 DISCUSSION

Details of the propagation of ultrasonic waves in ternary compound semiconductors are sparse. The present work furnishes an insight into the effects of extremely high vacancy concentrations on both the elastic and anelastic properties of the series of materials formed by the replacement of some of the mercury atoms by indium or gallium atoms in the compound *HgTe*. In each compound series there is a marked reduction in the crystal stiffness as the vacancy concentration increases (Table 5.2) Comparison between the elastic constants of the compounds is best effected through a normalisation procedure. The elastic properties of a material are basically determined by the interaction between electrons and lattice ions. Dimensional analysis (Huntington 1958) suggests that the elastic constants should be of the order q^2/r^4, where q is the electronic charge and r is some characteristic length of the lattice in question. Accordingly, Keyes (1962) in order to compare different materials with a zincblende structure has reduced their elastic constants to a set of dimensionless parameters by defining an elastic constant

$$C_o \equiv \frac{q^2}{d^4} \tag{5.54}$$

where d is the nearest neighbour atomic spacing, which in terms of the lattice spacing is $d = \sqrt{3}\, a_o/4$. The reduced bulk modulus and shear moduli are then

$$B^* = \frac{(C_{11} + 2C_{12})}{3C_o} \tag{5.55}$$

$$C_{44}^* = \frac{C_{44}}{C_o} \tag{5.56}$$

$$C_s^* = \frac{C_{11} - C_{12}}{2C_o} \qquad (5.57)$$

and the reduced average shear modulus is

$$C^* = \frac{C_{11} - C_{12} + 3C_{44}}{5C_o} \qquad (5.58)$$

The reduced moduli at 77^oK for the compounds studied here are presented in Table (5.4). The values obtained for *HgTe* fall directly into the range occupied by zincblende structure, *II-VI* compounds, namely that $B^* \simeq 1.1$ to 1.2, $C_{44}^* \sim 0.6$, $C_s^* \sim 0.2$ and $C^* \sim 0.4$ and they have a particularly close affinity with the reduced moduli of cubic *ZnS*. Thus Keyes generalizations concerning the elastic moduli of zincblende compounds and diamond structure elements, namely that $B^* \sim 1.2$ and the shear moduli decrease through the sequence, group *IV* elements, *III-V* compounds and *II-VI* compounds, find further confirmation in *HgTe*, which shows no anomalous elastic behaviour (Alper and Saunders 1967). This is not so for the compounds containing vacancies. The reduced moduli, like the actual moduli, decrease smoothly through the sequence *HgTe*, $Hg_5In_2\square Te_8$ ($Hg_5Ga_2\square Te_8$), $Hg_3In_2\square Te_6$ ($Hg_3In_2\square Te_6$). Further, the values obtained for equivalent compounds in each series are in close agreement within the tolerance claimed of the technique. Such a decrease in the stiffness would follow naturally from the increasing vacancy concentration and would be accompanied by a change in the lattice stability.

Born (1940) and his co-workers in a series of papers have discussed lattice stability, and have shown that the energy density of a lattice when subjected to a homogeneous deformation is

$$u = \tfrac{1}{2} \sum_{ij} C_{ij}\epsilon_i\epsilon_j \quad , \qquad (5.59)$$

Table (5.4) The reduced elastic stiffness moduli. Parameters are based on the elastic constants C_{ij} measured at $77^{o}K$.

	$Hg_3In_2\square Te_6$	$Hg_5In_2\square Te_8$	HgTe	$Hg_3Ga_2\square Te_6$	$Hg_5Ga_2\square Te_8$	ZnS (Keyes 1962)
Reduced moduli:						
$C_o = 256\ e^2/9a_o$	4.19 ± 0.02	4.08 ± 0.04	3.76 ± 0.01	4.39 ± 0.02	4.34 ± 0.04	
$(C_{11} + 2C_{12})/3C_o$	0.76 ± 0.04	0.95 ± 0.04	1.23 ± 0.03	0.72 ± 0.04	0.95 ± 0.04	1.11
C_{44}/C_o	0.48 ± 0.02	0.51 ± 0.02	0.60 ± 0.02	0.49 ± 0.02	0.51 ± 0.02	0.56
$(C_{11} - C_{12})/2C_o$	0.20 ± 0.02	0.21 ± 0.02	0.24 ± 0.02	0.23 ± 0.02	0.21 ± 0.02	0.24
Reduced average shear modulus:						
$(C_{11} - C_{12} + 3C_{44})/5C_o$	0.37 ± 0.02	0.39 ± 0.04	0.45 ± 0.02	0.39 ± 0.02	0.39 ± 0.02	0.43

when internal strains are eliminated. This result is strictly comparable with the strain energy function (equation 3.11) in classical elasticity theory. Thus the elastic stiffness constants C_{ij} are given by the second derivitive $\partial^2 u/\partial\varepsilon_i\partial\varepsilon_j$ of the interatomic binding energy with respect to strain ε. For the lattice to be stable when subjected to small strains, the energy density must be raised, if this were not so, the lattice would transform to another. Born also discussed lattice stability from the viewpoint of small vibrations and concluded that essentially the long wavelength region of the vibrational spectrum corresponding to elastic wave frequencies need only be taken into account. Again, the results show that for a lattice to be stable the above quadratic form, equation (5.59), must be positive definite so that the energy density is raised when the lattice is subjected to a homogeneous deformation. To fulfil this requirement, the determinants of the matrices of successive orders of the elastic constant C_{ij} matrix (the principle minors) must all be positive. The cubic form of this matrix, given below, is marked out with these sub-matrices.

$$\begin{vmatrix} C_{11} & C_{12} & C_{12} & 0 & 0 & 0 \\ C_{12} & C_{11} & C_{12} & 0 & 0 & 0 \\ C_{12} & C_{12} & C_{11} & 0 & 0 & 0 \\ 0 & 0 & 0 & C_{44} & 0 & 0 \\ 0 & 0 & 0 & 0 & C_{44} & 0 \\ 0 & 0 & 0 & 0 & 0 & C_{44} \end{vmatrix} \qquad (5.60)$$

The principle minors are

$$C_{44},\ C_{44}^2,\ C_{44}^3,\ C_{44}^3 C_{11},\ C_{44}^3(C_{11}^2 - C_{12}^2),\ C_{44}^3(C_{11} - C_{12})^2$$

$$(C_{11} + 2C_{12}).$$

For these to be positive only the following conditions need be fulfilled,

$$C_{44} > 0, \quad C_{11} - C_{12} > 0, \quad C_{11} + 2C_{12} > 0 \tag{5.61}$$

In physical terms this means that both the shear moduli C_{44} and $(C_{11} - C_{12})/2$, and the bulk modulus $(C_{11} + 2C_{12})/3$ must be greater than zero for a cubic lattice to be stable. Hence any change in the value of these moduli in this series of compounds will indicate the relative stability of the structures. In fact, there is a reduction in both the reduced shear moduli of the vacancy compounds $Hg_5In_2\square Te_8$ $(Hg_5Ga_2\square Te_8)$ and $Hg_3In_2\square Te_6$ $(Hg_3Ga_2\square Te_6)$ compared with the zero vacancy parent compound *HgTe*. Table (5.5) gives this reduction $\Delta|C_{44}/C_o|$ and $\Delta|(C_{11} - C_{12})/2C_o|$ for each compound as a percentage using the appropriate reduced shear moduli of *HgTe* as a base. This table shows that the percentage reduction in C_{44}/C_o progressively increases through each compound series from $Hg_5In_2\square Te_8$ $(Hg_5Ga_2\square Te_8)$ to $Hg_3In_2\square Te_6$ $(Hg_3In_2\square Te_6)$; the reduction in C_{44}/C_o is progressive as the vacancy concentration increases from *6.25%* to *8.33%*. A reduction also occurs in $(C_{11} - C_{12})/2C_o$ in each compound series but the change in this modulus is not large compared with the experimental errors; there is an exact correspondence between the values obtained for this modulus and the C_{44}/C_o modulus in each of the compounds $Hg_5In_2\square Te_8$ and $Hg_5Ga_2\square Te_8$. The reduced moduli C_{44}/C_o and $(C_{11} - C_{12})/2C_o$ enable the resistance of each compound to deformation, when a shear stress is applied across a *(001)* plane in the $|001|$ and $|1\bar{1}0|$ directions respectively, to be compared. Clearly, the resistance to a shear stress decreases as the vacancy concentration in each compound increases and as a consequence there is a reduction in the stability of the structure.

The stability of the lattice is also linked with the bulk modulus $(C_{11} + 2C_{12})/3$ or its inverse the compressibility which is the proportional

Table (5.5) The percentage reduction in the normalized shear moduli based on the reduced shear moduli of *HgTe*. Parameters are based on the elastic constants C_{ij} measured at $77^{o}K$.

	$Hg_3In_2\square Te_6$	$Hg_5In_2\square Te_8$	$Hg_3Ga_2\square Te_6$	$Hg_5Ga_2\square Te_8$
$\Delta\left(C_{44}/C_o\right)$	20	15	18	15
$\Delta\left((C_{11} - C_{12})/2C_o\right)$	16	12	4	12

decrease in volume of a crystal when subjected to unit hydrostatic pressure. Like the other stiffness moduli, the bulk moduli decrease through the sequence $HgTe$, $Hg_5In_2\square Te_8$ ($Hg_5Ga_2\square Te_8$) and $Hg_3In_2\square Te_8$ ($Hg_5Ga_2\square Te_8$). A plot of the reduced bulk moduli B^* against the percentage of vacancies (Figure 5.20) produces a fact of fundamental import: the bulk modulus is a linear function within experimental error of the number of vacancies present. Thus the change in reduced bulk modulus ΔB^* or its inverse the reduced compressibility ΔK^* can be expressed in terms of the vacancy percentage (η) by

$$\Delta B^* = \frac{1}{\Delta K^*} = 0.053\eta \qquad (5.62)$$

Each additional vacancy increases the compressibility by the same amount. This suggests a general law for the change in compressibility due to an ordered array of vacancies.

If the line in Figure (5.20) is extrapolated out to higher vacancy concentrations the reduced bulk modulus becomes zero at 23% ± 1% vacancies. A solid with zero bulk modulus cannot be stable and the crystal structure must change. This has also been suggested by the reduction in the shear moduli as the vacancy concentration is increased. In fact, the phase diagrams for both series of compounds (Figures 2.1 and 2.2) show that centred on 75% In_2Te_3 (Ga_2Te_3) a compound $HgIn_2\square Te_4$ ($HgGa_2\square Te_4$) exists containing 12.5% vacancies and having a chalcopyrite (tetragonal) structure with a unit cell approximately twice the size of that for zincblende (Hahn et al 1955 and Ray et al 1969). The boundaries of this region are about 70% In_2Te_3 (Ga_2Te_3), which corresponds to 12% vacancies and 80% In_2Te_3 (Ga_2Te_3). Between the cubic compounds $Hg_3In_2\square Te_6$ and $Hg_3Ga_2\square Te_6$ centred on 50% In_2Te_3 (Ga_2Te_3) and the tetragonal compounds $HgIn_2\square Te_4$ and $HgGa_2\square Te_4$ there exists a two phase region between approximately 54% In_2Te_3 (Ga_2Te_3), 9% vacancies, and 70% In_2Te_3 (Ga_2Te_3), 12% vacancies, containing grains of both compounds. It is tempting to

suggest that this two phase region is stabilized because the high compressibility $Hg_3In_2\square Te_6$ ($Hg_3Ga_2\square Te_6$) grains are surrounded by a matrix of $HgIn_2\square Te_4$ ($HgGa_2\square Te_4$) and that when the bulk modulus of the former grains falls below *0.59* at *12%* vacancies the cubic structure can no longer be held and all the material transforms completely to the $HgIn_2\square Te_4$ ($HgGa_2\square Te_4$) chalcopyrite structure.

In conclusion, the reduction in the elastic stiffness constants C_{11}, C_{12} and C_{44}, the reduced shear moduli C_{44}/C_o and $(C_{11} - C_{12})/2C_o$, and the reduced bulk moduli $(C_{11} + 2C_{12})/3C_o$ through each compound series suggests that as the vacancy concentration in the structure is increased the lattice becomes progressively less stable. A reduction in the stability of the lattice must be accompanied by a reduction in the binding forces which in this case occurs as a result of the presence of vacancies: certain nearest neighbour interactions are missing. The results produced by the two force constant model adopted here, where a progressive reduction in the force constants through each compound series occurs, is consistent with this behaviour. In the limit if one of the shear moduli C_{44} or $(C_{11} - C_{12}/2$ or the bulk modulus $(C_{11} + 2C_{12})/3$ tend to zero, the lattice cannot hold and it will change into another form. Behaviour of this type is not uncommon. Novotny and Smith (1965) found that the onset of instability of *f.c.c.* indium-thallium alloys is directly associated with the approach of $(C_{11} - C_{12})/2$ towards zero. These crystals are unstable to and are transformed by this particular shear. Recently, Pace and Saunders (1971) have investigated the elastic moduli on either side of this *f.c.c.* to *f.c.t.* transition, which can be either temperature or composition dependent. In each case it was found that anomalies occurred in the shear moduli C_{44} and $(C_{11} - C_{12})/2$ on going through the transition which is consistent with a reduction in the stability of the lattice. Similar behaviour has been observed near the transformation temperature (T_m) at which certain intermetallic compounds of the *A15(β-tungsten)* type transform from cubic to tetragonal lattices.

For example, Testardi and Bateman (1967) found for V_3Si that the velocity of $|110|$ shear waves of polarisation $|1\bar{1}0|$ approaches zero while the attenuation of this soft shear mode increases greatly near T_m. In the present work a temperature dependent transformation of the order-disorder type has been observed at $320^oC \pm 5^oC$ using x-ray and electrical measurements in the compound $Hg_3In_2\square Te_6$. This compound, containing 8.33% vacancies, has the least stable structure of each series, the reduction in the reduced shear moduli C_{44}/C_o and $(C_{11} - C_{12})/2C_o$ being 20% and 16% respectively and that of the reduced bulk modulus $(C_{11} + 2C_{12})/3C_o$ being 38% when compared to the reduced moduli of $HgTe$, the zero vacancy compound. A transition has also been observed in the equivalent compound $Hg_3Ga_2\square Te_6$ at a temperature between 400^oC and 500^oC. The compounds $Hg_5In_2\square Te_8$ and $Hg_5Ga_2\square Te_8$, which contain 6.25% vacancies, are more stable and retain an ordered structure even when quenched from temperatures in excess of 500^oC. Finally, it may be that the compounds at 75% In_2Te_3 (Ga_2Te_3) containing 12.5% vacancies assume the tetragonal structure because the vacancy concentration is too large for a cubic lattice to be stable.

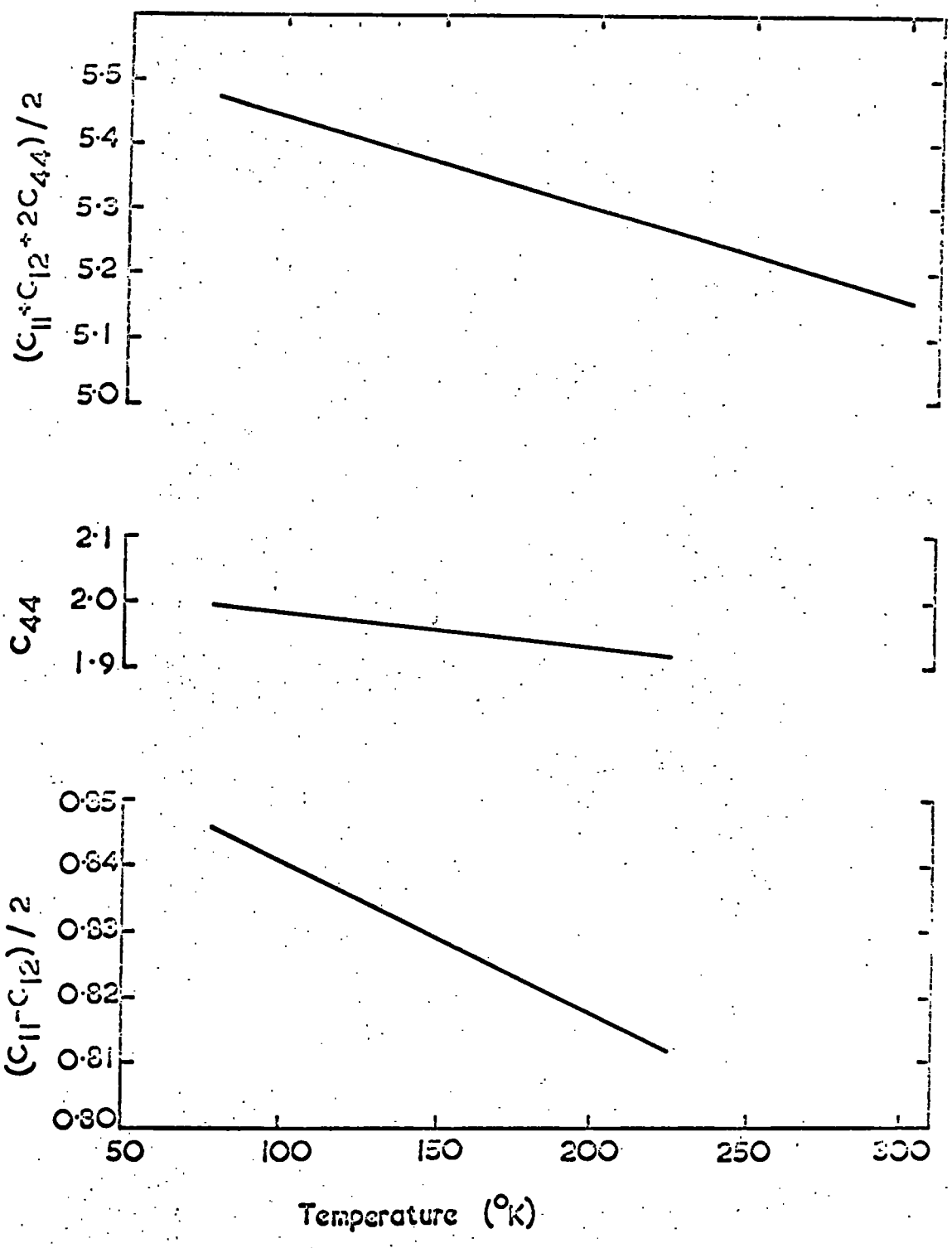

Fig. (5.1) Temperature dependence of the elastic constants of $Hg_3In_2\square Te_6$ crystals. The lines drawn are computed lines of regression from numerous data points. The units are 10^{11} dyne cm^{-2}.

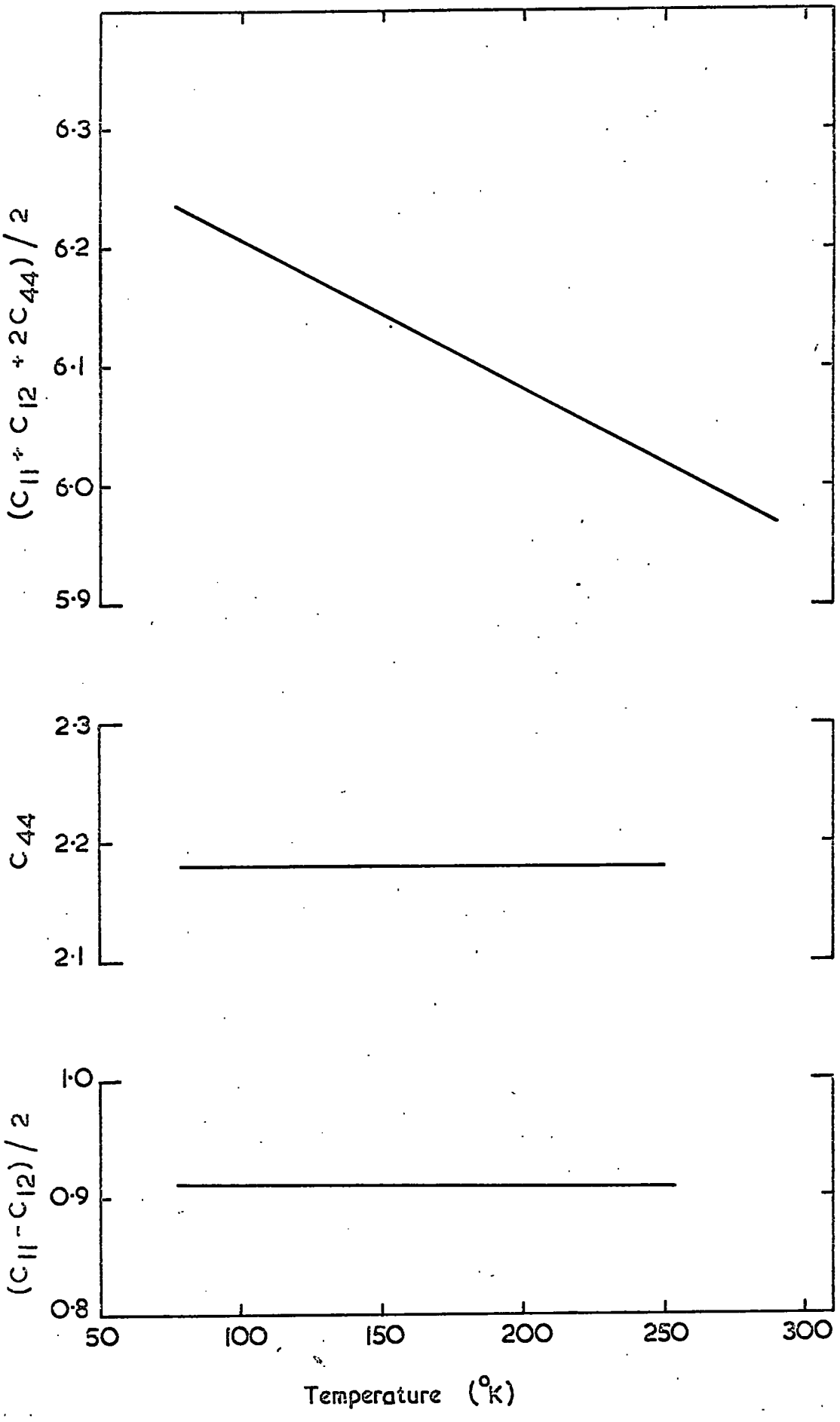

Fig. (5.2) Temperature dependence of the elastic constants of $Hg_5Ga_2\square Te_8$ crystals. The lines drawn are computed lines of regression from numerous data points. The units are 10^{11} *dyne* cm^{-2}.

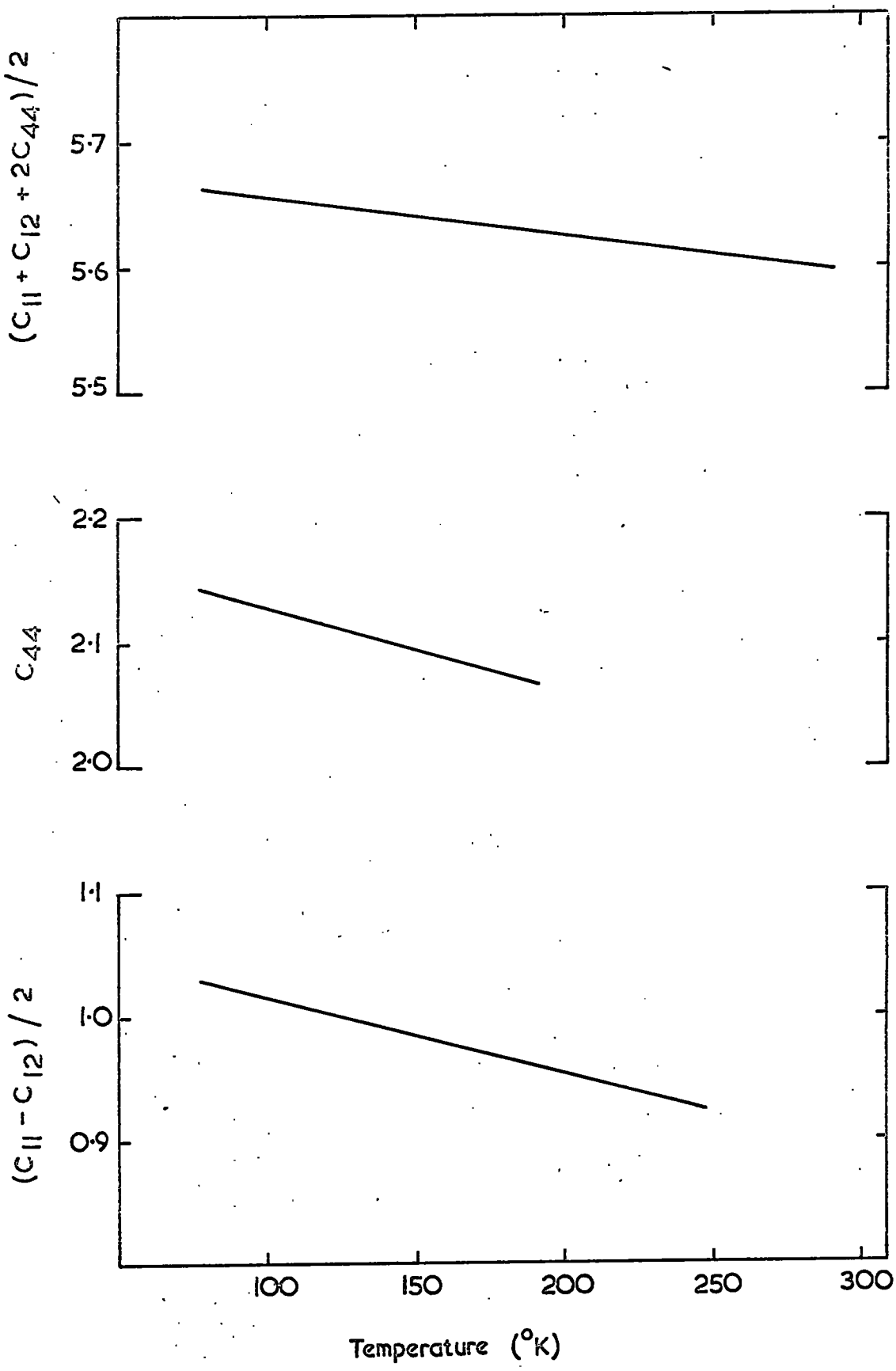

Fig. (5.3) Temperature dependence of the elastic constants of $Hg_3Ga_2\square Te_6$ crystals. The lines drawn are computed lines of regression from numerous data points. The units are 10^{11} dyne cm^{-2}.

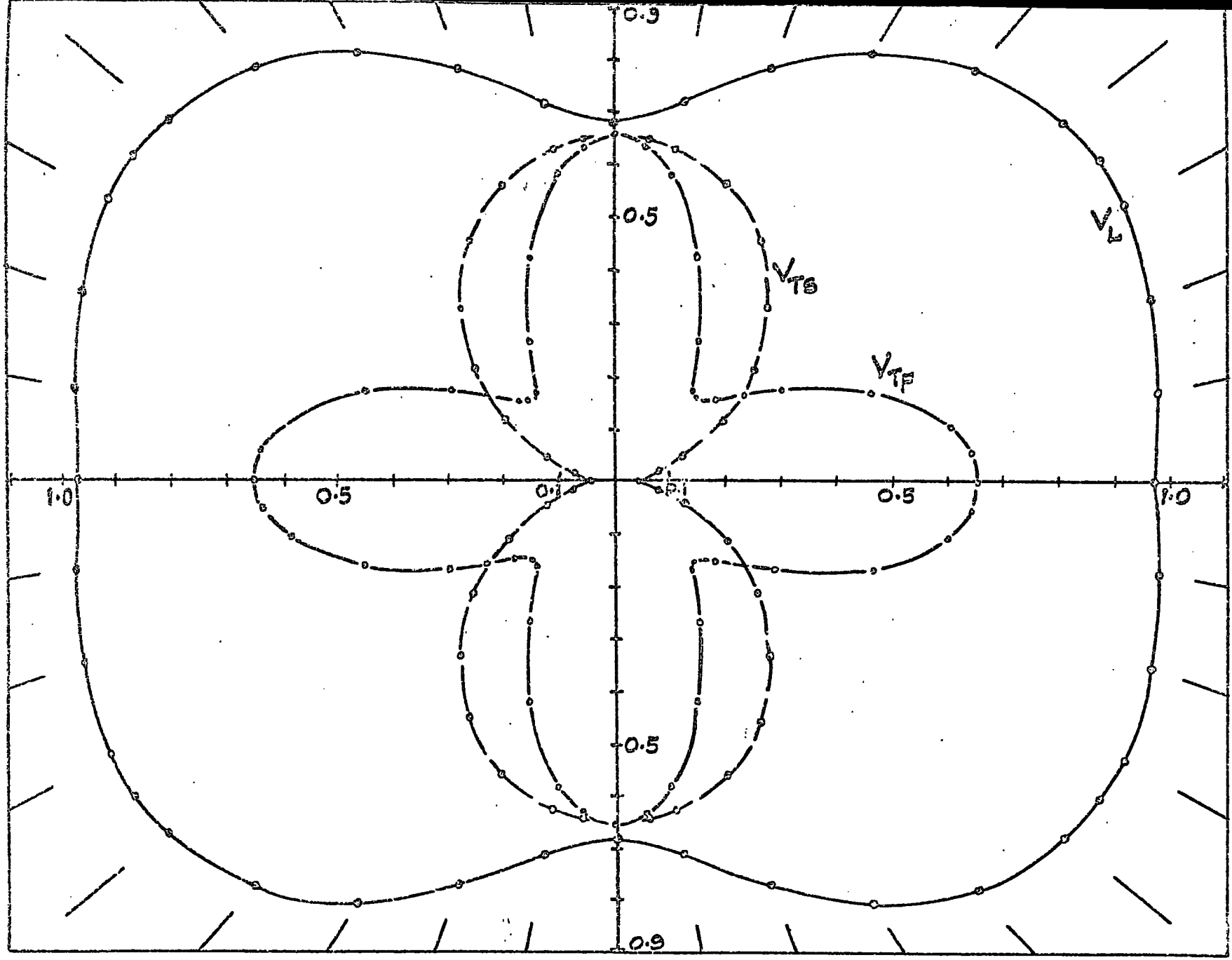

V_L 0.21 TO 0.31

V_{TF} 0.10 TO 0.20

V_{TS} 0.1 TO 0.2

Fig. (5.4)

Cross Section of the Velocity Surface

Hg Te

[110] PLANE.

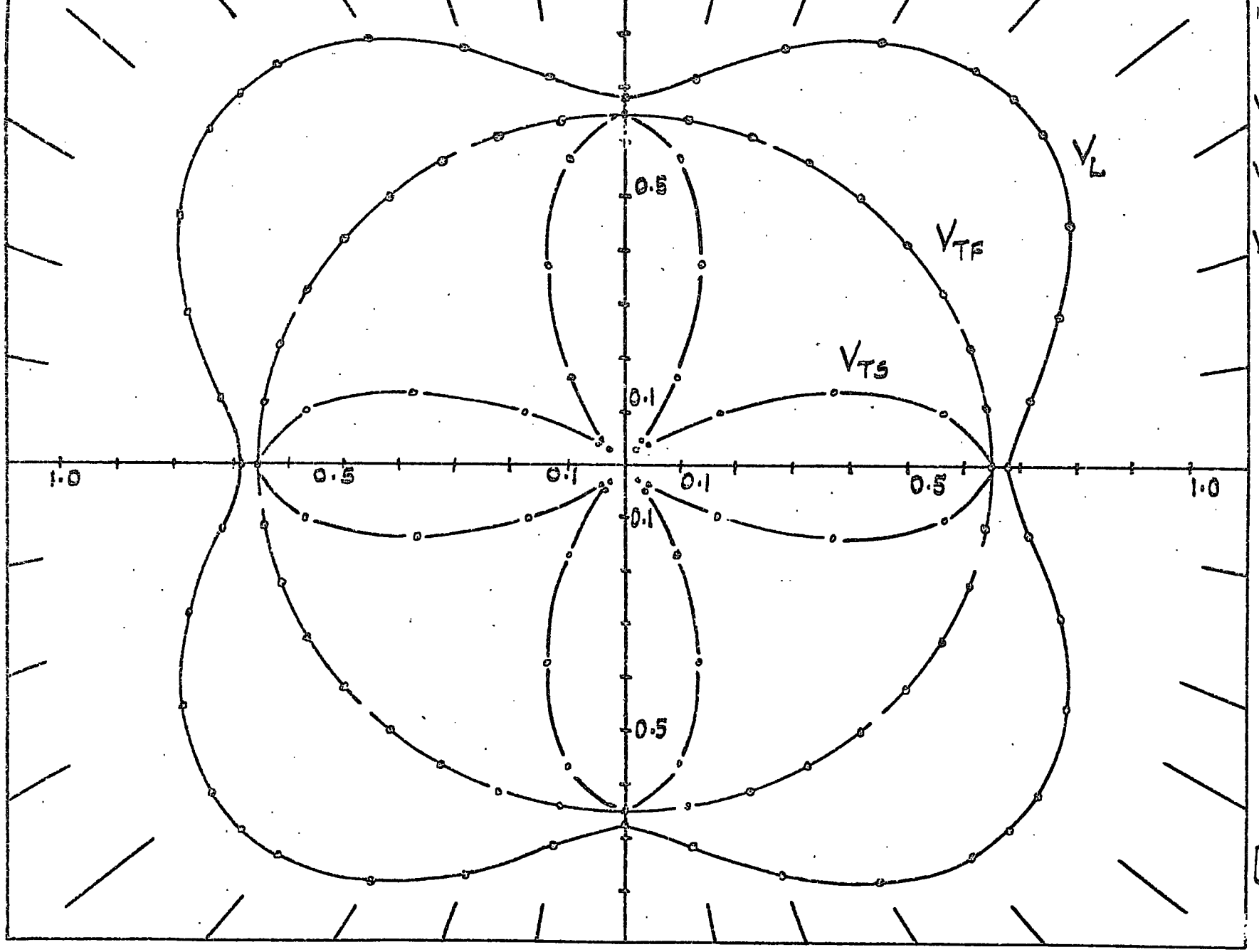

V_L 2·0 TO 3·0

V_{TF} = 1·654

V_{TS} 1·0 TO 2·0

Fig. (5.5)

Cross Section of the Velocity Surface

Hg Te

[100] PLANE.

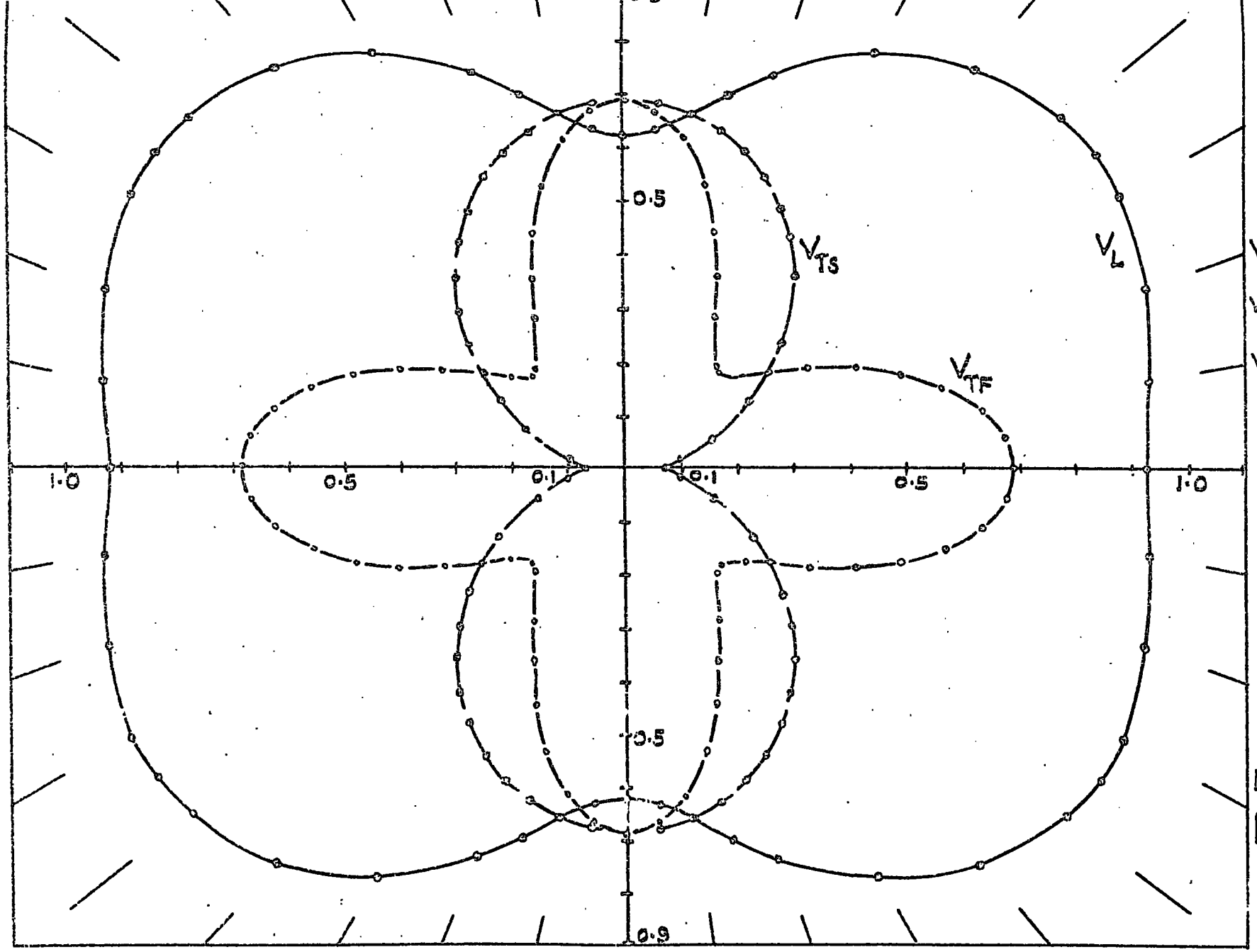

V_L = 0.2 TO 0.31

V_{TF} = 0.1 TO 0.2

V_{TS} = 0.1 TO 0.2

Fig. (5.6)

Cross Section of the Velocity Surface

$Hg_5 In_2 Te_8$
[110] PLANE.

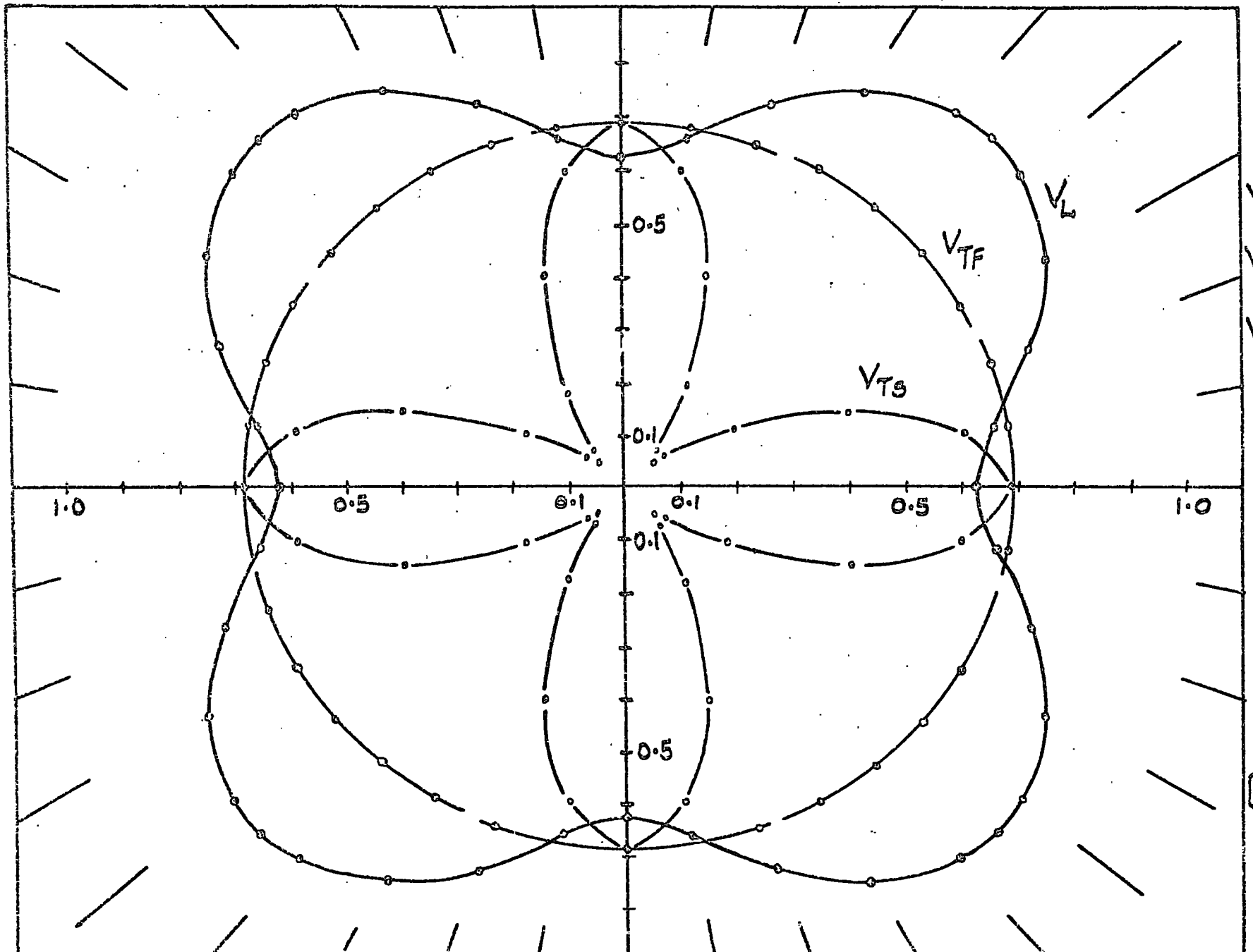

V_L 2·0 TO 3·0

$V_{TF} = 1·688$

V_{TS} 1·0 TO 2·0

Fig. (5.7)

Cross Section of the Velocity Surface

$Hg_5 In_2 Te_8$

(100) PLANE.

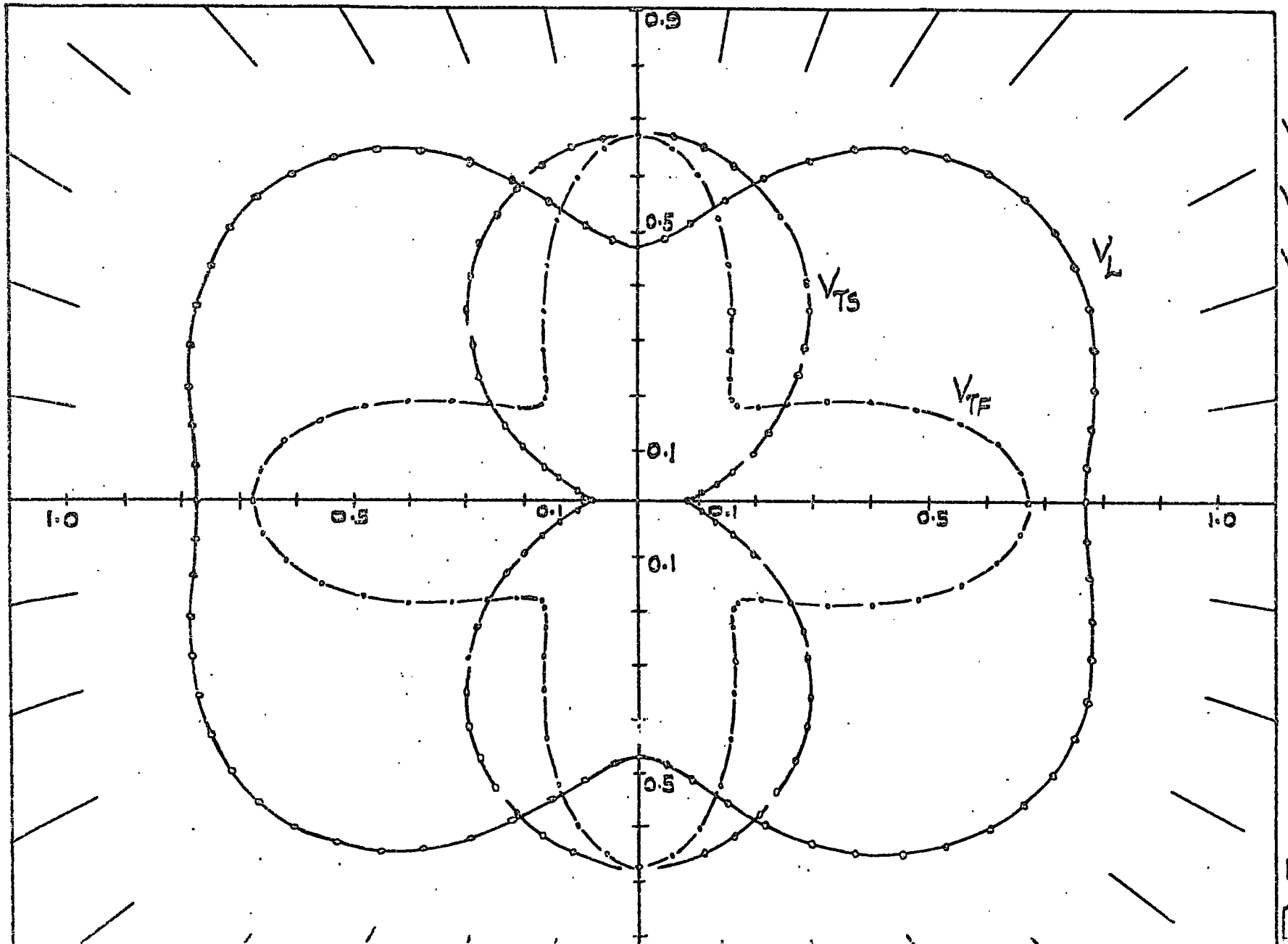

V_L = 0.2 TO 0.3

V_{TF} = 0.1 TO 0.2

V_{TS} = 0.1 TO 0.2

Fig. (5.8)

Cross Section of the Velocity Surface

$Hg_3In_2Te_6$

[110] PLANE.

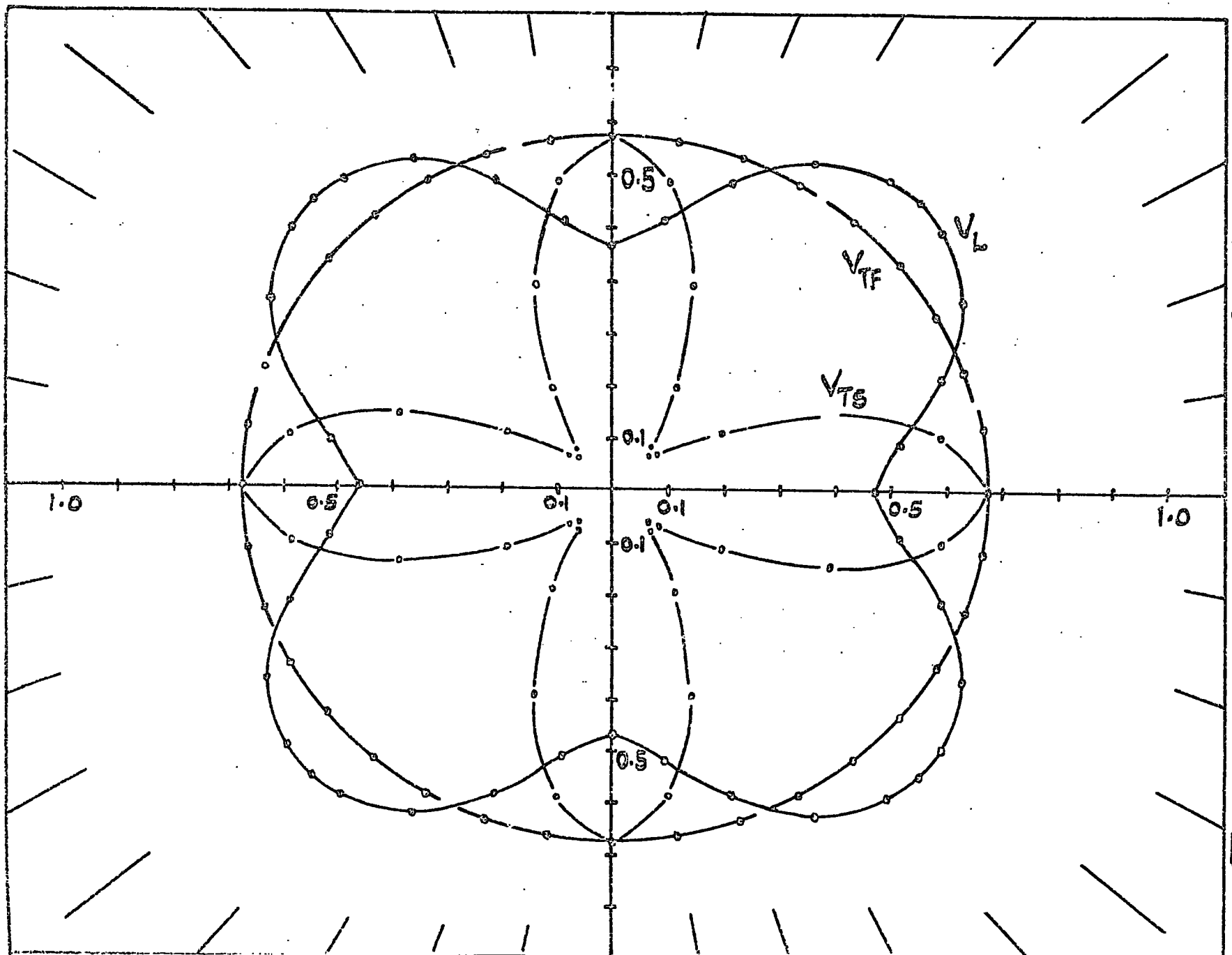

V_L 2·0 TO 3·0

V_{TF} = 1·674

V_{TS} 1·0 TO 2·0

Fig. (5.9)

Cross Section of the Velocity Surface

$Hg_3In_2Te_6$

(100) PLANE.

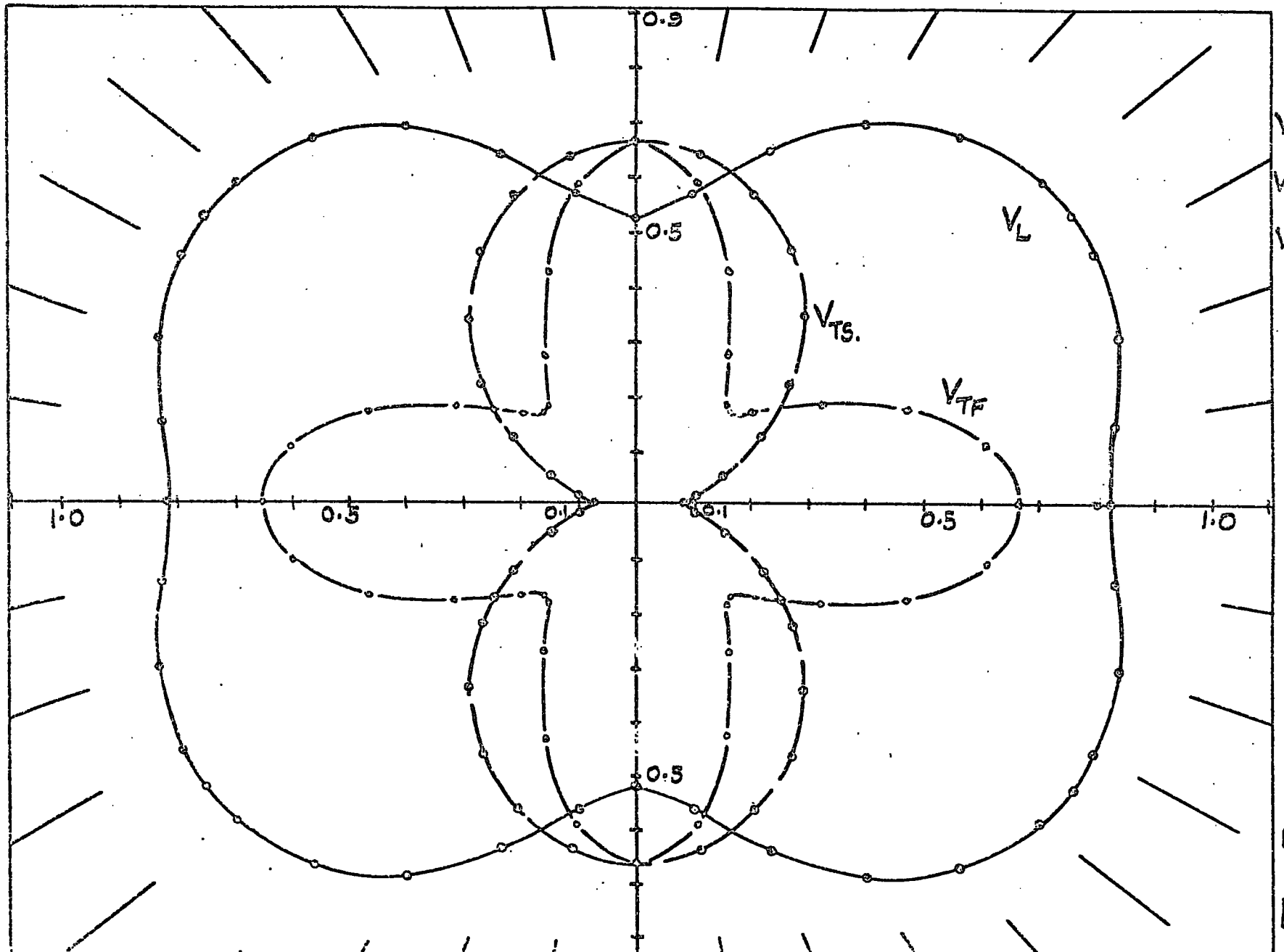

V_L 0.2 TO 0.3

V_{TF} 0.1 TO 0.2

V_{TS} 0.1 TO 0.2

Fig. (5.10)

Cross Section of the Velocity Surface

$Hg_5 Ga_2 Te_8$

[110] PLANE.

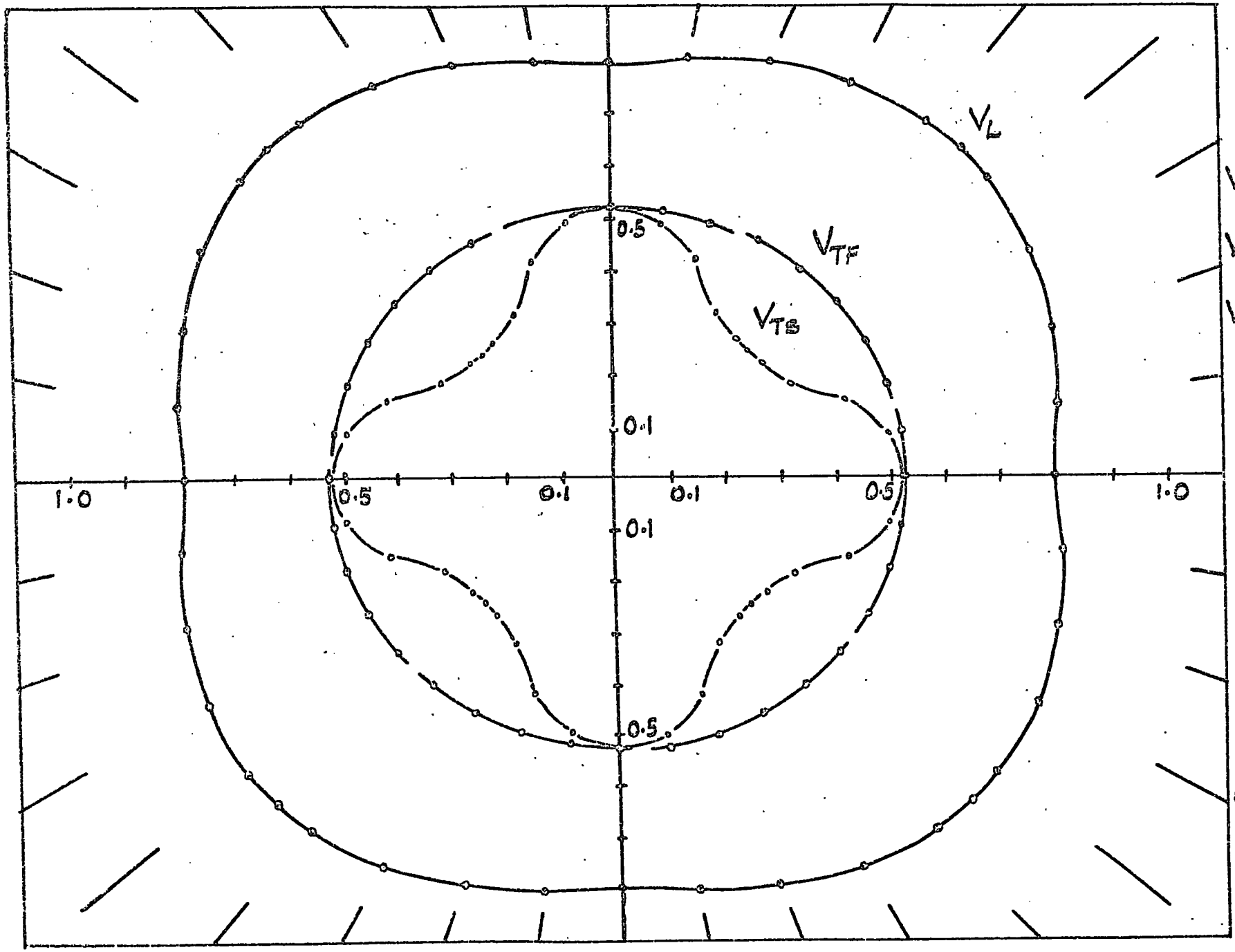

V_L 0 TO 1·0

$V_{TF} = 0.526$

V_{TS} 0 TO 1·0

Fig. (5.11)

Cross Section of the Velocity Surface

$Hg_5 Ga_2 Te_8$

(100) PLANE.

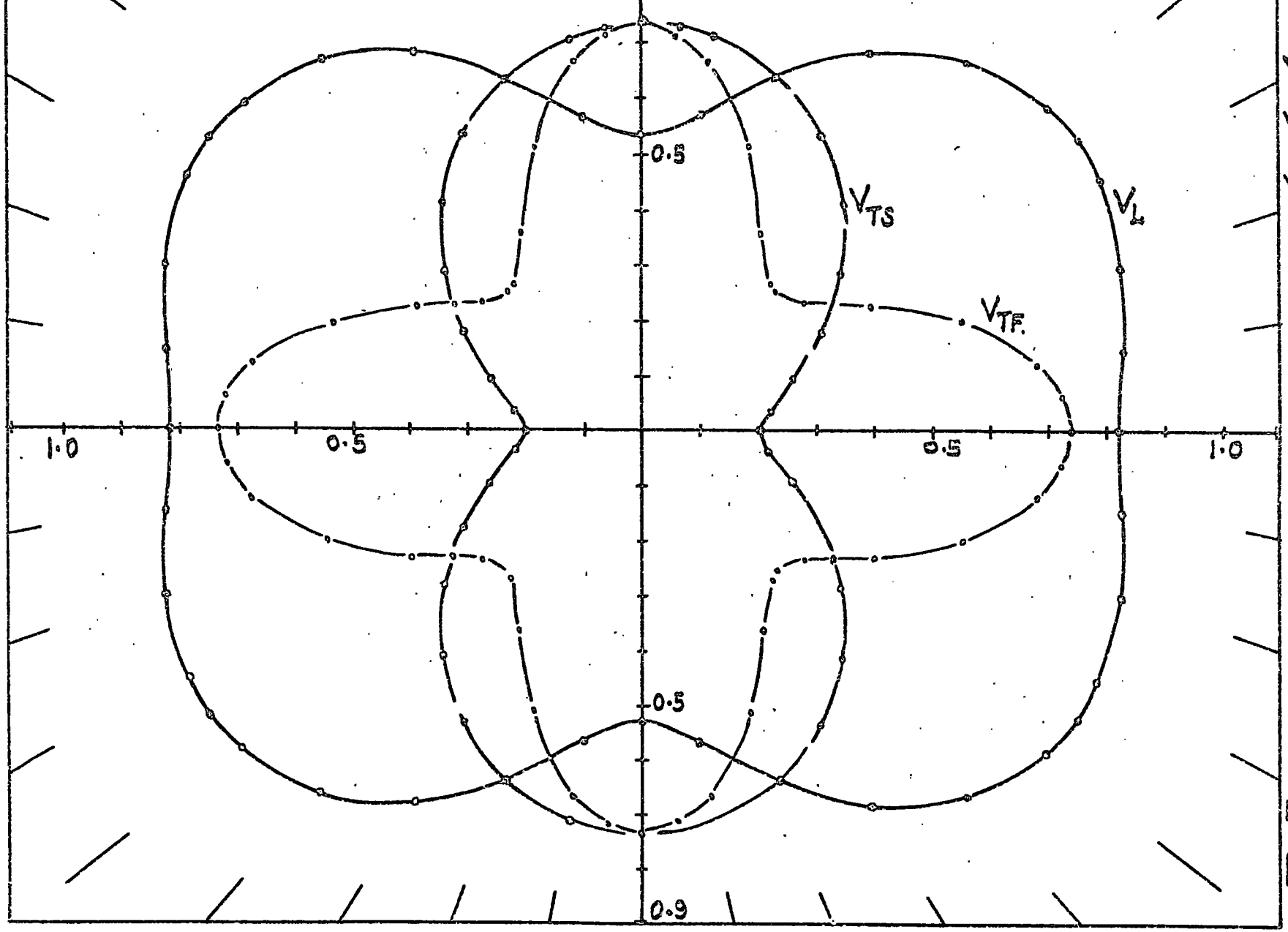

V_L = 0·2 TO 0·3

V_{TF} = 0·1 TO 0·2

V_{TS} = 0·1 TO 0·2

Fig. (5.12)

Cross Section of the Velocity Surface

$Hg_3 Ga_2 Te_6$

(110) PLANE.

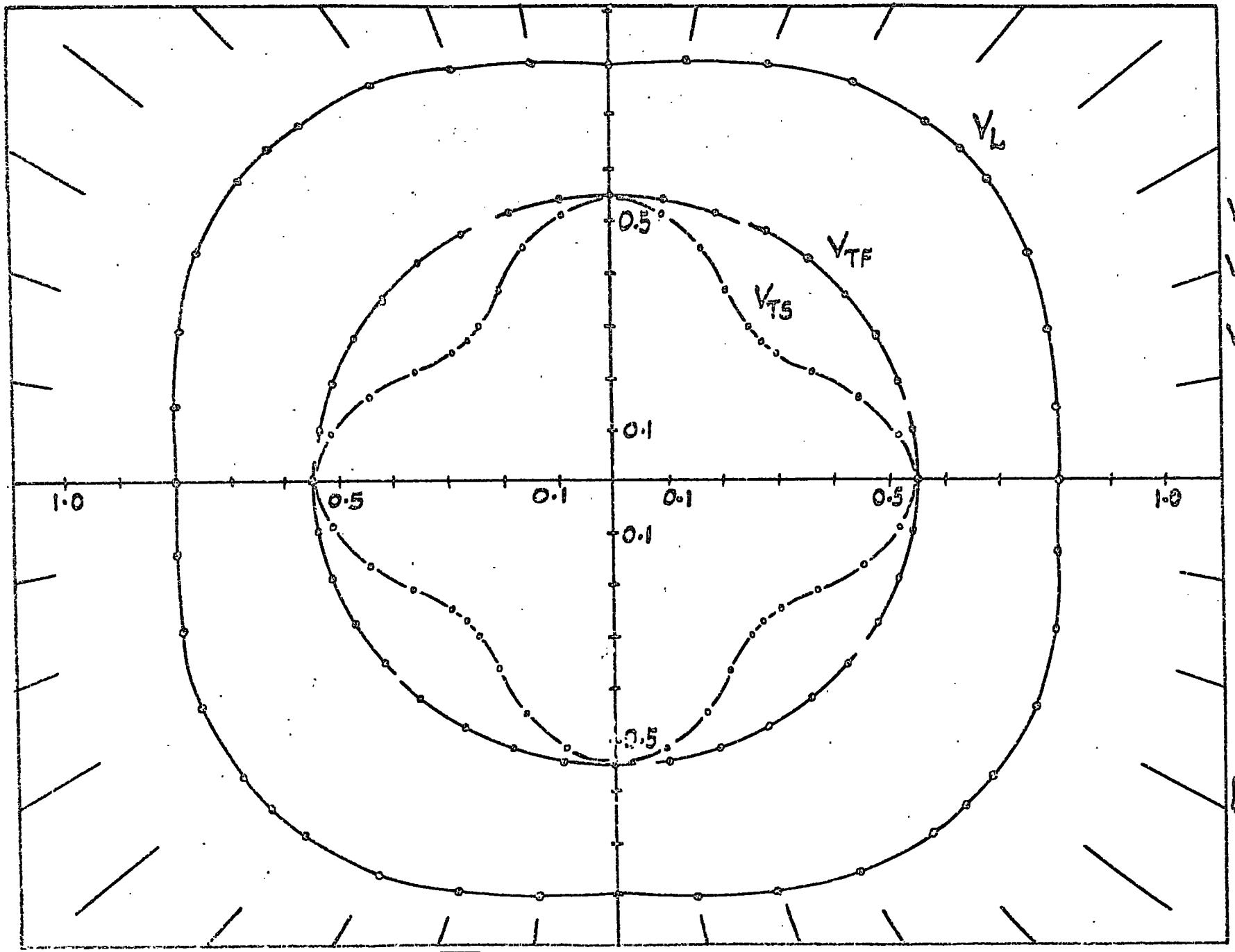

V_L 0 TO 1.0

V_{TF} = 0.5485

V_{TS} 0 TO 1.0

Fig. (5.13)

Cross Section of the Velocity Surface

$Hg_3Ga_2Te_6$

(100) PLANE.

Fig. (5.14)

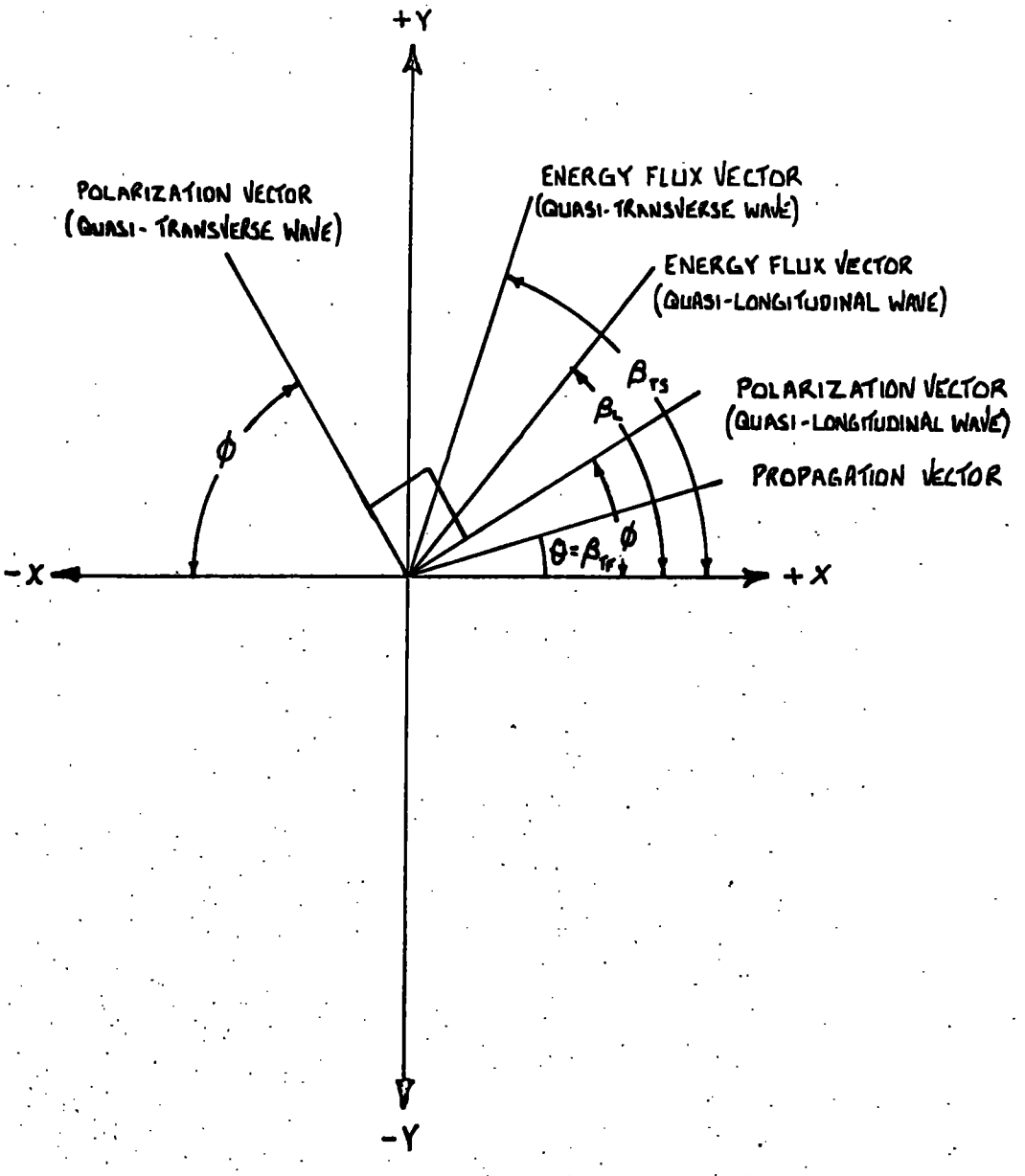

Fig. (5.15) to Fig. (5.19) give the deviation from the propagation direction in the *xy* plane of *(a)* particle displacement associated with the quasi-longitudinal wave ($\phi - \theta$), *(b)* energy flux associated with the quasi-longitudinal wave ($\beta_L - \theta$), *(c)* energy flux associated with the quasi-transverse wave ($\beta_{TS} - \theta$) and *(d)* energy flux associated with a pure transverse wave ($\beta_{TF} - \theta$ = *zero*).

Fig. (5.14) defines these angles. The particle displacement associated with the quasi-transverse wave, not shown, is ($\phi + \frac{\pi}{z} - \theta$) since the polarization vectors are orthogonal.

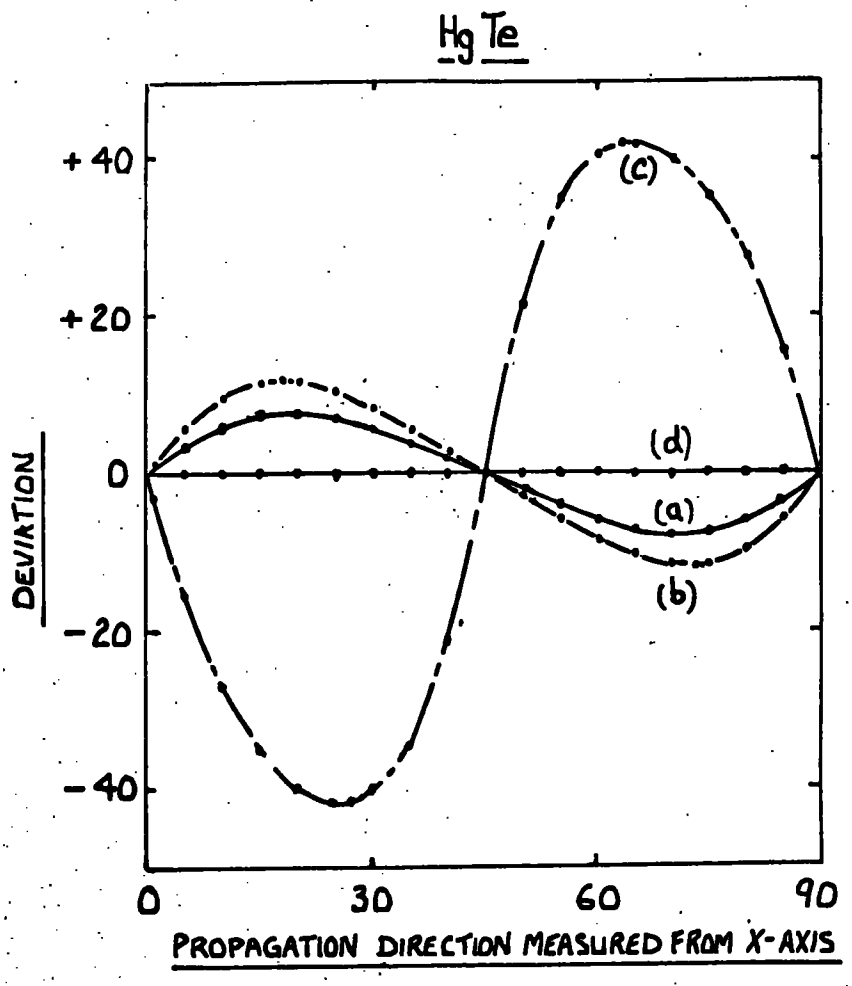

Fig. (5.15)

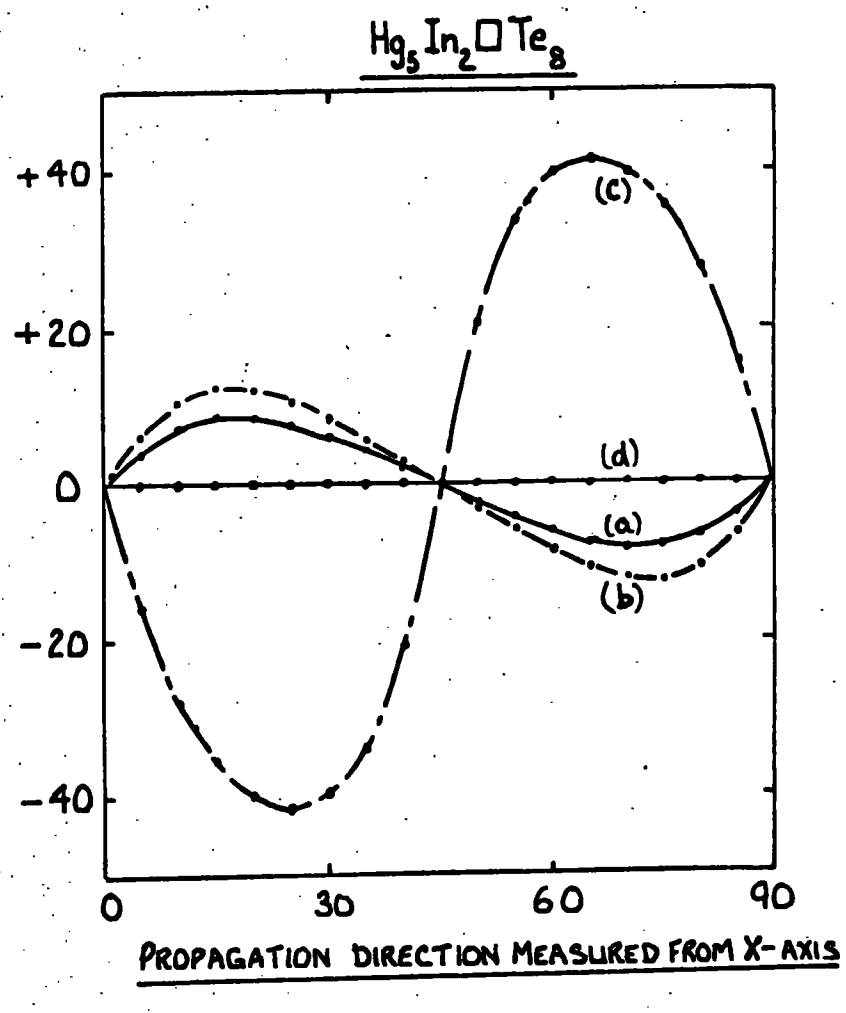

Fig. (5.16)

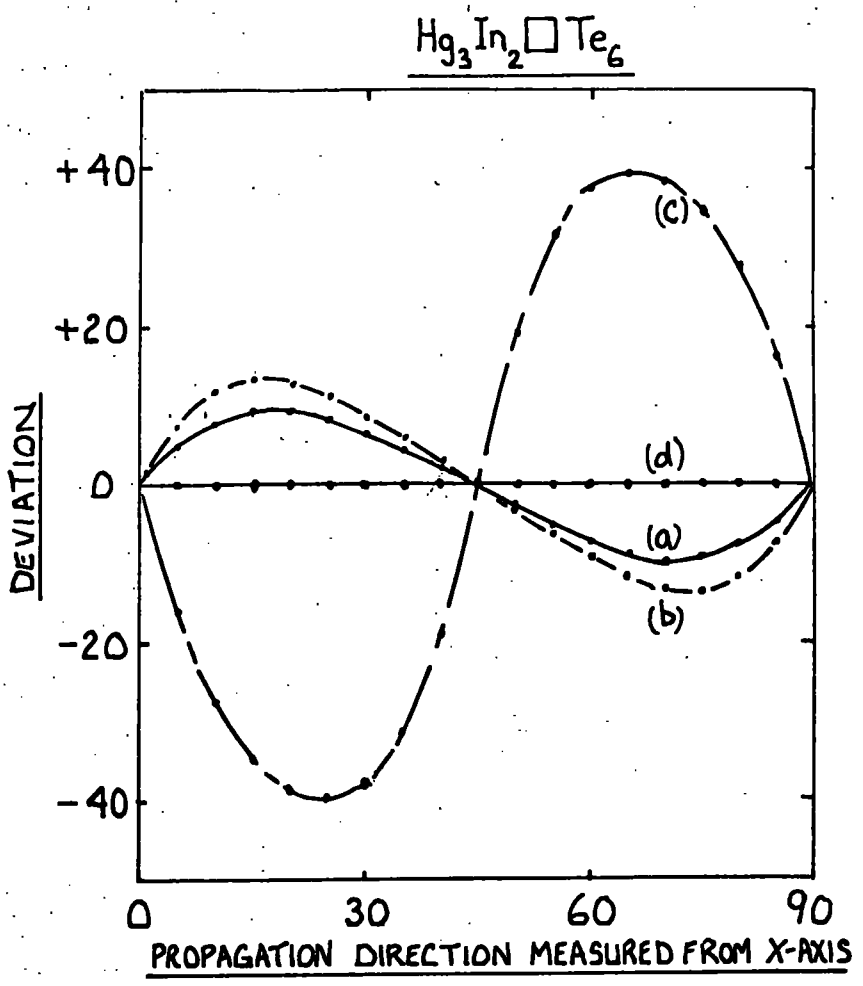

Fig. (5.17)

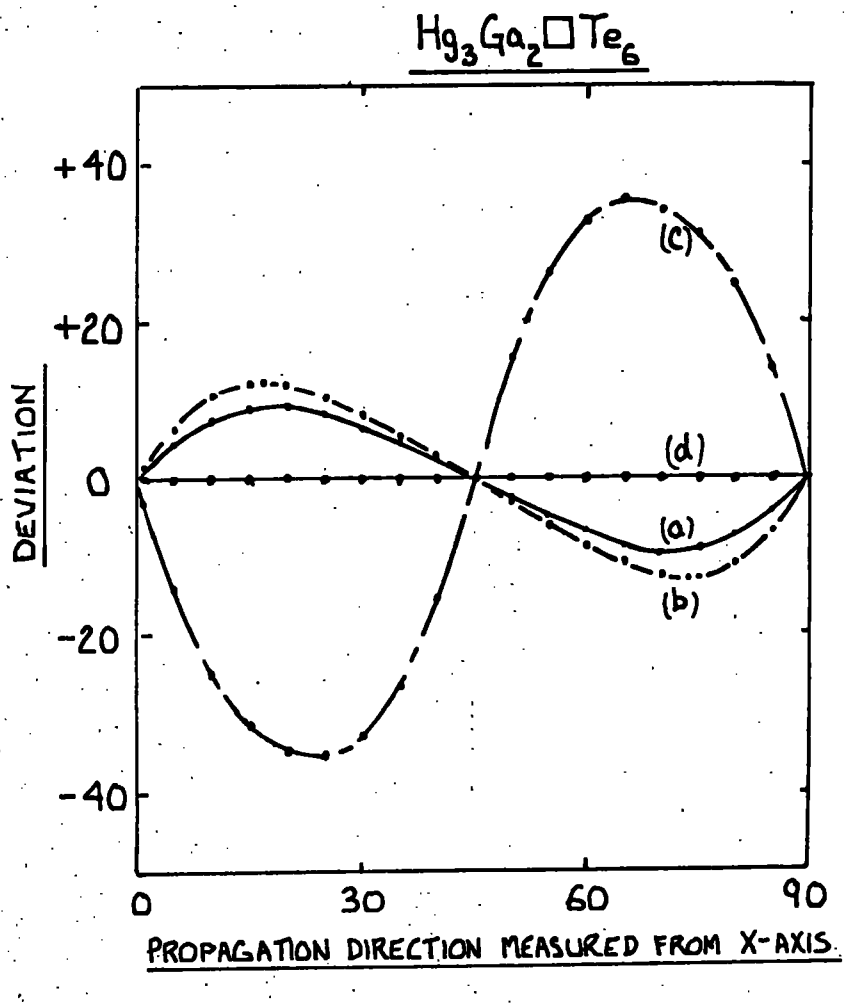

Fig. (5.18)

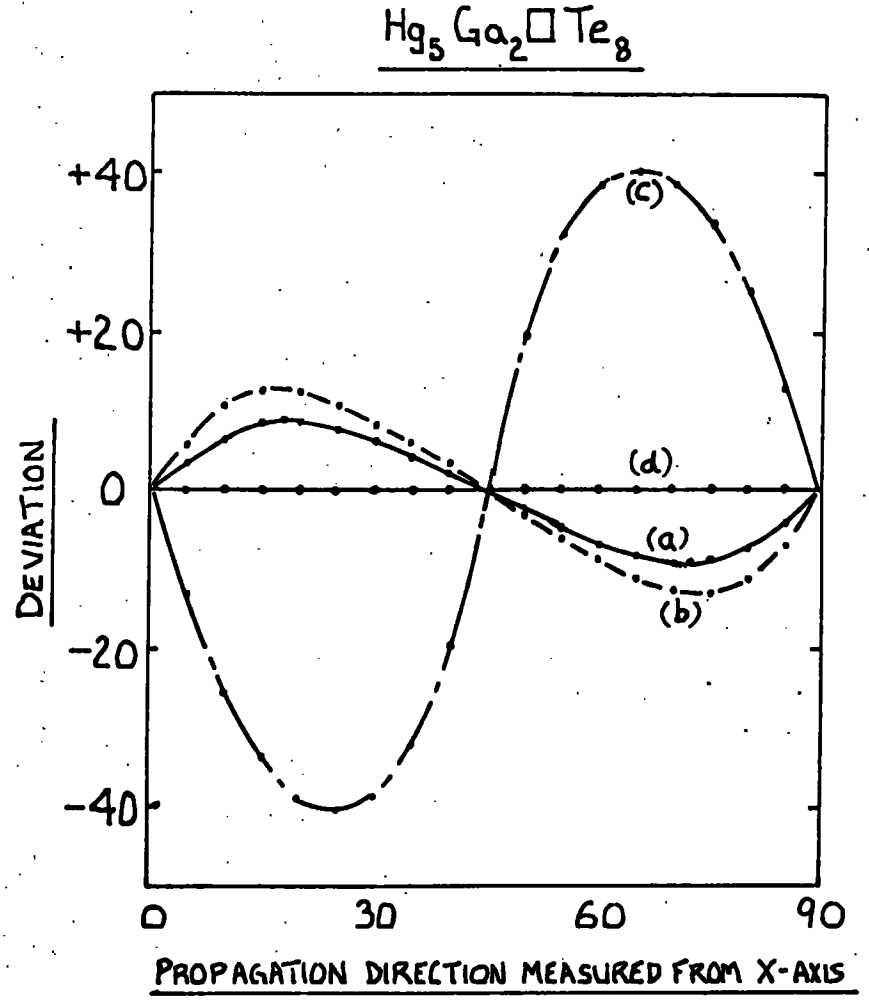
$Hg_5Ga_2\square Te_8$
+40
+20
0
-20
-40
DEVIATION
(c)
(d)
(a)
(b)
0
30
60
90
PROPAGATION DIRECTION MEASURED FROM X-AXIS

Fig. (5.19)

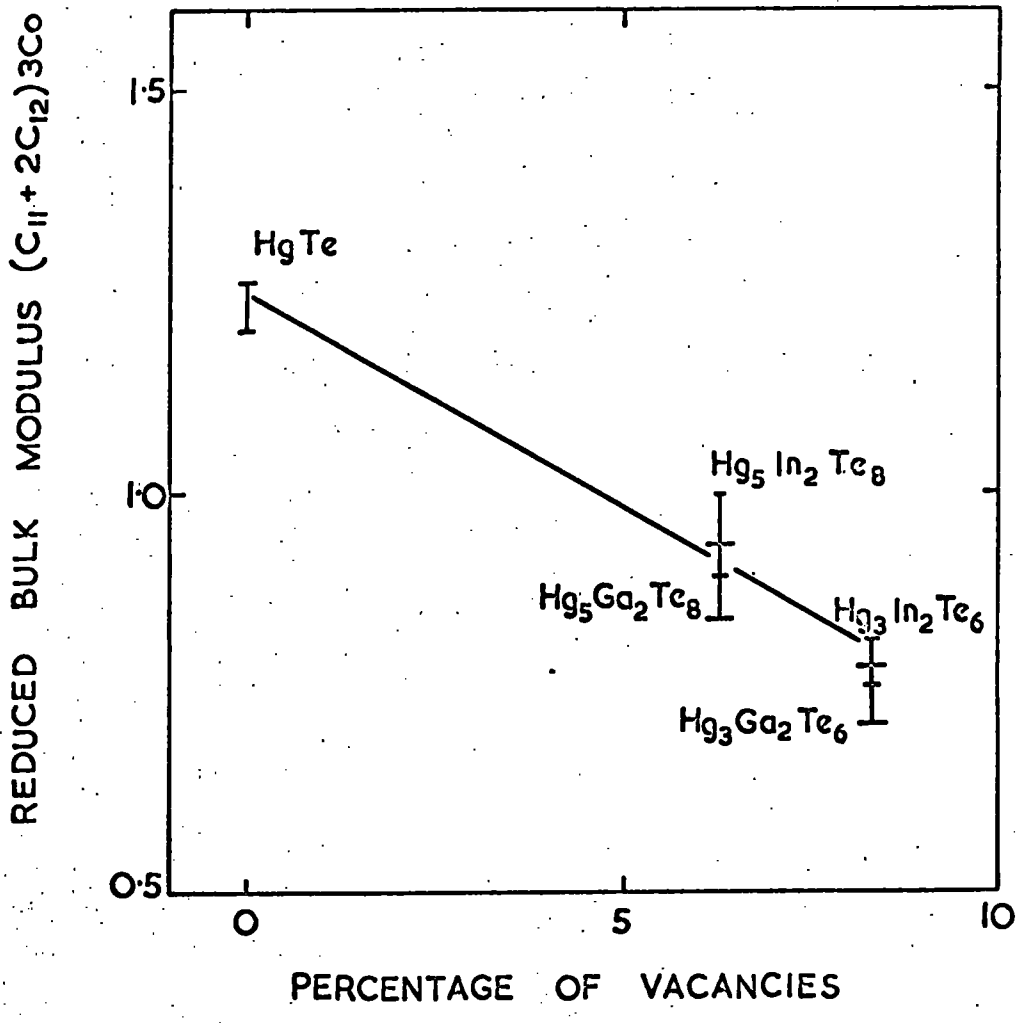

Fig. (5.20) The reduced bulk modulus plotted against the vacancy percentage in each compound.

CHAPTER 6

RESULTS DERIVED FROM THE ATTENUATION MEASUREMENTS AND DISCUSSION

6.1 ULTRASOUND DAMPING MECHANISMS

The interactions leading to damping of high frequency elastic waves propagating in solids vary widely. Not only imperfections but also elementary excitations such as phonons or electrons can contribute to the absorption. Ultrasonic attenuation measurements provide valuable information about the nature of materials, yet few details are available for compound semiconductors or semimetals. In this connection, the group of materials under study here is of interest, because they contain compounds of each of these types. Attenuation measurements have been made on the parent compound *HgTe* (Alper and Saunders 1969) but not previously on compounds of the mercury indium telluride or mercury gallium telluride series. The background attentuation in *HgTe* was found to be predominately due to losses associated with the interaction of the wave with dislocations, and for a *10MHz* longitudinal wave is in the order of *0.25dB/μsec* over a temperature range of about $150^{o}K$ above nitrogen. At room temperature it tends to be greater. Consequently, this type of absorption mechanism was expected to be the major cause of background attenuation in the vacancy compounds. In fact the attenuation is larger than in *HgTe* over the same temperature range being about *1.8db/μsec* for $Hg_3In_2\square Te_6$, *0.7db/μsec* for $Hg_5In_2\square Te_8$, *3.4dB/μsec* for $Hg_3Ga_2\square Te_6$ and *0.65db/sec* for $Hg_5Ga_2\square Te_8$. The contributions to background attenuation by other mechanisms such as deformation potential, piezoelectric coupling and the thermoelastic effect have been estimated in the parent compound *HgTe* (Alper and Saunders 1969); these results can be used to assess the order of magnitude of each contribution to the attenuation in the vacancy compounds, in the absence of appropriate data.

Deformation potential and piezoelectric coupling give rise to interactions between ultrasonic waves and charge carriers. At low megacycle frequencies $\omega (= 2\pi f)$, the attenuation of these waves in piezoelectric semiconductors (Hutson and White 1962, Lord and Truell 1966) is

$$\alpha = \left[\frac{\omega}{v_o} \right] \frac{e^2}{2cp} \left[\frac{\omega_c/\omega}{1 + \omega_c/\omega} \right] \tag{6.1}$$

This relaxation type expression is a maximum when the conductivity frequency $\omega_c (= b/p$, where b is the conductivity and p is the dielectric constant) is equal to the driving ultrasonic frequency ω. The parameter e defines the piezoelectric constant, c the elastic constant and v_o is the velocity of the wave in the absence of additional stiffness provided by piezoelectric coupling. Using the data on *HgTe* of Dickey and Mavroides (1964), the frequency at which maximum attenuation occurs is estimated to be 3×10^{12} *Hz* at an attenuation of 10^{-4} *dB/μsec* (Alper and Saunders 1969). A value which shows that even if the conductivity and the dielectric permittivity of the vacancy compounds changed by several orders of magnitude, the frequency at which the relaxation peak should occur is well beyond the range of the present experiment. Further, it would require a very large increase in the piezoelectric constant to make the attenuation caused by this effect to be significant compared with the attenuation due to dislocations. The attenuation caused by deformation potential coupling is very small for high conductivity solids (Pomerantz 1965); this is certainly the case for *HgTe* and is expected to be the same for these compounds.

Again, the order of magnitude of the attenuation due to thermo-elastic damping can be estimated for the compounds from the value

obtained for *HgTe*. When an acoustic wave propagates through a solid, the strained regions undergo a temperature change. Heat flow from the hotter, compressed to the cooler, extended regions leads to thermoelastic damping by direct conversion into thermal energy (Lücke 1956). The thermoelastic attenuation of longitudinal waves at megahertz frequencies in terms of the relative difference ($\Delta M/M_o$) between the isothermal and adiabatic moduli is

$$\alpha = \frac{8.68}{2v} \quad \frac{\Delta M}{M_o} \quad \omega^2 \tau \ dB/sec \qquad (6.2)$$

where $\omega (= 2\pi f)$ is the frequency and v is the phase velocity. τ is the relaxation time, dependent upon the propagation direction of the wave, for heat flowing from wave crest to trough and is obtainable from the thermal conductivity. Both τ and $\Delta M/M_o$ have been estimated for *HgTe* (Alper and Saunders 1969) and the attenuation using expression (6.2) at *10MHz* is typically $0.22 \times 10^{-14} dB/\mu sec$, a negligibly small value. Hence, the thermoelastic loss which is large in metals can also be considered to be negligibly small for these semiconducting compounds, which have a smaller thermal conductivity than metals.

Mechanical energy losses caused by the interaction between dislocations and high frequency alternating stress waves can be classified as resonance or relaxation losses. A satisfactory explanation for resonance is given by using the vibrating string model proposed by Koehler (1952) and developed by Granato and Lücke (1956). It is assumed that a crystal contains a network of dislocations which are strongly pinned at nodal intersections and less strongly at point defects. The attenuation which arises from the enforcedvibration of dislocation sections between these pinning points under the driving force of ultrasound waves of angular frequency ω, can be written as (Truell, Elbaum and Chick 1969);

$$\alpha = 8.68 \times 10^{-6} \left(\frac{4Gb^2}{\pi 4c} \right) \Lambda L^2 d \left(\frac{(\omega/\omega_o)^2}{\left|1 - (\frac{\omega}{\omega_o})^2\right|^2 + (\frac{\omega}{\omega_o})^2 (\frac{d}{\omega_o})^2} \right) dB/\mu sec \qquad (6.3)$$

a typical resonance expression, where the frequency response depends on the damping value $d(= B/A)$ relative to the resonant frequency ω_o. The parameters of the expression are: A the effective mass per unit length, B the damping force per unit length of dislocation per unit of velocity, c the effective tension in a bowed-out dislocation of mean length L, G the shear modulus, b the magnitude of the Burgers vector, Λ the total length of dislocation per unit volume. This type of loss forms the major background attenuation for the temperature dependent measurements made on the crystal *HgTe* and is the likely source of the background loss in $Hg_3In_2 \square Te_6$ (Figure 6.1) and in the other vacancy compounds. Expression (6.3) predicts a resonance peak and Alper and Saunders(1969)did succeed in obtaining a maximum in the attenuation on *HgTe* at about *240MHz* but only for annealed specimens. Attempts to find the frequency at which this peak occurs in each of the vacancy compounds was defeated by the very high attenuation encountered at frequencies in excess of *10MHz*.

The distinctive features in the attenuation results presented for $Hg_3In_2 \square Te_6$ (Figure 6.1) are the peaks which occur in the attenuation of the longitudinal and both shear waves within the temperature range 100^oK to 170^oK. The peaks have the characteristic features associated with a Bordoni type relaxation mechanism; an observation that is supported by the fact that both the height and the temperature position of the peak maximum were essentially independent of the ultrasonic wave amplitude. Also, the peak position was independent of prestrain which is in contrast with the dislocation damping mechanisms of the resonance

type, which suggest that an 'intrinsic' dislocation mechanism is involved which does not depend on a particular length of dislocation line. Consequently, these peaks together with the peaks obtained in the attenuation in *HgTe* (Alper and Saunders 1969), $Hg_5In_2\square Te_8$ (N. G. Pace private communication) are to be interpreted on the basis of the theory developed principally by Seeger (1955). Peaks were also observed in the compounds $Hg_5Ga_2\square Te_8$ and $Hg_3Ga_2\square Te_6$ but unfortunately at *10MHz* the positions of the maxima could not be resolved because the magnitude of the attenuation was outside the range of the measuring equipment.

6.2 THEORY OF BORDONI-TYPE RELAXATION PEAKS AND DISCUSSION

Characteristic peaks were originally observed by Bordoni (1954) in internal friction measurements on lead, aluminium, silver and copper at temperatures of the order of one third the Debye temperature and extensive studies were subsequently made by Niblett and Wilks (1957), Caswell (1958) among many others.

The dependence of the temperature at which the peaks occur on the frequency shows that the excess internal friction arises from a relaxation type of process. Further support for this interpretation is provided by the shape of the curves which are similar to that of any other relaxation process, and by the fact that damping is practically independent of strain amplitude.

For a simple relaxation process the relaxation time τ depends on the temperature T according to the Arrhenius equation

$$\tau = \tau_o \exp(W/kT) \qquad (6.4)$$

where W is the activation energy, k is Boltzmann's constant and τ_o is a constant (a temperature independent time). When measured at an angular frequency $\omega(2\pi f)$, the internal friction arising from this

process is a function of the product $\omega\tau$, and has a maximum value when $\omega\tau$ is unity. The temperature T_m at which the peak occurs can be related to the frequency by

$$f = \frac{1}{2\omega\tau_o} \exp\left(-W/kT_m\right) \tag{6.5}$$

which can also be written

$$f = f_o \exp\left(-W/kT_m\right) \tag{6.6}$$

where f_o $(= \frac{1}{2\omega\tau_o})$ is commonly called the attempt frequency. Hence, the activation energy W and the attempt frequency f_o can be found from a graph of the driving frequency f against the reciprocal $(1/T_m)$ of the peak temperature. The activation energy is obtained from the slope and the attempt frequency from the intercept. Bordoni et al (1960) found that such a graph does approximate to a straight line for the face centred cubic metals studied, giving a value of activation energy in the order of 0.1 eV. However, the situation is not so simple. If the attenuation peak arises from a process with single values of activation energy and attempt frequency, this dissipation at an angular frequency ω would be given by

$$\frac{1}{Q} = \frac{2}{Q_m} \frac{\omega/\omega_m}{\left|1 + (\omega/\omega_m)^2\right|} \tag{6.7}$$

where $\frac{1}{Q_m}$ corresponds to the maximum dissipation at a frequency

$$\omega_m = \omega_o \exp\left(-W/kT_m\right) \tag{6.8}$$

The half width of the peak given by this expression is then determined by the activation energy W and the attempt frequency ω_o. In fact the

observed peaks are frequently twice as wide as the values deduced on the basis of the activation energy obtained from the shift in the temperature of a peak maximum as a function of frequency. This indicates that the relaxation process must involve either a range of activation energies or a range of attempt frequencies or both. Hence only average values of activation energy are determined experimentally and the simple theory is only approximate. The first mechanistic theory was proposed by Mason (1955), who suggested that the relaxation process arises from the lifting of dislocations parallel to close packed directions between two adjacent Peierls (1940) minimum energy positions. A result of this theory is that the activation energy should depend strongly on the degree of cold work and the impurity content of the specimen, but this is not in agreement with the experimental observations of Niblett and Wilks (1957). These difficulties were overcome by the theory due to Seeger (1955) and Seeger, Donth and Pfaff (1957) which will now be summarised.

Consider a dislocation line lying in a position of minimum energy along a close packed direction in the glide plane Figure (6.2). In the absence of thermal fluctuations, a shear stress equal to the Peierls stress is required to displace it to the adjacent position of minimum energy. However, at finite temperatures the dislocation need not lie along a single potential energy minimum, instead it may contain kinks and bulges consisting of pairs of kinks of opposite sign. Stresses much smaller than the Peierls stress will be sufficient to move such kinks sideways, that is in a direction parallel with the dislocation line, where the potential barriers opposing motion are very small. Under the influence of such stress, new pairs of kinks of opposite sign can also form with the aid of thermal energy, and hence with a temperature-dependent frequency. If the frequency of

the applied stress is either large or small compared with the frequency ν of the thermal formation of kink pairs, no energy dissipation takes place. Only when these frequencies are comparable will there be an appreciable contribution to energy loss, and maximum dissipation occurs when the frequencies are equal.

In his original treatment Seeger (1955) assumed that the rate of formation f of kink pairs is given by an Arrhenius type equation

$$\nu = \nu_o \exp (- W/kT) \tag{6.9}$$

where W is the activation energy for the formation of kink pairs and ν_o is the attempt of frequency. ν_o was taken to be equal to the frequency of oscillation of the dislocation in the Peierls potential well;

$$\nu_o = \frac{1}{2\pi a} \left(\frac{2\sigma_p^o}{\rho} \right)^{\frac{1}{2}} \tag{6.10}$$

where σ_p^o is the Peierls stress, ρ the bulk density and a the lattice spacing. Further, Seeger assumed that W is $2H_k$, where H_k is the additional energy associated with a single kink in a dislocation line that is otherwise parallel to a close packed direction in the crystal. Then by solving the differential equation

$$E_o \frac{\partial y^2}{\partial x^2} - m \frac{dy^2}{dx^2} = b\sigma_p^o \sin \frac{2\pi y}{a} - b\sigma \tag{6.11}$$

where t is time, E_o and m are the energy and mass per unit length of a dislocation, σ is the resolved shear stress and b is the Burgers vector, for the shape of a dislocation line $y(x,t)$ lying in the x, y plane (Figure 6.2) crossing a Peierls potential barrier, Seeger obtained

$$W = 2H_k = \frac{4a}{\pi} \left(\frac{2E_o ab}{\pi} \tau_p^o \right)^{\frac{1}{2}} \tag{6.12}$$

This derivation yielded the right orders of magnitude ν_o and E_o but as it is based on the Arrhenius equation it is not very precise because kink pair formation is a collective process involving ten or hundreds of atoms. Seeger, Donth and Pfaff (1957) then gave a more rigorous treatment based on an expression for the rate of formation of kinks derived by Donth (1957) using the theory of stochastic processes. Then the frequency ν and the activation energy W for the formation of a kink pair is given as a function of temperature by

$$log\ (\frac{\nu}{z}) \ = \ F_1(r;\alpha) \tag{6.13}$$

The parameter z is given by

$$z \ = \ \frac{\pi^2}{32} \ \frac{Gb^2}{a^2v^2} \ \frac{kT_m}{m^{3/2}E_o^{1/2}} \tag{6.14}$$

where v is the velocity of sound and G is the shear modulus. This expression has been approximated (Bordoni, Nuova and Verdini 1959) as

$$z \ = \ \frac{\pi^2 k}{6b^4} \ (\frac{1}{\rho G})^{\frac{1}{2}} \ T_m \tag{6.15}$$

allowing a value to be obtained from experimental data for the temperature T_m at which the peak maximum occurs. Hence substitution of ν and z into expression (6.13) gives $F_1(r;\alpha)$. This function, given graphically by Seeger, Donth and Pfaff (1957) and reproduced here (Figure 6.3), is defined in terms of dimensionless variables r and α where

$$r \ = \ 2H_k/kT \tag{6.16}$$

and

$$\alpha \ = \ 1 \ - \ \frac{\pi}{8} \ \frac{\sigma}{\sigma_p^o} \tag{6.17}$$

Then r and hence H_k, the additional energy associated with a single kink in a dislocation otherwise parallel to a Peierls valley, can be calculated. Since, in ultrasonic experiments the strains encountered are of the order of 10^{-7}, the applied stress σ is very small compared to the Peierls stress σ_p^o and α in the above equation (6.17) is very close to unity. Knowledge of α and r leads directly to the activation energy W for kink pair formation through the relationship:

$$W = -\frac{d \log \nu}{d(1/kT)} = kTF_2(r;\alpha) \qquad (6.18)$$

using the graphical plots given for $F_2(r;\alpha)$ by Seeger, Donth and Pfaff (1957) and shown here in Figure (6.4). Further the Peierls stress σ_p^o can be obtained from

$$H_k = \frac{2}{\pi} \left(\frac{2}{5\pi} \right)^{\frac{1}{2}} Gb^3 \left(\frac{\sigma_p^o}{G} \right)^{\frac{1}{2}} \qquad (6.19)$$

This procedure has been followed for $HgTe$ (Alper and Saunders 1969) and here for $Hg_5In_2 \square Te_8$ and $Hg_3In_2 \square Te_6$, the values obtained for W, σ_p^o and H_k are collected in Table (6.1).

This theory accounts for most of the main features of a Bordoni peak. It leads to an activation energy that is an intrinsic property of the dislocations and is independent of the separation of pinning points, so that the temperature at which the peak occurs is approximately independent of both the degree of prestrain and the presence of impurities. The activation energy is also independent of the strain amplitude. The theory predicts no dependence of the peak height on frequency, which is in agreement with the available experimental evidence.

Several features of the Bordoni peak, however are not accounted for. In particular the theory leads to a peak only half as wide as that observed. Qualitatively, this difficulty can be overcome on the basis that the Peierls stress should be different for screw, edge and mixed

dislocations, with a corresponding range of activation energies for the relaxation process. The concept of a range of activation energies due to different dislocation types is also consistent with the slight shift of the peak to higher temperatures with increasing plastic deformation; the latter may be expected to affect differently, dislocations of different types. The same applies to the slight shift of the peak to lower temperatures with increasing impurity content; impurity atoms will interact differently with different types of dislocations. The theory explains the reduced peak height in annealed specimens of *HgTe*, a state which corresponds to a decrease in the dislocation density.

The problem of the main and subsidiary peaks can be resolved by attributing each peak to a direction of dislocation motion in a glide plane, the appropriate Burgers vector being the nearest neighbour distance along the slip direction, but the difficulty is to assign the correct slip plane to the appropriate peak. The experimental data can be used to resolve this problem. In zincblende lattice both $\{110\}$ and $\{111\}$ planes can be slip planes. The resolved shear stress component of the ultrasound waves differs on the two forms of slip plane, and the activation energies and the temperature T_m of the peak maximum should also be different. The experimental attenuation results are consistent with this view and, further, suggest which peaks should be assigned to a particular slip plane. Figure (6.5) illustrates the situation for the $\{110\}$ slip planes when ultrasound waves are propagated down the $|110|$ direction; the directions of forced dislocation motion are identical in the crystallographic sense, being $|1\bar{1}0|$ for both the longitudinal and transverse waves of polarisation $\underline{S}$ along the $|1\bar{1}0|$ direction. On the other hand for the transverse wave ($\underline{S}$|| $|001|$), the dislocation motion will be along the $|001|$ direction. Different activation energies are required for these two possible dislocation motions; the peak temperatures

should reflect this; they do. In the data presented for $Hg_3In_2\square Te$ (Figure 6.1) peaks occur at 164^oK in the attenuation of both the longitudinal wave and the transverse wave with $\underline{S}$ parallel to the $|1\bar{1}0|$ direction, while the peak in the other shear wave is found at 141^oK. All three types of ultrasound wave give a peak in the attenuation at 109^oK; this can be associated with dislocation motion on the $\{111\}$ slip planes for which the activation energies will be independent of atomic motion direction. Pure edge dislocations have been assumed and the appropriate Burgers vector used. The results in Table (6.1) substantiate the basic model used for the slip planes and the dislocation motion directions. For example, for the three different ultrasound wave propagations in $HgTe$, the suggested $\{111\}$ plane component in each case gives the same activation energy and Peierls stress within experimental error. Direct comparison between the three materials can now be made. There are general trends in the activation energies and Peierls stress for a given slip plane when the material is changed; both these parameters decrease through the sequence $HgTe$, $Hg_5In_2\square Te_8$ and $Hg_3In_2\square Te_6$. This trend follows the changes in elastic properties. Thus in the most easily compressed material, namely $Hg_3In_2\square Te_6$ with its high vacancy concentration, dislocation motion is most easily got under way. Vacancies which are sited regularly in an ordered lattice structure do not produce localized stress and should not pin the dislocations in the same manner as ordinary vacancies. In all three compounds the activation energies and Peierls stress are lower on the $\{111\}$ planes than on the $\{110\}$; dislocation motion is easier on the $\{111\}$ planes.

These results and the elastic constant data indicate that the elastic and anelastic properties of materials of this type can be dominated by the presence of sited vacancies.

experimental data for the peaks in the attenuation in $Hg_3In_2\square Te_6$, $Hg_5In_2\square Te_8$. With the exception of the column headed 141^oK under $Hg_3In_2\square Te_6$, peaks arising from the same type of motion are placed in horizontal rows.

	$Hg_3In_2\square Te_6$		$Hg_5In_2\square Te_8$	HgTe		
Ultrasonic Mode Propagation Direction	$L;\underline{S}//\|110\|$ $\|110\|$	$T;\underline{S}//\|1\bar{1}0\|$ $\|110\|$	$L;\underline{S}//\|110\|$ $\|110\|$	$L;\underline{S}//\|111\|$ $\|111\|$	$T;\underline{S}//\|1\bar{1}0\|$ $\|110\|$	$L;\underline{S}//\|100\|$ $\|100\|$
Frequency (v_m)	10MHz		10MHz	36MHz	10MHz	10MHz
Peak Temperature (T_m)	109^oK		175^oK	240^oK	204^oK	218^oK
Slip Plane	(111)		(111)	(111)	(111)	(111)
Shear Modulus (G)	$(C_{11} - C_{12} + C_{44})/3$		$(C_{11} - C_{12} + C_{44})/3$	$(C_{11} - C_{12} + C_{44})/3$	$(C_{11} - C_{12} + C_{44})/3$	$(C_{11} - C_{12} + C_{44})/3$
Burgers' Vector (b)	$a_o/\sqrt{2}$		$a_o/\sqrt{2}$	$a_o/\sqrt{2}$	$a_o/\sqrt{2}$	$a_o/\sqrt{2}$
$F_1(r,\alpha)$	-6.51		-6.93	-5.82	-6.96	-7.00
r	3.90		4.15	3.50	4.17	-4.10
$F_2(r,\alpha)$	8.60		9.12	7.34	9.20	8.83
$H_K(eV)$	0.018		0.031	0.036	0.037	0.038
W (eV)	0.081		0.14	0.15	0.16	0.16
$(\sigma_p^o/G) \times 10^4$	1.4		3.7	4.2	4.8	4.8
$(\sigma_p^o) \times 10^7$	1.7		4.7	5.2	6.0	6.0
Peak Temperature (T_m)	164^oK	141^oK	223^oK			260^oK
Slip Plane	(110)	(110)	(110)			(110)
Shear Modulus (G)	$(C_{11} - C_{12})/2$	C_{44}	$(C_{11} - C_{12})/2$			$(C_{11} - C_{12})/2$
Burgers' Vector (b)	$a_o/\sqrt{2}$	$a_o/\sqrt{2}$	$a_o/\sqrt{2}$			$a_o/\sqrt{2}$
$F_1(r,\alpha)$	-7.10	-5.14	-7.38			-7.33
r	4.25	3.10	4.42			4.40
$F_2(r,\alpha)$	9.4	6.6	9.81			9.78
$H_K(eV)$	0.030	0.018	0.042			0.049
W (eV)	0.133	0.081	0.19			0.22
$(\sigma_p^o/G) \times 10^4$	7.9	0.28	15.2			16.0
$(\sigma_p^o) \times 10^7$	6.7	0.56	12.8			15.0

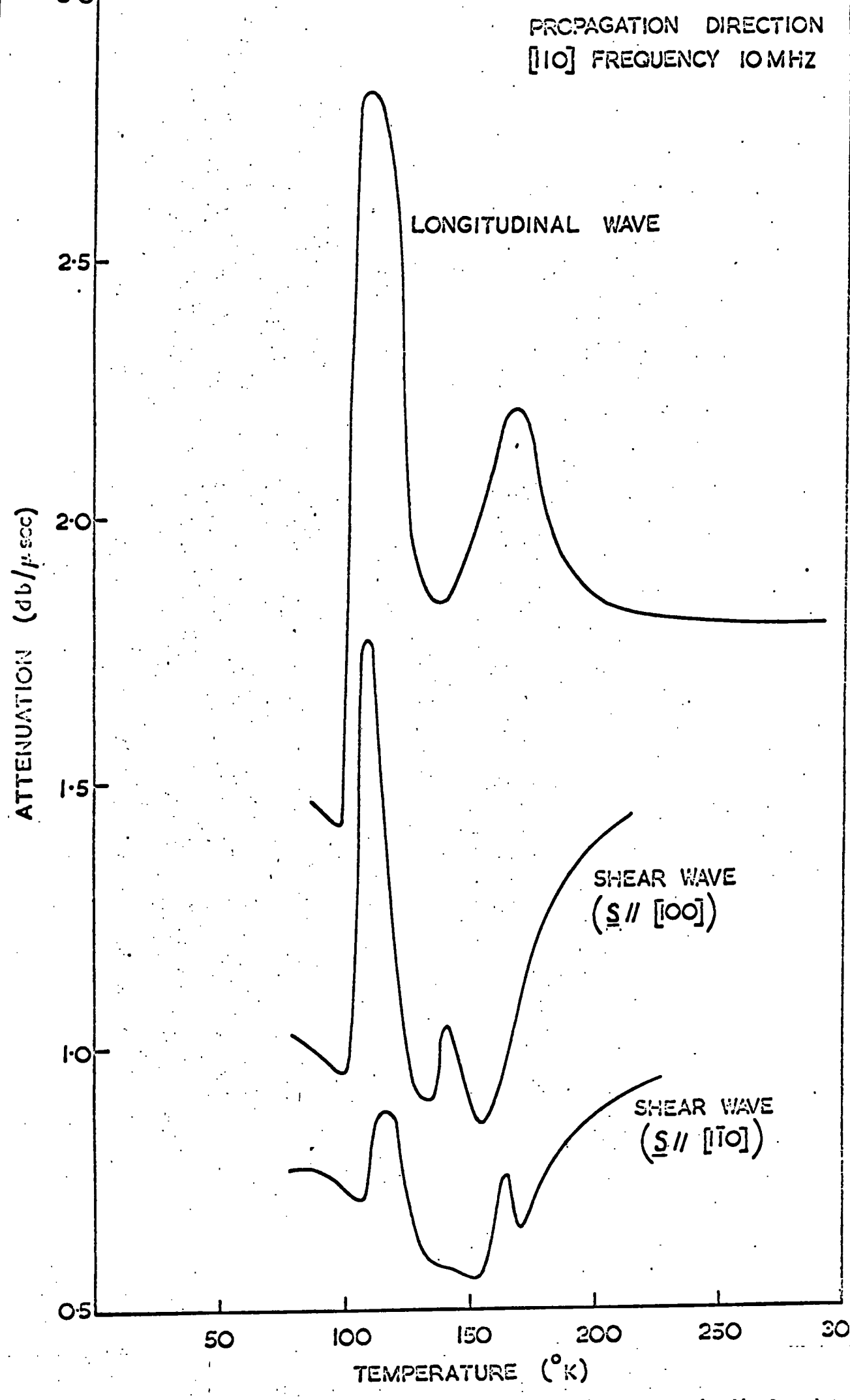

Fig. (6.1) The temperature dependences of the attenuation of longitudinal and transverse ultrasonic waves (frequency *10MHz*) propagated down the $|110|$ direction in $Hg_3In_2\square Te_6$. Some substructure was observed in the *109°K* peak found for attenuation of the longitudinal wave, the envelope only is shown here.

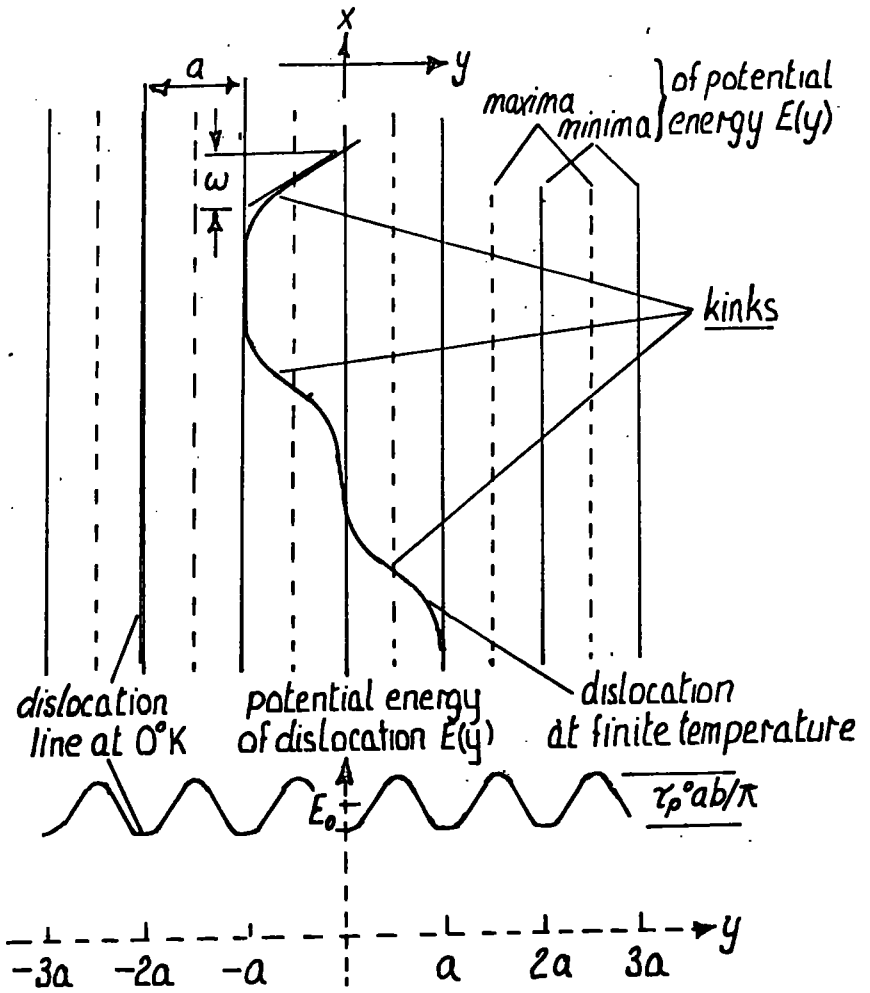

Fig. (6.2) Potential energy of a dislocation line due to Peierls stress σ_p^o (Seeger et al 1957)

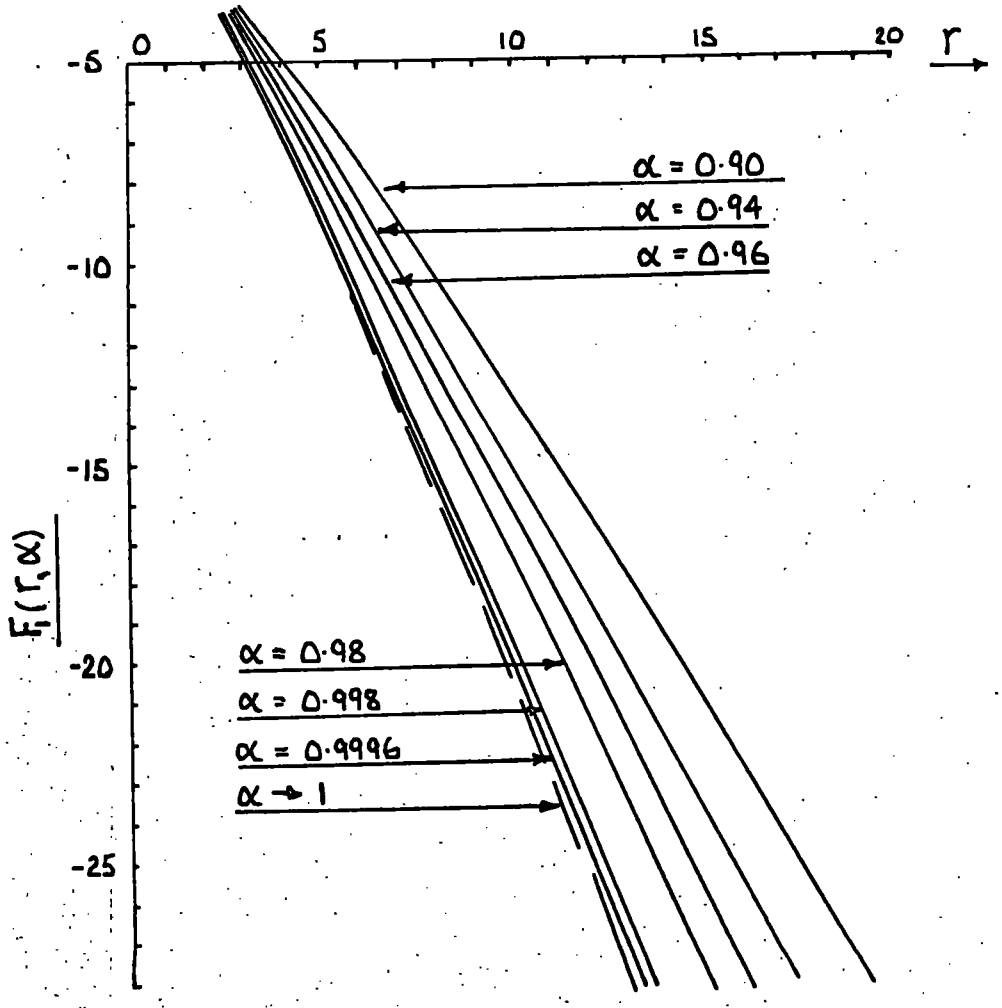

Fig. (6.3) The function $F_1(r,\alpha)$ given by Seeger et al (1957)

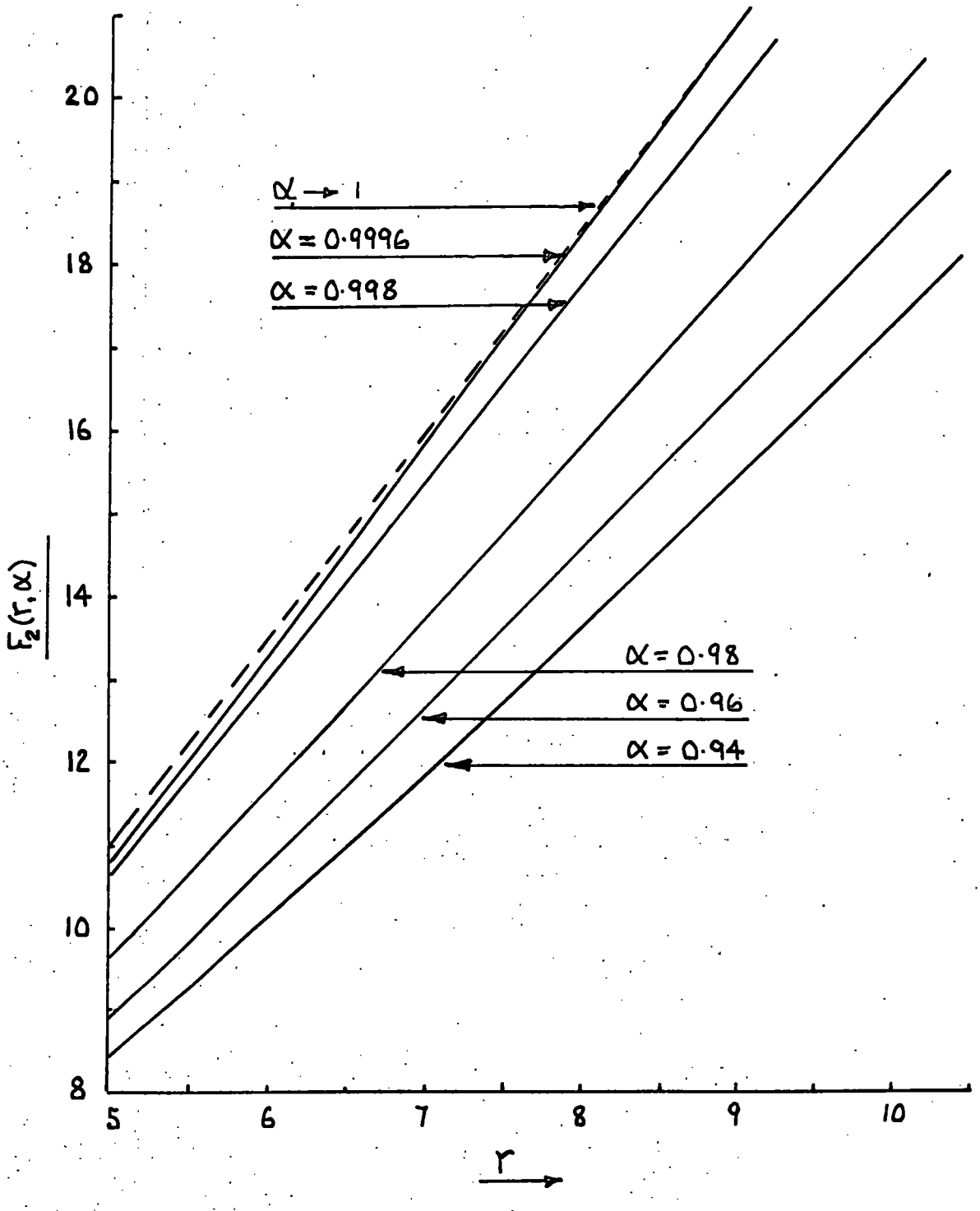

Fig. (6.4) The function $F_2(r,\alpha)$ given by Seeger et al (1957)

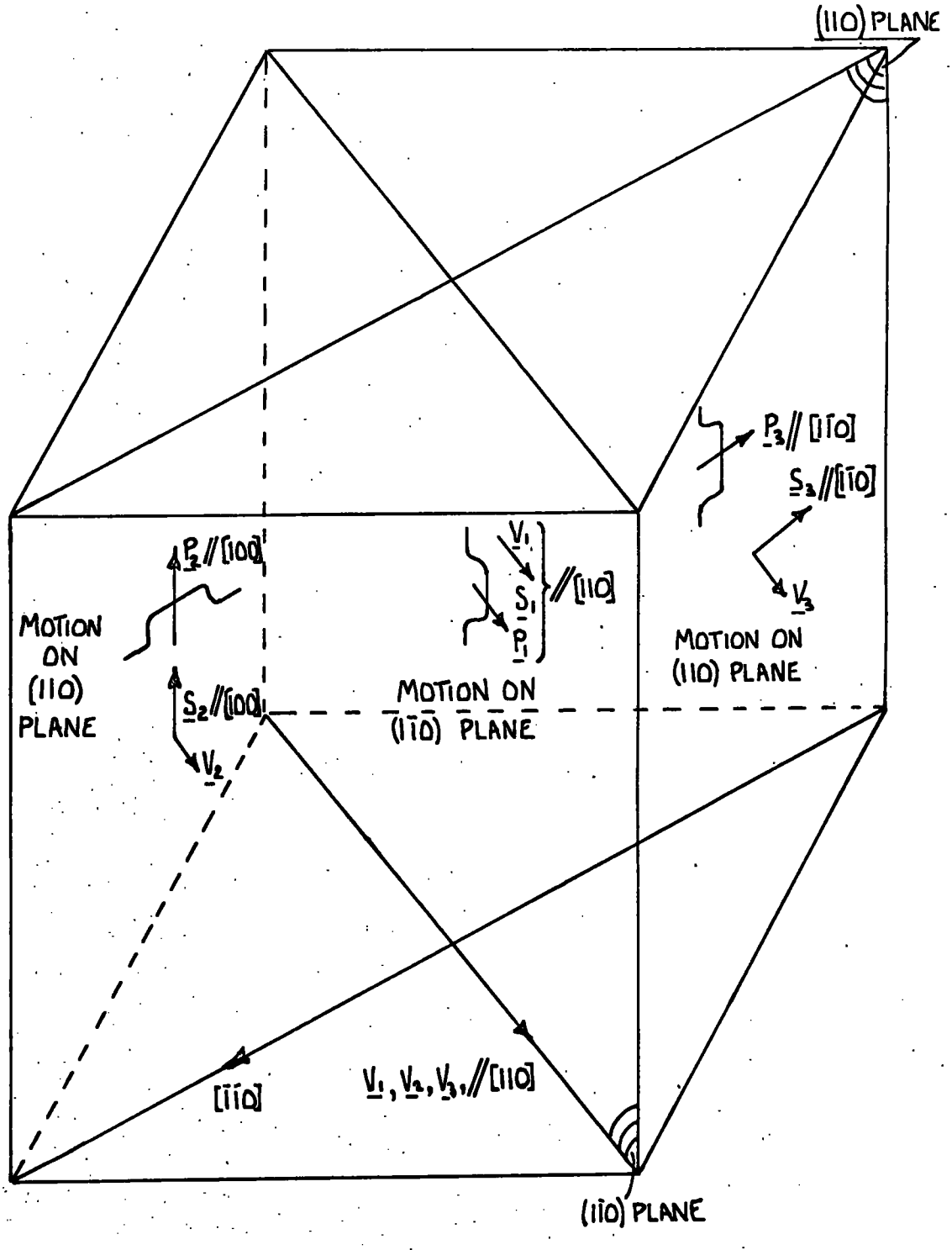

Fig. (6.5) To show forced dislocation motion on the {110} planes $\underline{V}_i$ and $\underline{S}_i$ are the ultrasonic wave velocities and polarisation vectors respectively as given on page (46). The vectors P_i are the directions along which the dislocations are forced and the bowed lines represent the kinked dislocation lines. The Burgers vectors b_i for edge dislocations are $a_o/\sqrt{2}$ for P_1 and P_3 and a_o for P_2, and vice-versa for pure screw dislocations.

REFERENCES

Alper, T. and Saunders, G. A. (1967) J.Phys. Chem.Solids, 28, 1637

Alper, T., Pace, N.G. and Saunders, G.A. (1968) Brit. J. Appl. Phys. (J.Phys.D), 1, 1079

Alper, T. (1968) Ph.D. Thesis, University of Durham

Alper, T. and Saunders, G. A. (1969) Phil.Mag. 20, 225

Alers, G. A. (1965) Physical Acoustics, Vol. III B (Academic Press, New York)

Born, M. and Huang, K. (1954), Dynamical Theory of Crystal Lattices (Clarendon Press, Oxford)

Born, M. and Misra, R. D. (1940), Camb.Phil.Soc. 36, 160

Bobylev, B. A. and Kravchenko, A. F. (1967) Sov.Phys. Acoustics (English Trans.) 12, 315

Blackman, M. (1935), Proc. R.Soc. A148, 384

Bhagavantum, S. (1955), Proc. Indium Acad.Sc., 41, 72

Bordoni, P. G. (1954), J. Acoustic Soc. Am. 26, 495

Bordoni, P. G., Nuova, M. and Verdini, L., (1959) Nuovo Cim. 14, 273 and (1960) Nuovo Cim. 16, 373

Caswell, H. L. (1958) J.Appl. Phys., 29, 1210

Dahake, S. L. (1967) Ph.D. Thesis, University of Durham

Dahake, S. L. (1967) Brit. J. Appl.Phys. 18, 1340

Debye, P. P. (1912), Ann.Physik Lpz. (4) 39, 789

Dickey, D. H. and Mavroides, J. G. (1964), Solid St. Comm. 2, 213.

Donth, H. (1957), Z.Physik 149, 111

Fumi, F. G. (1952) Acta. Cryst., 5, 44 and 5, 691

Fieschi, R. and Fumi, F. G. (1953), Nuovo Cim., 10, 865

Granato, A. and Lucke, K. (1956), J. Appl. Phys. 27, 583

Granato, A. and Truell, R. (1956), J. Appl. Phy. 27, 1219

Gusson, D. B., Jennings, I. C., Parrott, J. E. and Penn, A. W. (1960), Proc. Int. Conf. Semiconductor Phys., Prague (Academic Press, New York), 1032

Hahn, H. and Klingler, W. (1949), Z.anorg.allg. Chem. 259, 135 and 260, 97

Hahn, H. (1952), Angew. Chem. 64, 203

Hahn, H. Frank, G., Klinger, W, Störger, A. D. and Störger, G. (1955), Z.anorg.allg. Chem. 279, 241

Hutson, A. R. and White, D. L. (1962), J. Appl. Phys. 33, 40

Huntington, H. B. (1958), Solid State Physics, Vol. 7. (Academic Press, New York)

Isenberg, I., Russel, B.R., and Greene, R. F. (1957), Rev. Sc. Instrum, 34, 512

Keyes, R. W. (1962), J. Appl. Phys., 33, 3371

Kolsky, H. (1953), Stress Waves in Solids, (Clarendon Press, Oxford)

Koehler, J. S. (1952), Imperfections in Nearly Perfect Crystals (Wiley, New York)

Lyddane, R. H., Sachs, R. G. and Teller, E. (1941) Phys. Rev., 59, 605

Lipson, A. H. (1950), Prog. in Metal Phys., 2, 1

Lewis, J. E. and Wright, D. A. (1966), Brit. J. Appl. Phys., 17, 783

Lewis, J. E. (1965), Ph.D. Thesis, University of Durham

Lord, A. E., and Truell, R. (1966), J. Appl. Phys., 37, 4631

Lücke, K. (1956), J. Appl. Phys. 27, 1433

Leibfried, G. (1955), Handbuch der Physik, Vol. 7, (Springer, Berlin)

Love, A. E. H., (1944), Mathematical Theory of Elasticity, (Dover, New York)

Lawson, W. D., Nielson, S., Putley, E. H. and Roberts (1959) J. Phys. Chem. Solids. 9, 325

Musgrave, M. J. P., (1954), Proc. R. Soc., A226, 339

Musgrave, M. J. P., (1970), Crystal Acoustics, (Holden-Day, San Francisco)

McSkimin, H. J. (1964), Physical Acoustics, Vol. 1A. (Academic Press, New York)

McSkimin, H. J. and Thomas, D. G. (1962), J. Appl. Phys., 33, 56

McCartney, H. (1971), Private Communication

Mooser, E. and Pearson, W. B. (1959), Acta-Cryst., 12, 1015

Mason, W. P. (1955), Phys. Rev. 98, 1136

Mason, W. P. (1955), J. Acoustic Soc. Am., 27, 643

Mason, W. P. (1955), Bell System Tech. J. 34, 903

Nelson, J. B. and Riley, D. F. (1945), Proc. Phys. Soc., 57, 160

Niblett, D. H. and Wilks, J. (1956), Conf. Phys. Basses Temp. Paris, 1955, p.484, Instit. Intern. du Froid, Paris

Niblett, D. H. and Wilks, J. (1957), Phil. Mag., 2, 1427

Novotny, D. B. and Smith, J. F. (1965), Acta Metall., 13, 881

Nye, J. F. (1957), Physical Properties of Crystals and their representation by Tensors and Matrices (Clarendon Press, Oxford)

Potter, R. F. (1957), J. Phys. Chem. Solids, 3, 223

Parthé, E. (1964), Crystal Chemistry of Tetrahedral Structures, (Gordon and Beach, New York)

Pace, N. G. (1971), Private Communication

Palatrick, L. S., Komnik, Yu. F. and Koshkin, V. M. (1963), Sov. Phys. Cryst. 1, 454

Pamplin, B. R. (1960), Nature, 188, 136

Pauling, L. and Huggins, M. L. (1934), Z. Kristall, 88, 205

Pauling, L., Nature of the Chemical Bond, (Cornell University Press), 3rd. Ed., 246

Peierls, R. E. (1940), Proc. Phys. Soc., 52, 34

Pace, N. G. and Saunders, G. A. (1971), Proc. R. Soc., A326, 521

Pomerantz, M. (1965), Proc. I.E.E.E., 53, 1438

Quimby, S. L. and Sutton, P. M. (1953), Phy. Rev., 91, 1122

Ray, B., Spencer, P. M. and Younger, P. A. (1969), J. Phys. D, 3, 37

Szigeti, B. (1950), Proc. R. Soc., A204, 51

Spitzer, W. G. and Fan, H. Y. (1955) Phys. Rev., 99, 1893

Stephens, A. E., Mackey, H. J. and Sybert, J. R., (1970), J of Appl. Phys., 42, 7, 2592

Spencer, P. M. (1964), Brit. J. Appl. Phys., 15, 625

Spencer, P. M., Pamplin B. R. and Wright, D. A. (1962), Proc. Int. Conf. on Phys. of Semiconductors, Exeter, (Inst. of Phys. and Phys. Soc.), 244

Spencer, P. M., and Ray, B. (1968), Brit. J. Appl. Phys. (J. Phys. D.), 1, 229

Seeger, A. (1956), Phil. Mag. 1, 651

Seeger, A., Donth, H. and Pfaff, F. (1957), Discuss. Faraday Soc., 23, 19

Truell, R. Elbaum, C. and Chick, B. B. (1969), Ultrasonic Methods in Solid State Physics, (Academic Press, New York)

Truell, R. and Oates, W. (1963), J. Acoustic Soc. Am., 35, 1382

Testardi, L. R., Bateman, T. B., Reed, W. A. and Chirba, V. G. (1965), Phy. Rev. Letters, 15, 250

Wright, D. A. (1965), Brit. J. Appl. Phys., 16, 939

Wright, D. A. and Dahake, S. L. (1968), Brit. J. Appl. Phys. (J. Phys. D), 2, 1, 831

Waterman, P. C. (1959), Phy. Rev. 113 , 1240

Warekois, E. P., Lavine, M. C. , Mariano, A. N. and Gatos, H. C. (1962), J. Appl. Phys. Rev., 113, 1240

Woolley, J. C. and Ray, B. (1960), J. Phys. Chem. Solids, 15, 27

PUBLICATIONS

1. Effect of Ordered Vacancies on Ultrasonic Wave Propagation in some Mercury Indium Tellurides

   G. A. Saunders and T. Seddon

   Journal of Physics and Chemistry of Solids (1970), 31, 2495

2. An Order-Disorder Transformation in $Hg_3In_2\square Te_6$

   C. A. Maynell, G. A. Saunders and T. Seddon

   Physics Letters (1970), 31A, 6, 338

3. The Effect of Sited Lattice Vacancies on the Elastic Constants of $Hg_5Ga_2\square Te_8$

   G. A. Saunders and T. Seddon

   Physics Letters (1971), 34A, 7, 443

4. In Preparation. The Elastic Constants of $Hg_3Ga_2\square Te_6$

   G. A. Saunders and T. Seddon